Search for Supersymmetry in p-p Collisions at $\sqrt{s} = 13$ TeV Using the α_T Variable with the CMS Detector

by

Kin Ho Lo

Submitted in Partial Fulfillment of the

Requirements for the Degree

Doctor of Philosophy

Supervised by Professor Aran Garcia-Bellido

Department of Physics and Astronomy

Arts, Sciences and Engineering

School of Arts and Sciences

University of Rochester

Rochester, New York

2018

Table of Contents

Biographical Sketch

The author was born in Hong Kong. He attended the Chinese University of Hong Kong, and graduated with a Bachelor of Science degree in Physics in 2012. He began doctoral studies in Physics at the University of Rochester in the same year. He received a Master of Science degree from the University of Rochester in 2014. He pursued his research in high energy physics under the direction of Professor Aran Garcia-Bellido. The following publications were a result of work conducted during doctoral study:

- Search for top squark pair production in compressed-mass-spectrum scenarios in pp collisions at 8 TeV using the α_T variable, CMS-SUS-14-004, Phys. Lett. B 767 (2017) 403, arXiv:1605.08993
- A search for new phenomena in pp collisions at 13 TeV in final states with missing transverse momentum and at least one jet using the α_T variable, CMS-SUS-15-005, Eur. Phys. J. C 77 (2017) 294, arXiv:1611.00338
- Search for natural and split supersymmetric scenarios in proton-proton collisions at 13 TeV in all-jet final states, CMS-SUS-16-038, submitted to JHEP, arXiv:1802.02110

- Constraining top Yukawa coupling from tt differential cross section in lepton+jets final state at 13TeV, in preparation

Acknowledgements

I would like to thank Professor Wayne Knox to serve as the chairperson of my defense. Many thanks to all the people I have worked with over the course of the last five years. In particular, thanks to Rob Bainbridge for his constant help and support and to my α_T colleagues Mark Baber, Shane Breeze, Oliver Buchmueller, Stefano Casasso, Adam Elwood, Henning Flaecher, Christian Laner, Bjoern Penning and Alex Tapper. Thanks also to my HCAL colleagues Edmund Berry, Rohan Bhandari, Andrew Buccili, Pawel de Babaro, Mario Galanti, Ryan Heller, Josh Kunkle, Ted Kolberg, Paolo Rumerio, Jaehyoek Yoo and to my supervisor Aran Garcia-Bellido for his guidance throughout my PhD. I am grateful to my fellow PhD students, Yi-Ting Duh, Adam Elwood, Matthew Citron and Federico Redi for many fruitful discussions. Finally, thanks to my parents for all their patience and support.

Abstract

The thesis describes a search for new physics in form of supersymmetry in hadronic final states and missing transverse energy ($\not{E}_T$) using a dataset of 35.9 fb^{-1} collected during the 2016 proton-proton runs by the Compact Muon Solenoid (CMS) detector at the Large Hadron Collider (LHC). The search uses robust kinematic variables to suppress backgrounds while maintaining good acceptance to a broad range of signal models and employs data-driven techniques to accurately determine backgrounds and systematic uncertainties. No evidence for Beyond Standard Model (BSM) physics is observed and simplified models are used to interpret the results. For gluino mediated models, the gluino mass up to 1850 GeV and the lightest symmetric particle (LSP) up to 1100 GeV are excluded. For light squark mediated models, the light squark mass up to 1350 GeV (700 GeV) and the LSP up to 650 GeV (400 GeV), assuming no degeneracy in the light squark masses (a degeneracy in light squark masses). For sbottom mediated models, the sbottom mass is excluded to 1075 GeV and the LSP mass up to 550 GeV. For stop mediated models, the stop mass is excluded up to 1075 GeV with the LSP mass up to 400 GeV.

Contributors and Funding Sources

This work was supervised by a dissertation committee consisting of Professor Segev BenZvi (Department of Physics and Astronomy), Professor Aran Garcia- Bellido (Department of Physics and Astronomy), Professor Todd Krauss (Department of Chemistry), and Professor Lynne Orr (Department of Physics and Astronomy). All materials in the dissertation were produced by the author unless otherwise stated. The research was supported by the University of Rochester and through two grants from the U.S. Department of Energy: DE-SC0006535 and DE-SC0008475.

List of Tables

List of Figures

Chapter 1.

Introduction

The Standard Model of particle physics, developed throughout the latter half of the 20th century, is a theory describing three of the four known fundamental forces in nature. It describes almost all known phenomena in particle physics (subatomic scale). It provides accurate predictions for a wide range of experimental signatures, for example, the observation of top quark in 1995 [1,2], tau neutrinos in 2001 [3] and Higgs boson in 2012 [4,5].

Despite the huge successes of the SM, it does not provide explanations for some experimental anomalies. One of them is the existence of dark matter (DM) from astronomical observations [6–8] and the neutrino masses [9]. To explain such anomalies, various models for physics beyond SM (BSM) have been proposed. One of the popular candidates is to extend the SM and introduce an additional broken symmetry between fermions and bosons, supersymmetry (SUSY) [10]. SUSY models have rich phenomenological implications and can provide a DM candidate. In addition, SUSY can explain the existence of a low mass Higgs boson and unify the strong, weak and electromagnetic forces at the energy scale of 10^{18} GeV (the Grand Unified Theory scale). The features of the SM and SUSY models are introduced in Chapter 2.

To explore physics at high energy scales in the laboratory, particles are accelerated to high energies by particle accelerators and collided head on. The Large Hadron Collider (LHC) was built at CERN near Geneva, Switzerland in 2008 [11]. The LHC collides protons at record-breaking energies. Two general-purpose detectors, the Compact Muon Solenoid (CMS) and A Toroidal LHC Apparatus (ATLAS), were also built separately at collision points of the LHC to detect and collect results of these collisions. One of the main focus of these two experimental programs is to search for possible BSM physics signatures at highest ever achieved energies. The LHC and CMS detector are described in Chapter 3. The reconstruction of data collected by the CMS detector is introduced in Chapter 4.

This thesis presents results from a search for SUSY in hadronic final states, known as the α_T analysis, with proton-proton collision data collected by the CMS detector at the LHC, at center of mass energy $\sqrt{s} = 13$ TeV in 2016. The analysis strategies are introduced in Chapter 5. Methods for background estimation in the α_T analysis are detailed in Chapter 8, while the statistical analysis and interpretations of results are explained in Chapter 9.

Chapter 2.

Theory Overview

2.1. The Standard Model

The SM describes all known elementary particles and three of the four known fundamental interactions (electromagnetic, weak and strong). All matter particles are represented as spin-$\frac{1}{2}$ fermionic fields, and the three interactions in the SM are represented and mediated by spin-1 bosonic fields. An additional spin-0 scalar field, called the Higgs field, is introduced to provide masses for various elementary particles and force carriers. The SM incorporates the Lorentz and gauge invariance within the framework of renormalizable quantum field theories. One of the easiest ways to include Lorentz invariance and other symmetries is by using the common Lagrangian formalism [12]. The SM Lagrangian can be written as [13]

$$L_{\text{SM}} = L_{\text{gauge}} + L_{\text{fermion}} + L_{\text{Higgs}} + L_{\text{Yukawa}} \tag{2.1}$$

where L_{gauge}, L_{fermion}, L_{Higgs} and L_{Yukawa} encode free field and interaction terms of gauge bosons, fermions, Higgs boson and Yukawa couplings of the Higgs field and fermion fields respectively.

2.1.1. Particle classification

All known elementary particles in the SM can be classified into spin-$\frac{1}{2}$ fermions (quarks and leptons), spin-1 gauge bosons which acts as force carriers for the three

Fermion type	Generation			T	T_3	Y	Q	Color charge
	1st	2nd	3rd					
Leptons	$\begin{pmatrix}\nu_e \\ e\end{pmatrix}_L$	$\begin{pmatrix}\nu_\mu \\ \mu\end{pmatrix}_L$	$\begin{pmatrix}\nu_\tau \\ \tau\end{pmatrix}_L$	$\frac{1}{2}$	$\begin{pmatrix}\frac{1}{2} \\ -\frac{1}{2}\end{pmatrix}$	-1	$\begin{pmatrix}0 \\ -1\end{pmatrix}$	0
	e_R	μ_R	τ_R	0	0	-2	-1	0
Quarks	$\begin{pmatrix}u \\ d\end{pmatrix}_L$	$\begin{pmatrix}c \\ s\end{pmatrix}_L$	$\begin{pmatrix}t \\ b\end{pmatrix}_L$	$\frac{1}{2}$	$\begin{pmatrix}\frac{1}{2} \\ -\frac{1}{2}\end{pmatrix}$	$\frac{1}{3}$	$\begin{pmatrix}\frac{2}{3} \\ -\frac{1}{3}\end{pmatrix}$	r, g, b
	u_R	c_R	t_R	0	0	$\frac{4}{3}$	$\frac{2}{3}$	r, g, b
	d_R	s_R	b_R	0	0	$-\frac{2}{3}$	$-\frac{1}{3}$	r, g, b

Table 2.1.: Summary of the three generations of fermions and their properties. T, T_3 and Y represent total weak isospin, the third component of weak isospin and hypercharge respectively. $Q = T_3 + \frac{1}{2}Y$ represents electric charge [9].

Boson type	T	T_3	Y	Q	Color charge	Force
photons	0	0	0	0	0	Electromagnetic
Z	0	0	0	0	0	Weak
W	1	± 1	0	± 1	0	Weak
gluons	0	0	0	0	$r\bar{g}, r\bar{b}, g\bar{r}, g\bar{b}, b\bar{r}, b\bar{g}, \frac{1}{\sqrt{2}}(r\bar{r} - g\bar{g}), \frac{1}{\sqrt{6}}(r\bar{r} + g\bar{g} - 2b\bar{b})$	Strong
H	$\frac{1}{2}$	$-\frac{1}{2}$	$+1$	0	0	-

Table 2.2.: Summary of gauge boson and their properties [9].

fundamental interactions and one spin-0 Higgs boson for generating masses for all other elementary particles. Table 2.1 and 2.2 shows properties of the three generations of fermions and bosons respectively.

2.1.2. Gauge theory

Gauge invariance is a central feature of modern renormalizable field theories. For a spin-$\frac{1}{2}$ field with local $U(1)$ invariance, the fermion Lagrangian can be written as [14]

$$L_{\text{fermion}} = i\bar{\varphi}\gamma^{\mu}(\partial_{\mu} + iqA_{\mu})\varphi - m\bar{\varphi}\varphi \tag{2.2}$$

$$L_{\text{gauge}} = -\frac{1}{4}F^{\mu\nu}F_{\mu\nu} \tag{2.3}$$

where φ is the Dirac field, A_{μ} is the gauge field, m is the mass of the fermion and γ^{μ} is the gamma matrix. The field strength $F_{\mu\nu}$ is defined as $F_{\mu\nu} = \partial_{\mu}A_{\nu} - \partial_{\nu}A_{\mu}$. Under the local $U(1)$ gauge transformation,

$$\varphi \to e^{iq\alpha(x)}\varphi \tag{2.4}$$

$$A_{\mu} \to A_{\mu} + \partial_{\mu}\alpha \tag{2.5}$$

the fermion Lagrangian L_{fermion} is invariant. The term $iqA_{\mu}\varphi\gamma^{\mu}\varphi$ encodes the interaction of the gauge field with the fermion. Such term is dedicated and required by gauge invariance.

Gauge transformation can also involve internal degrees of freedom by promoting the $U(1)$ abelian gauge group to non-abelian gauge group such as $SU(2)$ and $SU(3)$ [13]. Gauge transformation in Equation 2.4 becomes instead

$$\varphi \to e^{ig\alpha^{a}(x)T^{a}}\varphi \tag{2.6}$$

$$A^{a}_{\mu} \to A^{a}_{\mu} + \partial_{\mu}\alpha^{a} + g\alpha^{a}(x)A^{a}_{\mu} \tag{2.7}$$

where g, T^{a} are the coupling constant and generator matrix in the adjoint representation of the corresponding gauge group [13]. The corresponding Lagrangian can be rewritten as [13]

$$L_{\text{fermion}} + L_{\text{gauge}} = i\bar{\varphi}\gamma^{\mu}(\partial_{\mu} + igT^{a}A^{a}_{\mu})\varphi - m\bar{\varphi}\varphi - \frac{1}{4}F^{a,\mu\nu}F^{a}_{\mu\nu} \tag{2.8}$$

where $F^{a}_{\mu\nu} = \partial_{\mu}A^{a}_{\nu} - \partial_{\nu}A^{a}_{\mu} - gf_{abc}A^{b}_{\mu}A^{c}_{\nu}$. The Lagrangian is again invariant under gauge transformation 2.6. The extra term $gf_{abc}A^{b}_{\mu}A^{c}_{\nu}$ arises from the non-abelian nature of the gauge group and is absent in the $U(1)$ gauge theory. It gives rise to self interactions of gauge bosons.

2.1.3. Strong interaction

The strong interaction can be formulated as a $SU(3)$ gauge theory, known as quantum chromodynamics, with eight massless gauge fields as gluons, and fermions as quark fields. Both quark and gluon fields have non-trivial representations under $SU(3)$ transformation and possess color charges. Unlike electromagnetism, color charge screening from virtual gluons in vacuum gives rise to the interesting property called asymptotic freedom [15], which means that the strong coupling constant decreases for shorter length scales (or equivalently higher energy scales) of physics processes considered. This means that perturbative QCD is asymptotically converging at high energy scales but not valid anymore as the energy scale decreases [16].

2.1.4. Electroweak interaction

The electromagnetic and weak interaction are described by a single $SU(2) \times U(1)$ gauge theory in the SM. The unification of the two interactions in one single theory is one of the major breakthroughs in particle physics in the 19th century [17–19]. One problem with the formulation of gauge theory is that gauge bosons have to be massless. To provide masses for the electroweak gauge bosons, the gauge theory also undergoes spontaneous symmetry breaking with the Higgs mechanism [20–22] described in Section 2.1.5.

The weak isospin $SU(2)$ gauge group of the electroweak theory has three generators $T_i = \tau_i/2$, where τ_i are the Pauli spin matrices and $i = 1, 2, 3$, and hence three gauge fields W^i_μ are required by the theory. These gauge fields only couple to the left handed chiral component of the fermion field and this explicitly violates parity. Parity violation was observed in 1956 by the Wu experiment [23].

Similar to the $U(1)$ gauge theory described in Section 2.1.2, the hypercharge $U(1)$ gauge group is an abelian gauge group with one generator and one gauge field B_μ.

W_μ^i and B_μ mix to give physical gauge boson fields. One of the most common representations of the boson fields is [13]

$$W_\mu^\pm = \frac{1}{2}\left(W_\mu^1 \mp iW_\mu^2\right) \tag{2.9}$$

$$Z_\mu = \cos\theta_W W_\mu^3 - \sin\theta_W B_\mu \tag{2.10}$$

$$A_\mu = \sin\theta_W W_\mu^3 + \cos\theta_W B_\mu \tag{2.11}$$

where A_μ, Z_μ and $W_\mu^\pm$ are the photon, Z boson and W boson fields respectively. The Weinberg angle θ_W can be expressed in terms of the coupling strengths of $U(1)$ ($g^{'}$) and $SU(2)$ gauge field (g).

After mixing , the left-handness of the theory is manifested by $W_\mu^\pm$ coupling only to the left handed fermion fields.

2.1.5. The Higgs Mechanism

The formulation of strong and electroweak interactions as gauge theories requires the gauge bosons (W boson, Z boson, photon and gluon) to be massless. It is not compatible with the experimental observation of massive W and Z bosons [24–27]. To provide masses for these two electroweak gauge bosons, the Higgs mechanism [20–22] was proposed as a special case of spontaneous symmetry breaking.

A symmetry is spontaneously broken if the ground state of a physical system does not conserve the symmetry, even though the Lagrangian preserves the symmetry. A set of degenerate ground states is available and connected through the spinless Goldstone boson [28], corresponding to the internal generators of the broken symmetry.

In the case of the Higgs mechanism, a complex $SU(2)$ scalar field ϕ is introduced as

$$\phi = \begin{pmatrix} \phi^+ \\ \phi^0 \end{pmatrix} \tag{2.12}$$

with the corresponding Lagrangian as:

$$L_{\text{Higgs}} = (D_\mu \phi)^\dagger (D^\mu \phi) - V(\phi) \tag{2.13}$$

where $D_\mu = \partial_\mu + igT^a W^a_\mu + ig' B_\mu$. It is worth noting that the quantum numbers of the ϕ^+ and ϕ^0 field are slightly different, as summarized in Table 2.3. The potential $V(\phi)$ is proposed to be:

$$V(\phi) = \mu^2 \phi^\dagger \phi + \lambda(\phi^\dagger \phi)^2 \tag{2.14}$$

where $\mu^2 < 0, \lambda > 0$. In a classical theory, the potential leads to a ground state solution with $|\phi|^2 = -\frac{\mu^2}{2\lambda}$. The quantum analog is a continuous set of vacuum states with a non-vanishing expectation value in the vacuum state $\langle 0||\phi|^2|0\rangle = -\frac{\mu^2}{2\lambda}$. The physical vacuum selects a preferred direction in the weak isopin and hypercharge space and spontaneously breaks the $SU(2) \times U(1)$ gauge invariance. In the unitary gauge which contains only physical degrees of freedom [29], the vacuum state can be conveniently chosen such that the vacuum expectation value is

$$\langle 0|\phi|0\rangle = \begin{pmatrix} 0 \\ \sqrt{\frac{\mu^2}{2\lambda}} \end{pmatrix} \tag{2.15}$$

and the Higgs field can be rewritten as

$$\phi = \begin{pmatrix} 0 \\ v + H \end{pmatrix} \tag{2.16}$$

where v is the vacuum expectation value and the quantum field H has zero vacuum expectation value. The Lagrangian of the Higgs field can then be rewritten as

$$L_{\text{Higgs}} = \frac{1}{2}(\partial^\mu H)(\partial_\mu H) - \frac{1}{4}g^2 W^+ W^- (v+H)^2 + \frac{1}{8}g_Z^2 ZZ(v+H)^2 - V\left[\frac{1}{2}(v+H)^2\right] \tag{2.17}$$

and the v^2 terms provide the mass terms for W and Z boson. In this case, the Goldstone bosons, which have three degrees of freedom from the symmetry breaking, are 'eaten' by the W and Z boson as the massive components of the fields. The

Field	T	T_3	Y	Q
ϕ^+	$\frac{1}{2}$	$+\frac{1}{2}$	1	1
ϕ^0	$\frac{1}{2}$	$-\frac{1}{2}$	1	0

Table 2.3.: Summary of quantum numbers of the Higgs field [9].

photon field remains massless as there is no fourth degree of freedom from the Goldstone boson.

The essence of the Higgs mechanism is to introduce mass terms for W and Z bosons in a gauge invariant manner. The mechanism introduces a scalar field and predict the existence of the Higgs boson with a mass of $\sqrt{2\mu^2}$. The Higgs boson has been discovered by the ATLAS and CMS collaboration with a mass of 125 GeV [4,5].

The same mechanism can also generate mass terms for leptons and quarks, if additional Yukawa interactions are included in the theory. In the case of electrons,

$$L_{\text{Yukawa}} = -G_e \left[\bar{e_R}(\phi^\dagger \ell_L) + (\bar{\ell_L}\phi)e_R \right] \tag{2.18}$$

where $\ell_L = \begin{pmatrix} \nu_e \\ e \end{pmatrix}_L$. By substituting Equation 2.16,

$$L_{\text{Yukawa}} = \frac{G_e v}{\sqrt{2}}\bar{e}e - \frac{G_e}{\sqrt{2}}H\bar{e}e \tag{2.19}$$

Not only does the electron field acquire a mass of $m_e = \frac{G_e v}{\sqrt{2}}$, but also a Yukawa coupling with the Higgs field with a coupling strength proportional to its mass. The same procedure can be applied to the μ and τ lepton. In the case of quarks, a similar procedure can be applied, with a slight complication of both up-type and down-type quarks having masses. The conjugate multiplet of the Higgs doublet $\tilde{\phi}$, with $Y = -1$, has to be included to generate masses for down-type quarks

$$\tilde{\phi} = i\tau_2\phi^* \tag{2.20}$$

where τ_2 is the y-th component of the Pauli matrices. The Lagrangian can be written as

$$L_{\text{Yukawa}} = -\sum_{i=1}^{3}\sum_{j=1}^{3}\left[\tilde{G}_{ij}\bar{u_{iR}}(\tilde{\phi}^{\dagger}D_{jL} + G_{ij}\bar{d_{iR}}(\phi^{\dagger}D_{jL})\right] + \text{h.c.} \tag{2.21}$$

where $D_{jL} = \begin{pmatrix} u_j \\ d_j \end{pmatrix}_L$. By again substituting Equation 2.16, one can obtain the mass terms

$$\sum_{i,j=1}^{3} u_{iR}M^{u}_{ij}u_{jL} + \text{h.c.} \tag{2.22}$$

$$\sum_{i,j=1}^{3} d_{iR}M^{d}_{ij}d_{jL} + \text{h.c.} \tag{2.23}$$

where $M^{u}_{ij} = \frac{v}{\sqrt{2}}\tilde{G}_{ij}$ and $M^{d}_{ij} = \frac{v}{\sqrt{2}}G_{ij}$. The matrices M^{u} and M^{d} can be transformed to diagonal forms by a unitary transformation and forms the mass eigenstate of the quark fields. The coupling strengths of the quark-Higgs Yukawa interaction are characterized by the Cabibbo-Kobayashi-Maskawa (CKM) matrix following the unitary transformation. Detail of the generation mixing of quarks is described in [9, 13].

2.2. Physics beyond the Standard Model

Despite being incredibly successful in predicting physics phenomena up to the electroweak energy scale (~ 100 GeV), there are several unsolved anomalies that cannot be explained by the SM alone. Such anomalies indicate the likely existence of Beyond the Standard Model (BSM) physics at higher energy scales.

One of the main issues with the SM concerns the naturalness of the Higgs mass parameter, known as the Higgs mass hierarchy problem. In particular, within the SM, the physical mass of the Higgs boson can be expressed as [10]

$$m_{\text{physical}} = m_{\text{bare}} + \Delta m_{\text{H}} \tag{2.24}$$

where Δm_{H} corresponds to the quantum loop correction to the Higgs mass, which is approximately expressed as

$$\Delta m_{\mathrm{H}}^2 \sim -\frac{\Lambda^2}{8\pi^2}\lambda_f^2 \tag{2.25}$$

where Λ is the cut-off energy of the theory and λ_f is the coupling strength of the Higgs field to fermions. The cut-off value must occur at the Planck scale $\Lambda_{\mathrm{Planck}} \sim 10^{19}$ GeV where effects of gravity become important. The huge difference between the Planck scale and the Higgs mass of 125 GeV indicates that fine-tuned cancellations are required in Equation 2.24 to keep the Higgs mass low. This seemingly high degree of fine-tuning, although not physically forbidden, is unnatural and points to BSM physics.

Furthermore, astronomical and cosmological observations, such as the measurement of the rotation speed of galaxies, gravitational lensing and measurement of the Cosmic Microwave Background (CMB), suggest the vast majority of matter in the universe is not baryonic and would indicate the existence of weakly interacting dark matter (DM). The SM, however, does not have a suitable particle candidate for DM.

Last but not least, the SM, while successfully unifies the electromagnetic and weak interaction, fails to unify the strong interaction at high energy. Analysis of running coupling constants shows that the coupling constants of the SM do not converge to one single coupling strength [30] in the absence of BSM physics at the Grand Unified Theory (GUT) scale.

2.3. Supersymmetry

Supersymmetry (SUSY) is an extension of the space-time symmetries in the Poincaré group [31]. It is a symmetry that relates fermions to bosons and vice versa. The theory predicts the existence of a superpartner for every SM particle with the same quantum numbers, except differing in spin by $\frac{1}{2}$. If SUSY was an exact symmetry in nature, then each SM particle and the corresponding superparter would be degenerate in mass and would have been already observed. As a consequence, SUSY has to be a broken symmetry: The mass of the superpartners has to be much larger than the SM particles. SUSY breaking can be introduced in many ways and one of the most popular is the Minimal Supersymmetric Standard Model described in Section 2.3.1.

SUSY can provide solutions to various issues in the SM described in Section 2.2. The existence of the superpartners can stabilize loop corrections from higher energy scale in equation 2.24 by including an extra contribution to the loop correction [10]

$$\Delta m_{\mathrm{H}}^2 \sim -\frac{\Lambda^2}{8\pi^2}\left(\lambda_s - \lambda_f^2\right) \tag{2.26}$$

where λ_s is the coupling strength of the Higgs field to the scalar superpartner to the fermion field. In addition, various extension of the SM by supersymmetry can provide one ore more hypothetical particle as the weakly interacting DM candidates. SUSY can stabilize the converging of various coupling constants measured in the electroweak energy scale in the SM, when extrapolating to a higher energy scale [30]. SUSY is therefore a viable theory for the Grand Unification of strong and electroweak interaction.

2.3.1. The Minimal Supersymmetric Standard Model

The MSSM is an extension of the SM with supersymmetry with a minimal set of additional particles and interactions. Table 2.4 shows a summary of new particles introduced in the MSSM and their corresponding quantum numbers. Superpartners are distinguished from their SM counterparts with a tilde in notation. An additional scalar Higgs doublet is added on top of the SM Higgs doublet described in Section 2.1.5 to introduce separate Yukawa couplings for up-type and down-type quarks, and avoid gauge anomalies from loop corrections in the theory [10]. Superpartners of electroweak gauge boson and Higgs bosons undergo mixing and give rise to four neutral neutralinos, two charginos.

Lepton and baryon number violation can occur in the MSSM, and leads to proton decay. Given the strong experimental constraint on the proton lifetime [32], one of the most popular solutions is to introduce a symmetry with a multiplicative

Particle	Notation	Spin	Charge Q
Up-type squarks	$\tilde{u}, \tilde{c}, \tilde{t}$	0	$+\frac{2}{3}$
Down-type squarks	$\tilde{d}, \tilde{s}, \tilde{b}$	0	$-\frac{1}{3}$
Sleptons	$\tilde{e}, \tilde{\mu}, \tilde{\tau}$	0	-1
Sneutrinos	$\tilde{\nu_e}, \tilde{\nu_\mu}, \tilde{\nu_\tau}$	0	0
Gluino	$\tilde{g}$	$\frac{1}{2}$	0
Neutralinos	$\tilde{\chi}_1, \tilde{\chi}_2, \tilde{\chi}_3, \tilde{\chi}_4$	$\frac{1}{2}$	0
Charginos	$\tilde{\chi}_1^\pm, \tilde{\chi}_2^\pm$	$\frac{1}{2}$	± 1
Neutral Higgs boson	h, H, A	0	0
Charged Higgs boson	$H^\pm$	0	± 1

Table 2.4.: Summary of sparticles and their quantum numbers in MSSM [34].

quantum number known as the R-parity

$$R = (-1)^{3B-3L+2s} \tag{2.27}$$

where B is the baryon number, L is the lepton number and s is the spin of the particle. Under this definition, SM particles have $R = +1$ and sparticles have $R = -1$. As a result, proton-proton collisions, an initial state with $R = +1$, lead to sparticles always being produced in pairs. Furthermore, decays of sparticles have to contain at least one sparticle in final states, meaning the lightest supersymmetric particles (LSP) is stable. Various sparticles could be the LSP, depending on the mass spectrum and parameters of the SUSY model considered. The LSP is prominently postulated to be the neutral and weakly interacting lightest neutralino, and serves as a possible DM candidate [33].

2.3.2. SUSY at the LHC

The LHC, as a multi-purpose particle accelerator detailed in Section 3.1, predominantly performs proton-proton collisions for the purpose of searches of new physics and precise measurements in SM physics. At the highest ever achieved energy with particle accelerators, data of proton-proton collisions in the LHC provide an unprecedented opportunity to discover or exclude SUSY. Assuming R-parity, typical SUSY signatures in the LHC involve pair production of sparticles which quickly decay to various SM particles and weakly interacting neutral LSPs which escape the detector undetected. This introduces significant imbalance in transverse momenta in the collisions.

The LHC, as a hadron collider, would predominantly produce sparticles in strong production, i.e. squarks and gluons. As shown in Figure 2.1, the cross sections of various strong SUSY particles are often an order of magnitude or more higher than the electroweak counterparts. Each squark or gluon produced would predominantly decay to quarks, gluons and a LSP. Therefore, the signature could be characterized by a number of jets hadronized from quarks and gluons and missing transverse momenta.

Signatures of SUSY have been extensively searched for in previous collider experiments, such as LEP [35] and Tevatron [36], and also with ATLAS and CMS data from the LHC Run 1 period. No evidence of SUSY has been found yet. Figure 2.2 shows a summary of exclusion limits on various sparticle masses with the data collected by CMS in Run 1 at 8 TeV. These exclusions significantly exceeded results from previous collider experiments.

2.3.3. Simplified models

Typical SUSY models such as the MSSM introduce a large number of new parameters, complicated kinematics and SUSY mass spectra could arise from the large number of degrees of freedom. To facilitate interpretations of experimental results from ATLAS and CMS, simplified models [38,39] are introduced. These models only consider a specific SUSY production and decay process. Other sparticles not directly relevant to this channel are set to have much higher masses and decouple from the model. Figure 2.3 shows two examples of simplified models with pair production of gluinos and squarks. Each simplified model can be specified completely by masses of sparticles considered in the corresponding model. Experimental results are typically interpreted as limits in a wide range of sparticle masses in the case of no observed SUSY signatures.

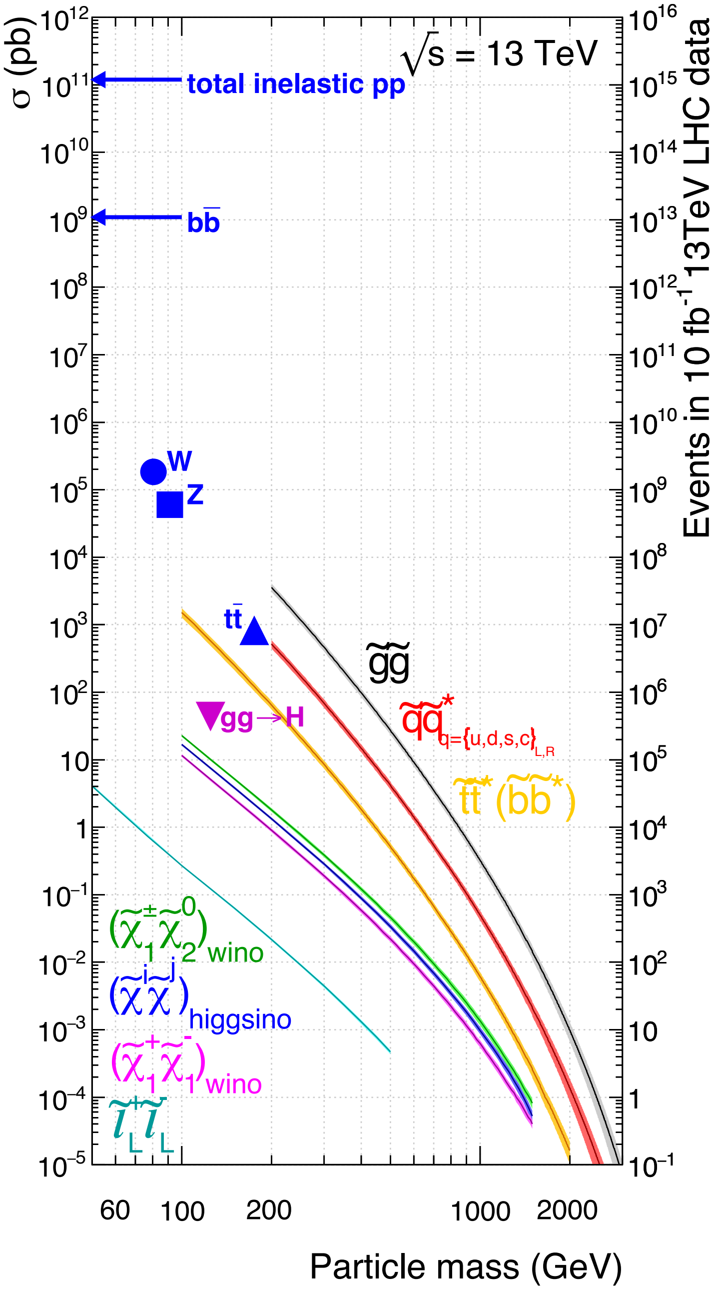

Figure 2.1.: Cross section of various SM and SUSY processes with center of mass energy of 13 TeV. From [36].

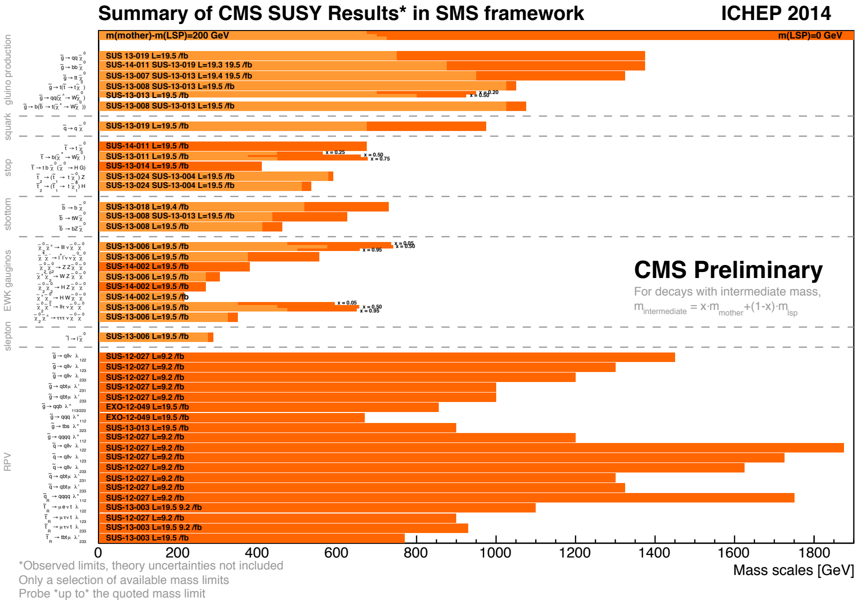

Figure 2.2.: Summary of exclusion limits against the sparticle mass for various SUSY models from CMS with data collected during Run 1 in 8 TeV. From [37].

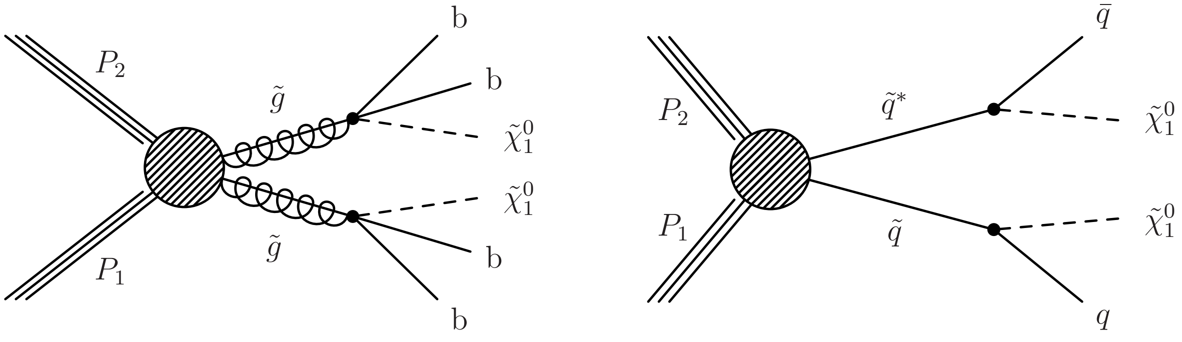

(a) T1bbbb **(b)** T2qq

Figure 2.3.: Simplified model with pair production of gluinos decaying to four b-quarks (2.3a) and two LSPs, squarks decaying to two light quarks and two LSPs (2.3b).

Chapter 3.

The LHC and CMS experiment

3.1. The LHC

The LHC is the biggest particle accelerator ever built. It is designed to collide protons or heavy lead ions up to a center of mass energy of $\sqrt{s} = 14$ TeV. It is located between France and Switzerland at the European Center for Nuclear Research (CERN). Particles are collected into bunches of 10^{11} protons, which are 25 ns or 50 ns apart, and accelerated in multiple stages. Hydrogen atoms are first stripped into protons and accelerated to 50 MeV by the Linear Accelerator 2 (LINAC2). The resulting proton beams are further accelerated by the Proton Synchrotron Booster (PSB) to 1.4 GeV. The beams are then injected into the Proton Synchrotron (PS) and boosted to 26 GeV. The final acceleration of the beam to 450 GeV is provided by the Super Proton Synchrotron (SPS) before being injected into the LHC. Inside the LHC, the bunches are steered by 1200 superconducting dipole magnets and accelerated further to 6.5 TeVwith radio frequency cavities. Once the beam reaches the desired energy, protons are collided at four different interaction points on the ring. Four different detectors (ALICE, ATLAS, LHCb and CMS) are built at each interaction point respectively and products from collisions are recorded and stored for later analysis. Figure 3.1 shows a representation of this accelerator complex.

Apart from the record-breaking center of mass energy at 13 TeV, the LHC collides hadrons at a very high luminosity, with a collision rate of up to 40 MHz [11].

Proton bunches are also squeezed to increase the luminosity, which also increases the number of simultaneous collision for each bunch crossing. Extra simultaneous collisions are called pile-up (PU). The LHC operates in an environment of $PU \sim 27$ in 2016. The design of the LHC to deliver high luminosity is necessary because the rate of electroweak and other BSM processes is significantly lower than the main backgrounds from inelastic collisions. The instantaneous luminosity of the machine is 10^{34} cm^{-2} s^{-1}.

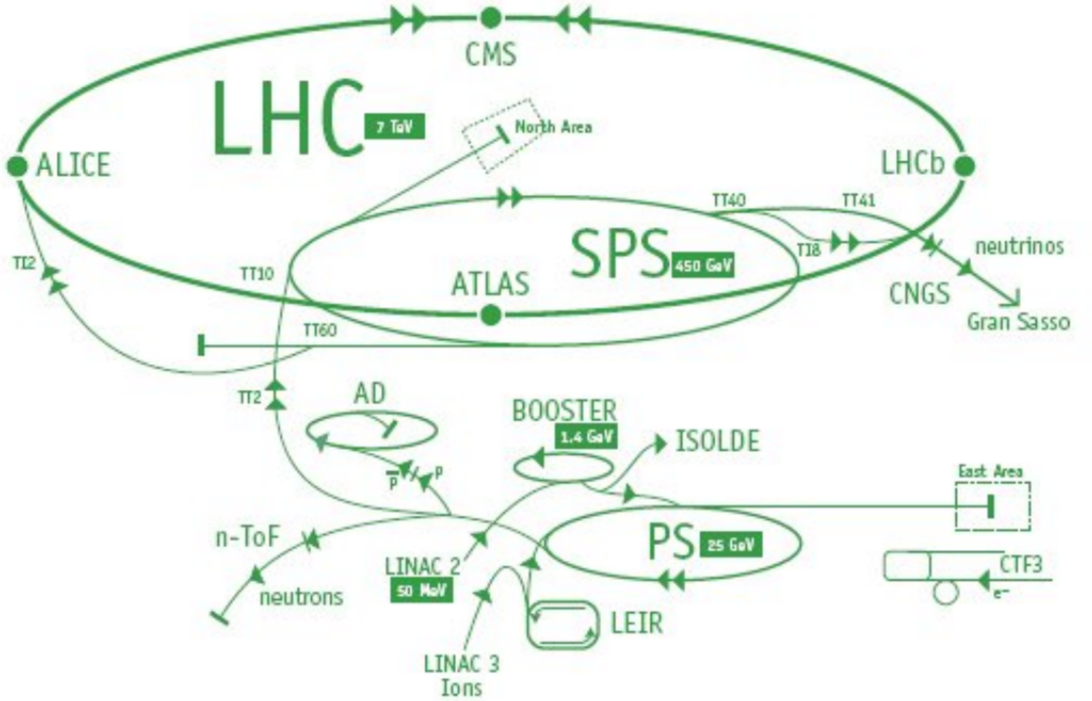

Figure 3.1.: A representation of the CERN accelerator complex for the LHC. From [40].

3.2. The CMS detector

The CMS detector is one of the two general-purpose detectors at the interaction points of the LHC ring. It was designed for the discovery of the Higgs boson and searching for a wide range of BSM physics signatures. The detector consists primarily of four sub-detectors and a 3.8 T superconducting solenoid. Figure 3.2 shows a representation of the CMS detector and its sub-detectors. The detector is constructed in a series of cylindrical-shaped sub-detectors with the center as the collision point. The first layer is the silicon tracking system, which reconstructs trajectories of charged particles arising from each collision. Trajectories of charged particles are bent by the strong magnetic field provided by the superconducting solenoid and their momenta can be measured by the curvatures of tracks. The second layer is the electromagnetic calorimeter (ECAL), one of the two sampling calorimeters in the detector. It absorbs and measures the energy of photons and electrons that produce electromagnetic showers. The third layer is the hadron calorimeter (HCAL), another sampling calorimeter like ECAL specialized in absorbing and measuring energies of hadrons from hadronic showers. These three sub-detectors are enclosed by the superconducting solenoid. Outside this solenoid, the final layer is the muon chambers and iron return yoke. The chambers are designed to detect muons which normally are not absorbed by the inner sub-detectors. Last but not least, data from all sub-detectors are read out and passed to the trigger system, which decides if data from each collision should be recorded and stored for offline processing, because of the limited bandwidth and storage space to store data from every collision.

3.2.1. The tracker

The CMS tracker is designed to accurately determine the trajectories of charged particles. In the presence of the strong magnetic field provided by the CMS solenoid, the curvature of the trajectories of charged particles can be used to reconstruct momenta with high resolution. High spatial resolution of the CMS tracker allows for accurate measurements of primary or secondary decay vertices and provides a good performance even with high levels of PU. The tracker is an all-silicon tracker. Electron-hole pairs are produced when charged particles pass through doped silicon, and electric currents can arise in the the presence of an electric field. The silicon tracker can achieve a high level of spatial precision and fast response time even in a high radiation environment.

The CMS tracker consists of the pixel detector and the strip tracker. The cross section of the tracker in the $r - z$ plane is shown in Figure 3.3. The pixel detector is a high granularity tracking system closest to the interaction point, extending up to $r <$ 20cm, $|\eta| < 2.5$. The pixel detector consists of three cylindrical layers with 66

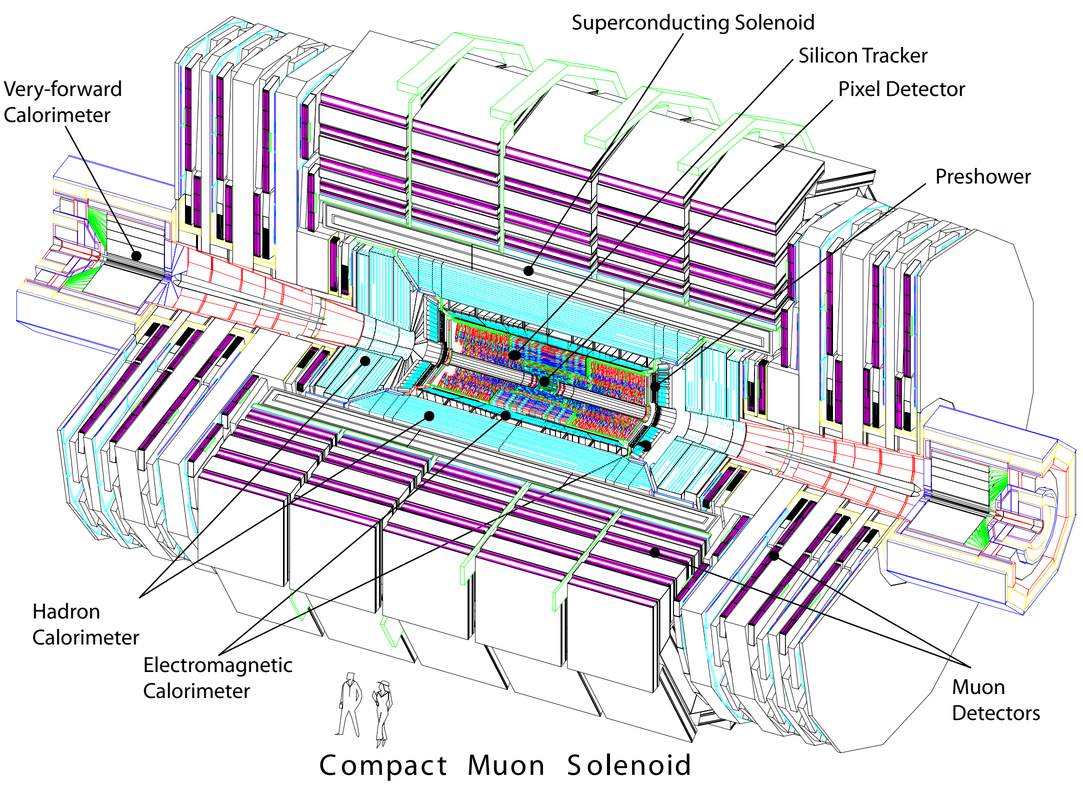

Figure 3.2.: A representation of the CMS detector and its associated sub-detectors. From [41].

million silicon pixels of size 100 μm × 150 μm, and two disks at the forward region on each side. The high spatial resolution of the pixel detector is essential for precise determination of primary and secondary vertices originating from, for example, decays of b-hadrons from b-jets.

In the region $r > 20$ cm resides the strip tracker, which consists of three subsystems with 9.6 million silicon strips covering an area of 198 m^2, namely the Tracker Inner Barrel and disks (TIB/TID), the Tracker Outer Barrel (TOB) and the Tracker End Caps (TEC). Sizes of these silicon strips range from $10 - 25$ cm long and $80 - 180$ μm wide. The strip tracker provides complementary information to reconstruct the trajectory of charged particles with high efficiency at large radii.

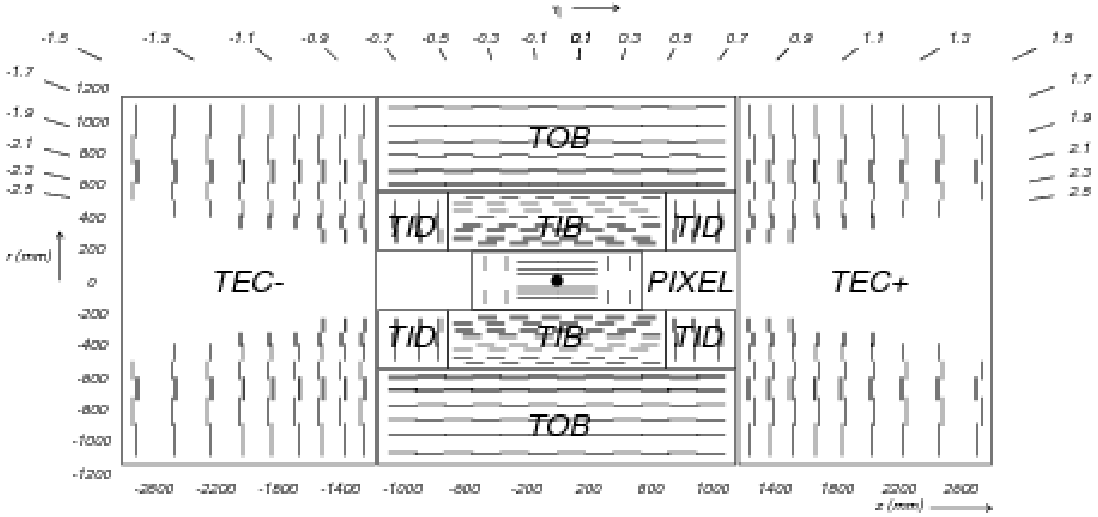

Figure 3.3.: The cross section of the CMS tracker. Detector modules are represented by black lines. From [42].

3.2.2. The electromagnetic calorimeter

The ECAL is one of the two sampling calorimeters in the CMS detector, specializing in the measurement of energies of electrons and photons. It consists of three subdetectors, the ECAL barrel (EB) in the region of $|\eta| < 1.479$, the ECAL endcaps (EE) in the region of $1.479 < |\eta| < 3.0$, and the Preshower just before the EE in the region of $1.653 < |\eta| < 2.6$. The layout of the ECAL can be seen in Figure 3.4.

The entire ECAL is constructed from 75848 lead tungstate ($PbWO_4$) scintillating crystals. High-energy electrons and photons initiate electromagnetic showers. Lower energy particles in the shower will ionize the atoms in the crystals and scintillating light is emitted as the atoms de-excite. Scintillating light then travels through the transparent crystals and is measured by photo-diodes and photo-triodes. Electric currents are created and the magnitude of the currents is proportional to the energy of the scintillating light. A time dependent calibration is carried out to account for the degrading transparency of the crystals because of radiation damage.

The energy resolution of the $PbWO_4$ scintillating crystals was measured in a test beam. The empirical formula of the resolution σ_{ECAL} [43] is given by

$$\left(\frac{\sigma_{\mathrm{ECAL}}}{E}\right)^2 = \left(\frac{2.8\%}{\sqrt{E}}\right)^2 + \left(\frac{12\%}{E}\right)^2 + (0.30\%)^2 \tag{3.1}$$

where E is the energy of the incident particle. The first term arises from fluctuations on the lateral containment, fluctuations on the energy deposited in the preshower absorber and photostatistics. The second term captures the effects from preamplifier, digitization and PU noise. The third term accounts for effects from the non-uniformity of the longitudinal light collection, crystal calibration uncertainty, leakage of energy from the back of the crystal [44].

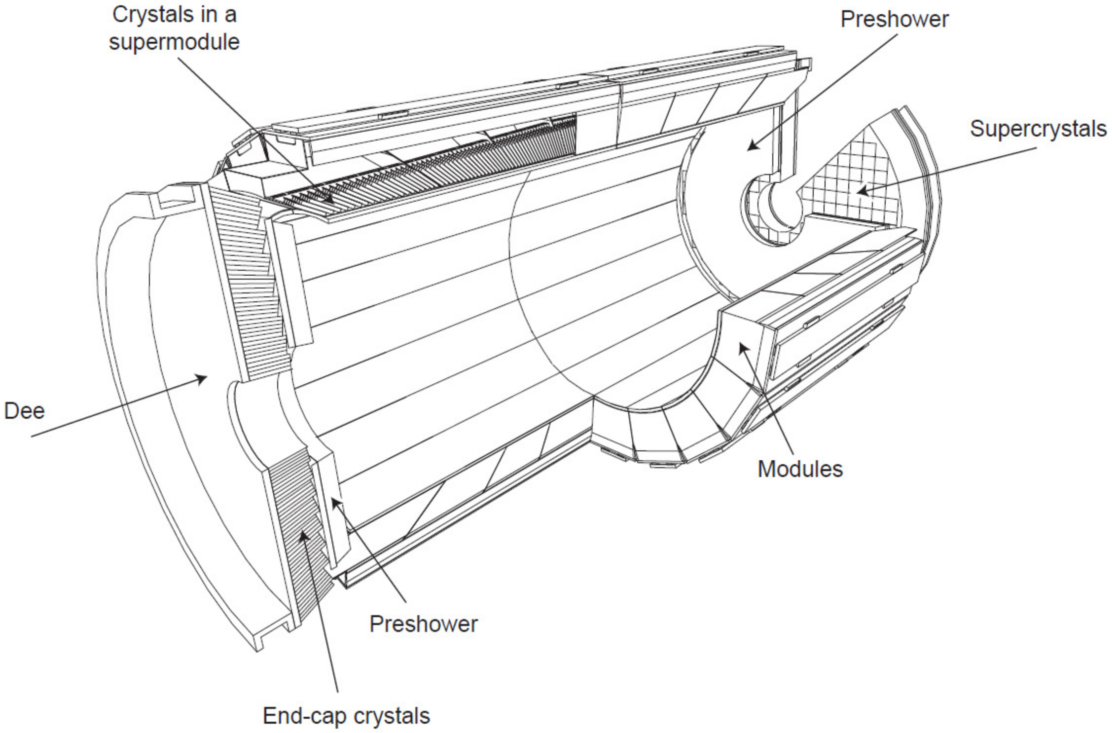

Figure 3.4.: Layout of the CMS electromagnetic calorimeter. From [45].

3.2.3. The hadron calorimeter

The HCAL is another sampling calorimeter designed to measure hadron energies and resides between the ECAL and the solenoid. It consists of four subdetectors, namely the HCAL barrel (HB), the HCAL endcap (HE), the HCAL outer (HO) and the HCAL forward (HF). The layout of the HCAL detector is shown in Figure 3.5. The HB consists of 17 layers of brass absorber interleaved with scintillating plastic tiles in the region $|\eta| < 1.3$, and the HE is composed of 14 layers of the same absorbers with scintillating plastic tiles in the region $1.3 < |\eta| < 3.0$. Brass absorbers provide a good performance for the HCAL inside the solenoid magnet, as they are non-magnetic and have a short interaction length ($\sim$ 16 cm) to ensure a full embedding of hadron showers within the HCAL.

Outside the solenoid magnet, a dedicated subdetector is also designed and installed 11 m from the interaction point to provide accurate measurement of hadron showers for the forward region $3.0 < |\eta| < 5.0$. In addition, just beyond the solenoid magnet is the HO, which absorbs any late-starting or highly-penetrating showers and effectively increases the overall interaction length with the HB.

The HCAL energy resolution was measured in a test beam of single pions and can be parametrized as an empirical formula [46]:

$$\left(\frac{\sigma_{\mathrm{HCAL}}}{E}\right)^2 = \left(\frac{84.7 \pm 1.6\%}{\sqrt{E}}\right)^2 + (7.4 \pm 0.8\%)^2 \tag{3.2}$$

where E is the energy of the incident particle.

3.2.4. Superconducting magnet

The superconducting magnet of the CMS detector is designed to achieve a 4 T magnetic field in a free bore of 6 m diameter and 12.5 m in length. To achieve the required magnetic field of 4 T, the 4-layer winding with the NbTi conductor is used to increase the number of ampere-turns for the solenoid. This powerful solenoid magnet is typically run at a field of 3.8 T to maximize its lifetime and at the same time provides sufficient bending power for charged tracks at high energy.

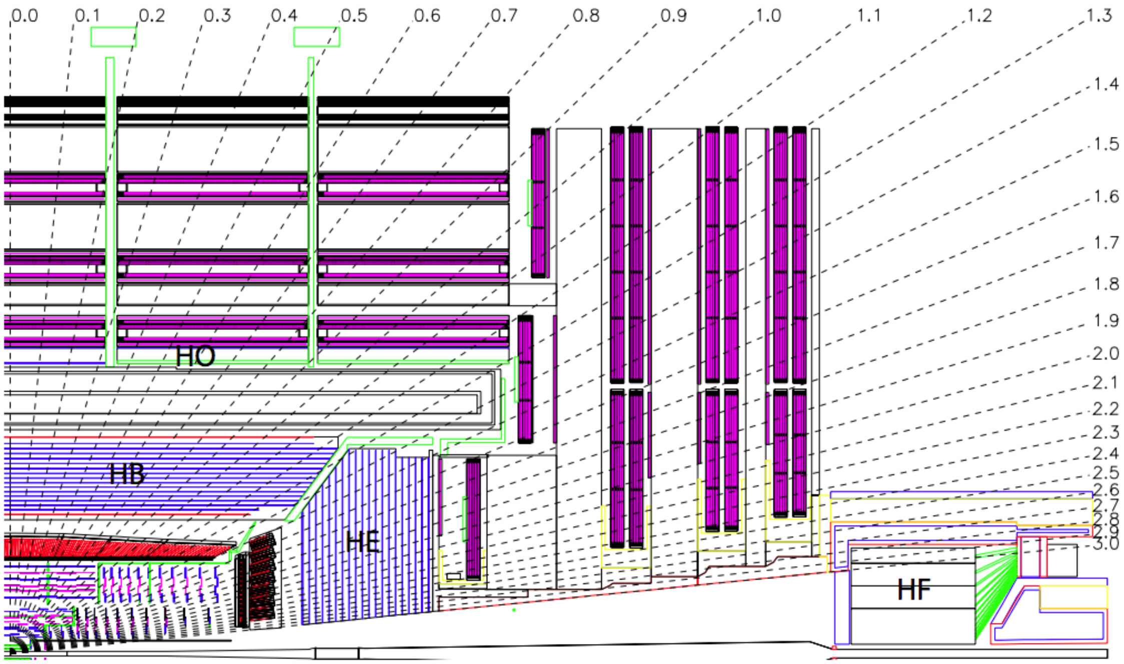

Figure 3.5.: Longitudinal view of the CMS detector showing the locations of the hadron barrel (HB), endcap (HE), outer (HO) and forward (HF) calorimeters. From [45].

3.2.5. The muon system

The layout of the muon system is shown in Figure 3.6. The muon system is composed of three types of gaseous particle detectors for muon identification, the drift tube (DT), resistive plate chamber (RPC) and cathode strip chamber (CSC) subsystems. As muons travel through the gas detectors, the gas is ionized. Free electrons produced from the ionization drift towards the anodes in the presence of the electric field and induce an electronic signal.

For the barrel region $|\eta| < 1.3$, the DT subsystem is used. This subsystem consists of four cylindrical stations around the beam line. Each chamber is filled with a mixture of Ar and CO_2 gas. The CSCs consist of chambers with a mixture of Ar, CO_2 and CF_4 gas, and cover the endcap region $0.9 < |\eta| < 2.4$. They aim to provide standalone precision muon measurement and muon trigger. They are required to operate at high rates of radiation and under large non-uniform magnetic fields. Last but not least, the RPCs cover the range $|\eta| < 2.1$. They are composed of bakelite plate electrodes with a 2 mm gas gap. They have poorer spatial resolution than the DTs and CSCs, but provide complementary timing resolution for precise decision of muon trigger timing and the bunch crossing from which the detected muons originate.

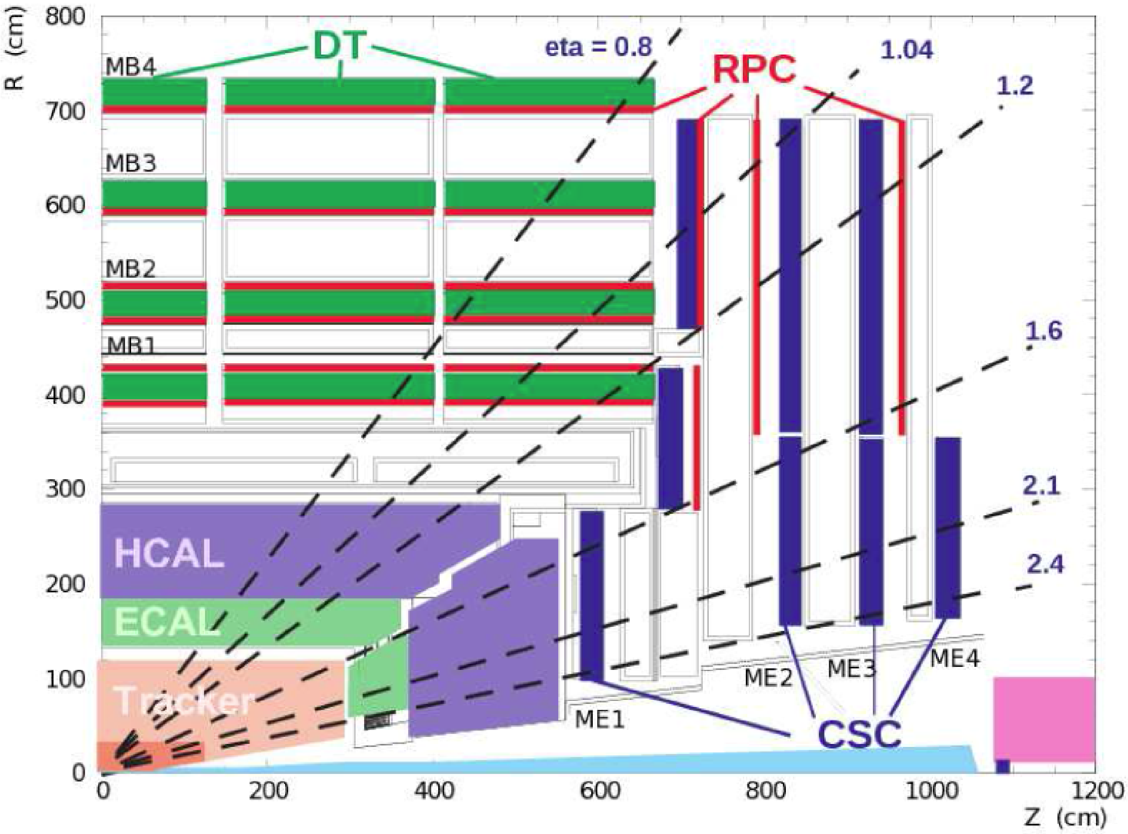

Figure 3.6.: A schematic of a quadrant of the CMS muon system. The locations of the Drift Tube (DT), Resistive Plate Chamber (RPC) and Cathode Strip Chamber (CSC) subsystems are displayed. From [45].

3.2.6. The Trigger system and data acquisition system

The rate of collisions at the LHC is 40 MHz. At such a high rate, it is too expensive to record information every collision from every bunch crossing. As most collisions produced are soft QCD processes due to the relatively large cross sections, a two-level trigger system is employed to discriminate against these soft QCD processes, and select and store interesting physics events using faster algorithms. It is crucial that the trigger algorithm can recognize and select nearly $\sim 100\%$ of interesting hard scattering events.

The CMS trigger system is composed of two decision layers, the Level-1 Trigger (L1T) and the High-level Trigger (HLT). The L1T serves as a first layer for event selection based on data received from the read-out pipelines. These are made from customized field programmable gate array (FPGA) boards. The L1T is designed to select events based on coarse data received from the read-outs of calorimeters and muon systems in a short time scale, as the read-out pipelines of the CMS detector can only store data from each bunch crossing for ~ 4 μs. This first layer trigger system is able to reduce the event rate from 40 MHz to 100 kHz. Figure 3.7 shows how the data from each subdetector readout are handled and passed to the Global Trigger (GT), which decides if each event would be passed to the second layer of the trigger system, HLT, for further discrimination.

The HLT is the second layer of the CMS trigger system. It receives a much reduced data rate from the L1T and has a larger latency window to exploit more information from the detector and make refined trigger decisions with more complex algorithms. The HLT is designed to select more effectively interesting physics processes that would not be impossible in the L1T stage. It reduces the data rate from ~ 100 kHz from the L1T to ~ 1 kHz.

Events that are accepted by both the L1T and HLT are marked and stored in the data storage infrastructure at CERN (Tier-0) for offline data analysis later. Accepted data are also transferred to each data storage site (Tier-1) around the world through the GRID computing infrastructure. Members of the CMS collaboration on different parts of the world can then access the data and perform offline analysis.

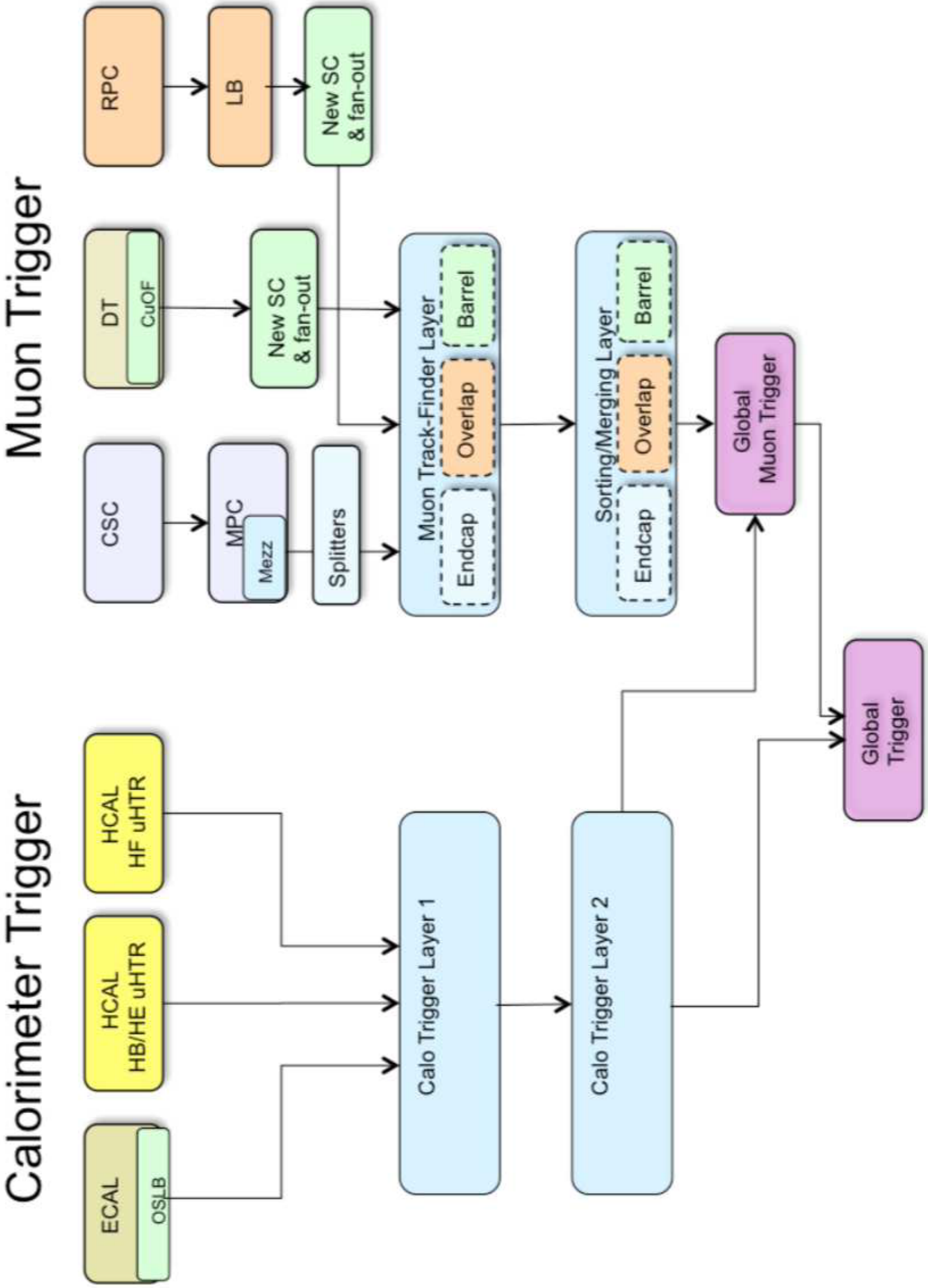

Figure 3.7.: Data passing to the L1T from each subdetector read-out. From [47].

Chapter 4.

Event reconstruction

4.1. Detector reconstruction

Raw information from each subdetector is combined to compute variables that approximate the properties of individual particles, groups of particles in an electromagnetic or hadronic shower, and the global event. Each subdetector uses its specific reconstruction algorithm to suppress noise, mitigate pile-up effects and provide accurate spatial, temporal or energy measurements. Precise measurements on these quantities are crucial for the optimal performance of the experiment under the challenging environment of the LHC collisions.

4.1.1. Track reconstruction

As charged particles pass through the tracker and induce ionization and energy deposits, hits are formed. Based on hit patterns registered by the tracker, trajectories of charged particles are reconstructed using the Combined Track Finder (CTF) algorithm [48]. It proceeds as follows: first of all, potential track candidates are seeded in the innermost tracker layer. Quality cuts are applied to reduce the number of fake tracks due to the combinatorics of hits. Tracks are then extrapolated to the next tracking layer with the Kalman filter method [49], which accounts for effects from energy losses and multiple scattering. The Kalman filter algorithm is mathematically equivalent to the least-squares minimization, and it is the optimal estimator for linear models with Gaussian noise. In case of non-linear models or models with non-Gaussian noise, it is still the optimal estimator but will be sensitive to outlying measurements. Recursive extrapolations and fitting of tracks are performed to subsequent tracker layers, until the outermost layer is reached or the track candidate does not satisfy track quality cuts. The track collection is then cleaned to avoid redundant tracks. The track finding algorithm is repeated up to six times for each event, and hits associated with reconstructed tracks in previous iterations are removed to reduce combinatorics.

4.1.2. Vertex reconstruction

Another important quantity to be reconstructed is the position of each proton-proton interaction, namely vertices. Dedicated algorithms are utilized to reconstruct vertices based on reconstructed tracks, clustering and vertex fitting. Tracks with good quality are selected by applying requirements on the χ^2 of the track fits and the minimum numbers of hits. The transverse impact parameters of these tracks are also required to be $< 5\sigma$ with respect to the beamspot. Candidate vertices are seeded by two or more tracks with separation in the z-coordinate $z < 1$ cm.

Other tracks are then associated to candidate vertices using the Deterministic Annealing algorithm [50]. The algorithm performs track selection, clustering and fitting of vertex positions. Finally, the spatial position of each candidate vertex is extracted by the Adaptive Vertex fitter [51]. The fitter determines the most probable spatial position of each vertex based on input track information associated with each candidate vertex. Quality cuts are further applied to each candidate vertex to reject fake vertices.

Once vertices are defined, the primary vertex (PV), which corresponds to the interaction with the hardest scattering in the event, is selected. The PV is defined as the vertex with the greatest sum of square of physics object momenta associated with the vertex, with physics objects defined as objects returned by the jet finding algorithm [52, 53] with inputs of all charged tracks associated with the vertex and corresponding $\vec{p}_{\text{miss}} = -\sum_{i \in \text{tracks}} \vec{p}_i$. Other vertices are defined as the PU vertices.

4.1.3. Calorimeter reconstruction

The primary goal of calorimeters is to accurately measure energies of particles from the collisions. Complementarily, they can also be used to provide additional tracking information for charged particles. To measure properties of incident particles precisely, measurements from different towers and crystals in the calorimeters must be clustered and calibrated [46, 54]. Reconstruction algorithms of the calorimeters access signal pulses in each cell or tower in multiple 25ns steps (time-slice) and convert these measurements to a single number of measured energy. Signal pulses in previous or later time-slices can be increased by the presence of particles from collisions in previous or later bunch crossing (out-of-time pile-up, OOTPU). Since Run 2, an algorithm utilizing a template fit method [55] is employed in ECAL energy reconstruction to minimize the effects from out-of-time PU, with signal templates measured in low PU conditions. A similar algorithm is also used for HCAL energy reconstruction [56]. Since 65% (95%) of signals in HB and HE are contained in one (two) time slice, pulses templates are fitted to the triggered, previous and later bunch crossing with amplitudes and arrival time of signal as free parameters. Figure 4.1 shows the relative energy response of the energy reconstruction algorithm for HCAL, defined as reconstructed hit energy divided by simulated hit energy, against simulated hit energy.

4.2. Physics object reconstruction

4.2.1. Muon reconstruction

Muons, as minimally ionizing particles, travel across the CMS detector without losing a lot of their energy. Three reconstruction algorithms, based on hit information from the tracker and the muon system, are employed: the 'outside-in' global muon algorithm, 'inside-out' tracker muon algorithm [57], and the PF-Muon algorithm described in Section 4.3. Each algorithm provides complementary information and the combination maintains high reconstruction efficiencies across various muon energies. Muons are required to be reconstructed by at least one of the three algorithms mentioned above.

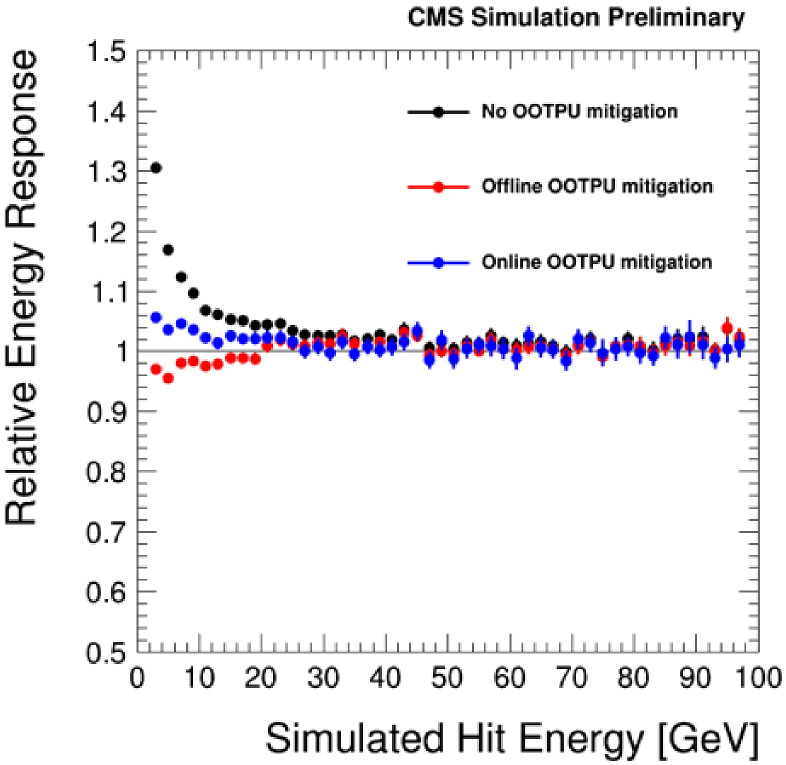

Figure 4.1.: Relative energy response in the collision condition of 20 PU and 25 ns bunch crossing. No OOPU mitigation uses only sum of signal in the triggered and later time slices without correction to OOTPU. Online (Offline) OOTPU mitigation is the energy reconstruction algorithm using template fits for HLT (offline) reconstruction. From [56].

The global muon algorithm starts with hits from muon chambers and reconstructed muon tracks and their initial estimate of energy deposited. Muon tracks are then extrapolated back to the tracker using the Kalman filter. The algorithm searches for possible tracks for matching with the muon tracks. Matched tracks with good fits with the Kalman filter algorithm are considered as muon candidates. This reconstruction algorithm provides high reconstruction efficiency for muons with higher momentum that can travel across the detector.

The tracker muon algorithm, instead, uses tracks reconstructed based on hits in the tracker with $p_T > 0.5$ GeV as seeds. Seed tracks are then extrapolated to the muon system using a Kalman filter. Tracks that are matched to at least one hit in the muon chamber are considered to be muon candidates. This algorithm provides a better performance for the reconstruction of low-p_T muons.

Furthermore, selections on the χ^2 of the muon track fit, the number of tracker hits, transverse and longitudinal impact parameters are used to reconstructed muon candidates to reduce backgrounds from hadronic punch-through and non-prompt muons while maintaining a good reconstruction efficiency.

4.2.2. Electron and photon reconstruction

Electrons and photons interact with the ECAL in a very similar mechanism, and hence similar reconstruction algorithms are used for these two physics objects. Photons, however, do not leave tracks in the tracker and lose energy like electrons do. For example, electrons lose on average 33% of the energy before entering the ECAL through bremsstrahlung [58]. To properly account for energy deposition, photons produced during bremsstrahlung have to be clustered. Clustering in the ECAL is allowed to extend in the azimuthal direction, as trajectories of electrons can bend in the magnetic field but those of photons produced from bremsstrahlung do not.

In particular, electron energy usually spreads over multiple crystals in the ECAL. For example, electrons with 120 GeV deposit about 97% of the energy in a 5×5 crystal array [43]. A hybrid clustering algorithm is utilized to form superclusters in the barrel region. The procedure is as follows:

- Crystals with energy above the minimum threshold are used as seeds.
- Arrays of adjacent 5×1 ($\Delta\eta \times \Delta\phi$) crystals (up to 17 arrays in both positive and negative ϕ direction) are added to the seed crystal in the ϕ direction, if their energies are above 0.1 GeV.
- Arrays are further clustered to form superclusters such that each supercluster contains at least 0.35 GeV.

The reconstruction algorithm for the endcap region is similar but uses 5×5 array of crystals. Positions of superclusters are then matched to tracks from the primary vertex. Superclusters with successful matching are considered as electron candidates and ones with unsuccessful matching as photon candidates. Various kinematic cuts are applied to electrons and photon candidates to reject backgrounds from mis-reconstructed jets, photon conversion and semi-leptonic decay of heavy quarks. These include the ratio of energy depositions in ECAL to HCAL, impact parameters and distances of matched tracks to the primary vertex (in case of electron candidates), the shower shape and cluster width variable.

4.3. Particle-flow reconstruction

The particle-flow (PF) algorithm aims at reconstructing all stable particles produced at the LHC (γ, $e^{\pm}$, $\mu^{\pm}$, $\pi^{\pm}$, $K^{\pm}$, K^0, $p^{\pm}$ and n) by combining information from all sub-detectors. Exploiting full information from every sub-detector improves significantly the measurements of energies and trajectories of particles with only subset of subdetectors. Reconstructed stable particles from the algorithm are then used to construct jets as described in Section 4.6, compute missing transverse momentum $\not{E}_T$, reconstruct hadronically-decaying τ, tag b-jets etc.

The algorithm relies on reliable measurements from each sub-detector for the best possible reconstruction performance and the CMS detector is well-suited with this requirement. Charged tracks are reconstructed by the tracker with high efficiency and small fake rates due to accurate silicon tracker measurements in a strong magnetic field of $3.8T$ provided by the superconducting solenoid. Excellent energy resolutions are achieved by the high granularity ECAL with $PbWO_4$ crystals which provides excellent performance on photon identification in a challenging environment with high particle density.

Each stable particle leaves specific signatures in the CMS detector and give rise to various possible combinations of PF elements such as charged-particle tracks, calorimeter clusters or muon tracks. A dedicated algorithm is designed to connect each PF element, fully reconstruct each stable particle based on PF elements and avoid any double counting of PF elements in reconstruction of different particles. The detailed procedure of the algorithm is as follows:

- Global muons defined in Section 4.2.1 are classified as PF muons, if the combined measurement of p_{T} is compatible with the measurement with the tracker alone within three standard deviations. The corresponding track to each global muon is masked and not used for later stages of the algorithm. Expected energy deposits in the calorimeters by each PF muons are also corrected for.

- Tracks pre-identified in the tracker are fitted with the Gaussian-sum filter (GSF) algorithm [59] and extrapolated to the ECAL. Additional quality cuts on the tracking calorimetric variables are applied to define PF electrons. Similar to PF muons, corresponding tracks and ECAL clusters to the PF electrons are masked for later stages of the algorithm.
- Remaining tracks in the tracker are then matched to clusters in ECAL and HCAL. A PF charged hadron is defined in cases of successful matching. The identification of neutral particles involves the comparison of the momentum from tracks and the measured energy from the calorimeters. If the measured calorimetric energy is significantly larger than the calculated energy from the track momentum under the charged pion mass hypothesis, a PF photon and possibly a extra neutral hadron is defined, depending on the excess of the energy.
- Remaining clusters in the calorimeters are considered as PF photons or PF neutral hadrons.

4.4. Pile-up estimation

Contamination from PU events has to be accurately estimated and corrected for in the event reconstruction algorithm. Charged particles from PUs can be distinguished by whether their tracks originate from the primary vertex. For neutral particles which leave no tracks in the detector, their PU contamination can be estimated from the data-driven energy ratio of neutral to charged particles from PUs (the $\delta\beta$ correction) [60]. In addition, PU contamination can be subtracted by utilizing the energy density of PU ρ_{PU}. For each particle, the corrected transverse momentum can be calculated as:

$$p_{\mathrm{T}_i}^{\mathrm{corr}} = p_{\mathrm{T}_i}^{\mathrm{raw}} - \rho_{\mathrm{PU}} \times A_i \tag{4.1}$$

where A is the active area of the particle i. The energy density is estimated by dividing the detector in a square grid of cells where the average energy density of all PF particles in each cell is determined [53, 61]. This mechanism, called the effective area (EA) correction, essentially corrects contamination from both charged and neutral particles coming from PUs.

4.5. Isolation

Another important aspect of the reconstruction algorithm is to distinguish between prompt and non-prompt leptons, which arise from leptonic decays of b(c)-hadrons. An effective way to distinguish between the two is to examine the hadronic activity around the lepton. It is measured by the isolation of the lepton, defined as the ratio of the total energy of particles within a cone around the lepton to the energy of the lepton. The standard method to compute isolation in the CMS experiment is the PF relative isolation $I_{\mathrm{PF}}^{\mathrm{rel}}$, defined as:

$$I_{\mathrm{PF}}^{\mathrm{rel}} = \frac{1}{p_{\mathrm{T}\ell}} \times \left(\sum_{\mathrm{PF_{PV}}} {p_{\mathrm{T}}}^{\mathrm{CH}} + \sum_{\mathrm{PF}} {p_{\mathrm{T}}}^{\mathrm{NH}} + \sum_{\mathrm{PF}} {p_{\mathrm{T}}}^{\gamma} - \sum_{\mathrm{PU}} {p_{\mathrm{T}}}^{\mathrm{Neutral}} \right) \tag{4.2}$$

where $p_{\mathrm{T}\ell}$, ${p_{\mathrm{T}}}^{\mathrm{CH}}$, ${p_{\mathrm{T}}}^{\mathrm{NH}}$, ${p_{\mathrm{T}}}^{\gamma}$ are the transverse momentum of the lepton, charged hadrons, neutral hadrons and photons respectively. The last term represents contributions to hadronic activity from neutral PU particles. Two methods are used in the CMS experiment to estimate this component, the $\Delta\beta$ correction and EA correction as described in Section 4.4.

4.6. Jet reconstruction

The most likely outcome of proton-proton collisions is by far the production of quarks and gluons. Upon production, high p_{T} quarks and gluons hadronize due to confinement and this results in a set of collimated showers of stable particles such as hadrons, leptons and photons in a cone, leading to a jet. Special clustering algorithms are developed to reconstruct each shower from a set of stable particles as jets [62].

4.6.1. Jet clustering

Soft or collinear emission from gluons and quarks can introduce infrared divergence in perturbative QCD [63]. Any jet clustering algorithm has to be insensitive to soft and collinear splitting of colored particles, i.e. infrared and collinear safe. To achieve this, CMS uses a sequential recombination algorithm [64] that fulfills infrared and collinear safety. In the algorithm, inter-particle distances are defined for each pair of particles as

$$d_{ij} = min\left[{p_{\mathrm{T}}}_i^k, {p_{\mathrm{T}}}_j^k\right] \times \left(\frac{\Delta R_{ij}}{R}\right)^2 \tag{4.3}$$

and beam-particle distances are defined for each particle as

$$d_{iB} = {p_{\mathrm{T}}}_i^k \tag{4.4}$$

where $k = -2, 0, 2$, ΔR is the separation of the particle i and j in the $\eta - \phi$ plane and R is a fixed parameter chosen to define the jet cone size. The procedure of the algorithm is as follows:

- Calculate d_{ij} for each pair of particles i, j and d_{iB} for each particle i.
- Rank all distances d_{ij}, d_{iB}
- If the smallest distance is an inter-particle distance, combine the pair of particles into one particle and repeat the calculation of distances and ranking again
- If the smallest distance is a beam-particle distance, classify this particle as a final cluster and repeat the calculation of distances and ranking again but ignoring this cluster.
- Repeat procedures above until there are no particles left for clustering.

The commonly used anti-k_T algorithm [52], with $k = -2$, is used in this thesis, with the jet cone size $R = 0.4$. The choice of jet cone size is made such that most hadronic showers from the hadronization of gluons and quarks in 13 TeV proton-proton collisions are contained while maintaining an efficient cone size to reduce PU contamination. The CMS experiment uses the FASTJET package [53] for jet clustering, with PF candidates described in Section 4.3 as inputs.

4.6.2. Jet identification

Additional requirements on jet properties are applied to each jet candidate after clustering to reduce backgrounds with fake jets or detector noise. Various set of selections are used in CMS [65]. In this analysis the loose set of selections are utilized, which provides high efficiency $\sim 100\%$ for jet identification while maintaining reasonable rejection rates $\sim 84\%$ for fake jets. The selection requires at least two PF candidates, the energy fraction of neutral hadrons and photons in each jet $< 99\%$, the energy fraction of charged hadrons in each jet $> 0\%$ and charged hadron multiplicity in each jet > 0.

4.6.3. Jet energy correction

The measured transverse momentum ${p_{\mathrm{T}}}^{\mathrm{raw}}$ of a jet could be different from the partonic energy of the quark or gluon, due to hadronization effects, variations in resolution in different parts of the detector, and failed reconstruction in uninstrumented sessions of the detector. To correct for this difference, a correction is parametrized as [66]

$$ {p_{\mathrm{T}}}^{\mathrm{corr}} = C_{\mathrm{offset}}({p_{\mathrm{T}}}^{\mathrm{raw}}) \times C_{\mathrm{rel}}(\eta) \times C_{\mathrm{abs}}({p_{\mathrm{T}}}^{'}) \times C_{\mathrm{res}}({p_{\mathrm{T}}}^{''}, \eta) \times {p_{\mathrm{T}}}^{\mathrm{raw}} \tag{4.5} $$

where C_{offset}, C_{rel}, C_{abs} and C_{res} represent the offset, relative, absolute and residual correction respectively. ${p_{\mathrm{T}}}^{\mathrm{corr}}$ and ${p_{\mathrm{T}}}^{\mathrm{raw}}$ are the corrected and uncorrected transverse momentum of a jet respectively. ${p_{\mathrm{T}}}^{'}$ is the transverse momentum of the jet after applying offset and relative corrections and ${p_{\mathrm{T}}}^{''}$ is the transverse momentum of the jet after applying all correction except the residual correction. The offset correction aims to remove contributions from PU jets. Charged PF candidates not originating from the primary vertex are removed before the clustering, and contaminations from neutral hadrons are estimated by jet area subtraction as described in Section 4.4. The relative correction, derived from multi-jet QCD MC simulation, gives a uniform jet energy response in η. The absolute correction, derived from $Z+$jets and $\gamma+$jets data samples, is used to correct jet energy response, defined as $\frac{p_T{}^{\text{jet}}}{p_T{}^{\gamma/Z}}$, as a function of jet p_T. The boson p_T in $Z+$jets and $\gamma+$jets sample, which can be accurately measured, is used to calibrate the reconstructed energy of the recoiling jets. The residual correction accounts for the difference in jet energy response between data and MC as a function of p_T and η.

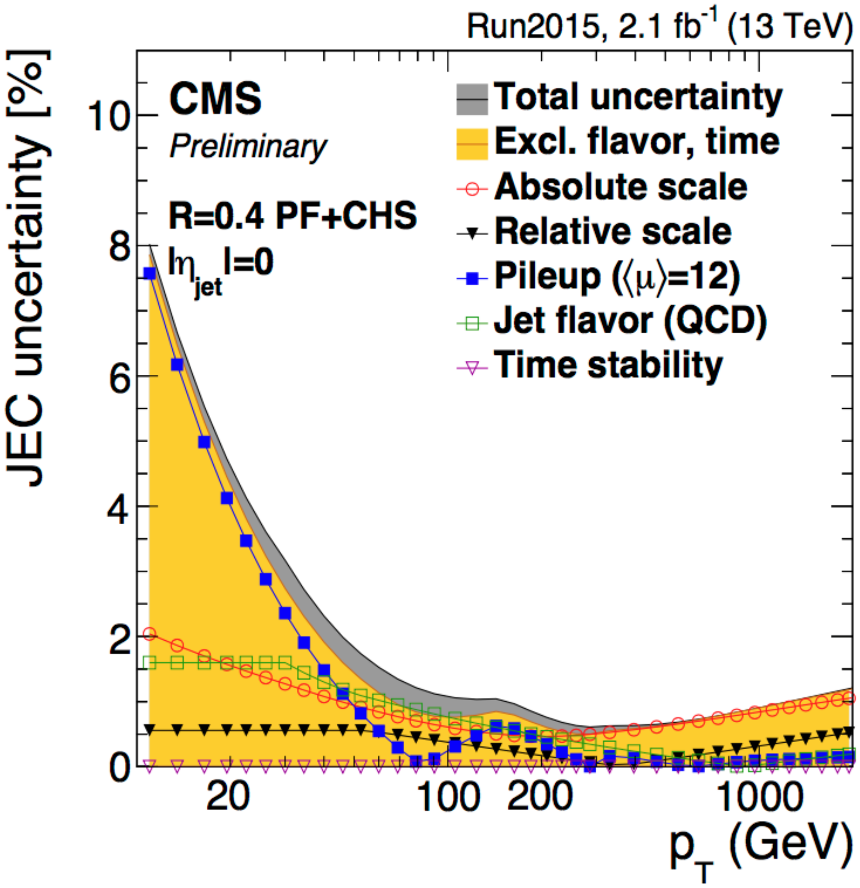

Figure 4.2.: Systematic uncertainty of jet energy correction for Equation 4.5. The gray band shows the total uncertainty of the correction. The PU uncertainty dominates for jet $p_T < 50$ GeV. From [67].

Sample	Definition
Multijet	At least one jet with $p_{\mathrm{T}_{\mathrm{jet}}} > 40$ GeV
Muon enriched jets	At least two jet with $p_{\mathrm{T}_{\mathrm{jet}}} > 20$ GeV At least one jet with a muon with $p_{\mathrm{T}_{\mu}} > 5$ GeV
Dileptonic t$\bar{\mathrm{t}}$	At least two jet with $p_{\mathrm{T}_{\mathrm{jet}}} > 20$ GeV One isolated muon or electron with $p_{\mathrm{T}_{\ell}} > 20$ GeV

Table 4.1.: Summary of event selections for each sample used to validate the b-tagging algorithm. From [68].

4.6.4. B-tagging

Due to the relatively long lifetime (~ 1.5 ps [9]) of b-hadrons, they typically travel a distance of ~ 450 μm before decaying. The high-resolution tracker can therefore resolve displaced vertices. Secondary vertices and the possible presence of muon or electrons from leptonic decay of b-hadrons can be used to identify jets hadronized from b-quarks (b-jets). CMS uses various dedicated algorithms to exploit the features mentioned above for robust performance of b-tagging [68]. In this thesis the Combined Secondary Vertex version 2 (CSVv2) algorithm is used. The algorithm combines information of secondary vertices and lifetime of each jet with a neural net and gives a likelihood value of the jet arising from a b-quark. A discriminator of value greater than 0.8989 is chosen to identify b-jets, corresponding to an efficiency of $\sim 67\%$ and a mis-tag rate of $\sim 10\%$ and $\sim 1\%$ for charm-jets and light jets (u, d and s quarks) respectively [69]. Difference in efficiency between data and MC is measured in each jet p_{T} and η bin with the multijet, muon enriched jets and dileptonic t$\bar{\mathrm{t}}$ sample [68]. Table 4.1 shows the definition of event selection for these three samples. Figure 4.3 shows the distribution of the CSVv2 discriminator in the multijet, muon enriched jets and dileptonic t$\bar{\mathrm{t}}$ samples.

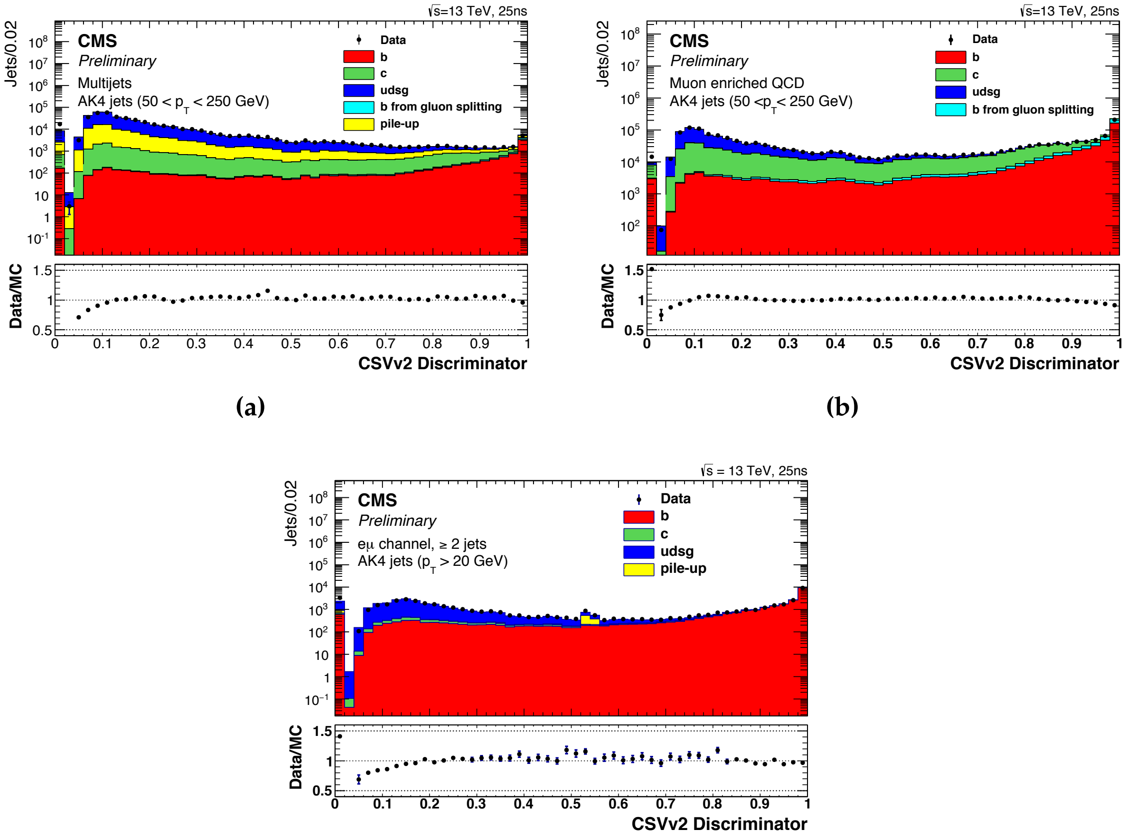

(a) **(b)**

(c)

Figure 4.3.: Distribution of CSVv2 discriminator for multijet (4.3a), muon enriched jets (4.3b) and dileptonic $t\bar{t}$ sample (4.3c). From [68].

4.7. Event-wide characteristic energy variables

To maximize sensitivity to potential SUSY signatures, several variables are utilized to categorize events based on event kinematics. SUSY models typically have high mass scales and decay of sparticles lead to significant visible and invisible energy in the final states.

To approximate the visible energy scale of a event, one can define the total transverse energy of a event as the scalar sum of all the reconstructed PF candidates

$$H_T = \sum_{i \in \mathrm{PF}} |E_{\mathrm{T}i}| \tag{4.6}$$

and the total hadronic transverse energy H_T can be calculated as the scalar sum of all reconstructed jets

$$E_{\mathrm{T}} = \sum_{i \in \text{jets}} |E_{\mathrm{T}i}| \tag{4.7}$$

For hadronic final states, the two variables provide complementary information and are similar to each other

To quantify the invisible energy scale of a event, one common choice of kinematic variables is the missing transverse momentum $\not{E}_T$, which is computed as the negative sum of the transverse momenta of all PF candidates

$$\not{E}_T = -\sum_{i \in \mathrm{PF}} p_{\mathrm{T}i} \tag{4.8}$$

Similarly, a similar quantity $\not{H}_T$ can be defined with only reconstructed jets in the event

$$\not{H}_T = -\sum_{i \in \text{jets}} p_{\mathrm{T}i} \tag{4.9}$$

$\not{E}_T$ can be biased by various detector effects, such as minimum energy threshold in calorimeters, inefficiencies in the tracker, non-linearity in calorimeter response. These effects are mitigated by correcting the p_{T} of the jets to the particle level by jet energy correction

$$\vec{\not{E}}_T^{\text{corr}} = \vec{\not{E}}_T - \sum_{i \in \text{jets}} (\vec{p}_{\mathrm{T}}^{\,\text{corr},i} - \vec{p}_{\mathrm{T}}^{\,i}) \tag{4.10}$$

where $\vec{\not{E}}_T^{\text{corr}}$ refers to the corrected $\vec{\not{E}}_T$ quantity and $\vec{p}_{\mathrm{T}}^{\,\text{corr},i}$ is the corrected p_{T} for jet i. The correction uses corrected jets with $p_{\mathrm{T}} > 15$ GeV and with less than 0.9 of their energy deposited in the ECAL. If a muon is inside a jet, the correction is applied to the jet momentum subtracted with the muon momentum [70]. Figure 4.4 shows the corrected $\not{E}_T$ distribution for the $\gamma +$ jets samples with statistical and systematic uncertainty from JEC displayed.

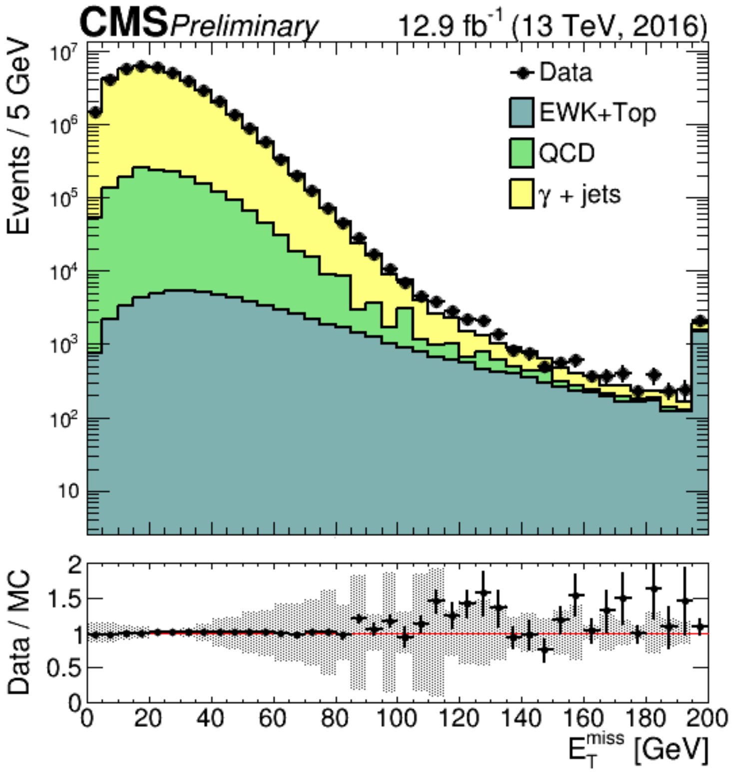

Figure 4.4.: Distribution of the $\not{E}_T$ distribution of $\gamma +$ jets events. Statistical uncertainty of data and MC simulation are included in the lower panel of the plot. The systematic uncertainty from JEC is also shown. The EWK component refers to the diboson, $Z\gamma$ and $W\gamma$ production. From [70].

Chapter 5.

The α_T analysis

The α_T analysis is a search for BSM physics, targeting pair production of colored SUSY particles which decay to LSPs leaving the detector undetected. The signal region of the analysis is selected as a final state of at least one jet and significant $\not{E}_T$, with no reconstructed leptons or photons.

The α_T analysis is a well established analysis since Run 1, providing public results at both $\sqrt{s}$ = 7 TeVand $\sqrt{s}$ = 8 TeVand several luminosities. Increases in center of mass energies from 8 TeVin Run 1 to 13 TeVin Run 2 significantly enhanced the cross sections of SUSY processes [36], and new techniques and strategies have been designed to exploit this gain.

Extraction of the signal requires a thorough understanding of the background. Various backgrounds are detailed in Section 5.1. One of the dominant backgrounds in hadronic analyses is QCD multijet production, which arises primarily from mismeasurements of jet energies. Dedicated variables are used to strongly suppress this background, as detailed in Section 5.2. Definitions of the signal region, and two control regions are described in Section 5.4. Furthermore, events which pass the signal region or control region selections are categorized according to four kinematic variables to optimize sensitivities. The categorization is described in Section 5.5. Finally, the trigger strategy is discussed in Section 5.3.

5.1. Backgrounds

5.1.1. QCD multijet background

The QCD multijet background is dominant in hadronic analysis. This final state consists of a balanced system of multijet events, with no genuine $\not{E}_T$ signature. However, jet energy mis-measurements due to fluctuations in detector response or reconstruction can induce fake $\not{E}_T$ signatures and hence constitute a significant proportion of total background in the signal region, due to the much larger cross sections of the multijet background than other SM backgrounds with genuine $\not{E}_T$ signatures [36]. Various mechanisms that induce jet energy mis-measurements are described below:

- Jets with outgoing directions pointing to regions with significant detector inefficiencies with reduced or no response can cause significant loss in measurement of energies.
- Additional fake energy could be added in jet energy measurements due to the presence of 'hot cells' in ECAL and HCAL, spontaneous discharges and direct particle interactions with detector electronics or photomultipliers.
- 'Beam halo' from LHC beam scattering off collimators can interact with the muon system and cause fake reconstructed muons, or interact with the calorimeters and deposit additional energy causing imbalance in transverse momenta [71].
- Imbalance in transverse momenta could be caused by acceptance effects due to finite detector resolutions.

In addition, QCD multijet background could have a small proportion of events with genuine $\not{E}_T$, due to production of heavy flavor quark decaying into leptons and neutrinos. These events could pass the signal region requirements as the leptons usually reside within the jet cone and fail isolation requirements.

5.1.2. Electroweak backgrounds

Besides QCD multijet background, various SM processes with neutrinos in the final state, labeled as electroweak background, can mimic signatures in the signal region and constitute a significant portion of background in hadronic searches.

In general for hadronic searches, the dominant backgrounds are $\mathrm{W} + \mathrm{jets}$, $\mathrm{t\bar{t}} + \mathrm{jets}$ and $\mathrm{Z} + \mathrm{jets}$. They are detailed as follows specifically for the case of the α_T analysis.

$\mathrm{Z} + \mathrm{jets}$ background

The largest background process in the signal region after QCD multijet rejection is the $\mathrm{Z} + \mathrm{jets}$ production, with the Z boson decaying to neutrinos, $\mathrm{Z} \rightarrow \nu\bar{\nu}$. This background is irreducible as the final state constitutes no leptons and significant $\not{E}_T$ from neutrinos escaping the detector undetected. Across signal regions, it contributes $\approx 50\%$ of the overall background. Similarly, the $\mathrm{Z} + \mathrm{jets}$ production but with Z decaying into two leptons, in which only one or both of them are lost due to failed reconstruction, can enter the signal region. However, due to the low probability of losing one or both of the leptons, this is a subdominant background, constituting only $\approx 0.5\%$ of the total background.

$\mathrm{W} + \mathrm{jets}$ background

One of the dominant backgrounds is the production of a W boson in association with jets ($\mathrm{W} + \mathrm{jets}$) with the W boson decaying leptonically ($\mathrm{W} \rightarrow \ell\nu$) and the lepton is not reconstructed, sometimes also labeled as lost lepton background. This background can enter the signal region if the lepton is out of acceptance or fails the isolation requirements or reconstruction, as both the lost lepton and neutrino contribute to $\not{E}_T$. The $\mathrm{W} + \mathrm{jets}$ background comprises $\approx 40\%$ of the overall background in the signal region. In addition, the $\mathrm{W} + \mathrm{jets}$ background can also enter the signal region with the W boson decaying into a hadronically decaying τ reconstructed as a jet.

$\mathrm{t\bar{t}}+$ jets and single top background

The $\mathrm{t\bar{t}}+$jets and single top background consist of around 5% and 0.5% of the overall background. Top quarks predominantly decay as $t \to Wb$. The two W bosons may then decay hadronically or leptonically. In the case of two W bosons decaying hadronically, $\not{E}_T$ may be introduced by jet energy mis-measurement or bottom quarks decay via neutrinos. In the case of one W boson decaying leptonically, similar to W + jets background, $\not{E}_T$ can arise from the neutrino and lost lepton. In the case of two W boson decaying leptonically, the final state consists of two leptons and significant $\not{E}_T$. This final state is subdominant due to low probability of losing or misreconstructing both leptons.

As detailed in Section 5.5, the α_T analysis categorizes events with the number of reconstructed jets originating from bottom quarks. The $\mathrm{t\bar{t}}+$jets backgrounds constitutes a dominant background for $N_b \geq 2$.

Single top backgrounds occur via t-channel in association with a quark, in association with a W boson, or s-channel in association with a bottom quark.

Residual electroweak backgrounds

In addition to dominant backgrounds described above, there are several processes with minor contributions to the signal region. They include $\mathrm{t\bar{t}}$ production in association with a vector boson ($\mathrm{t\bar{t}W}$, $\mathrm{t\bar{t}Z}$), pair production of vector bosons (WW, ZZ, WZ), and production of lost photons in association with jets.

5.2. QCD background suppression

The QCD background predictions present significant challenges. One of the distinguishing features of the α_T analysis is to mitigate such difficult background with robust kinematic variables while maintaining good acceptance to a broad range of SUSY models. This is achieved by using four selections, α_T, $\Delta\phi^*_{\mathrm{min}}$, $\not{H}_T/\not{E}_T$ and forward jet veto, as detailed in the following sections.

5.2.1. The α_T variable

The α variable was originally proposed in [72], and converted into a transverse variable, α_T, for hadronic collisions. It is designed to discriminate against events with significant $\not{E}_T$ originated from jet mis-measurement, such as QCD multijet background as described in Section 5.1. For dijet events, α_T is defined as

$$\alpha_T = \frac{E_{\mathrm{T}}{}^{\mathrm{j}_2}}{M_{\mathrm{T}}} \tag{5.1}$$

where $E_{\mathrm{T}}{}^{\mathrm{j}_2}$ is the transverse energy of the less energetic jet and M_{T} is the transverse mass formed by these two jets, defined as:

$$M_{\mathrm{T}} = \sqrt{\left(\sum_{i=1}^{2} E_{\mathrm{T}}{}^{\mathrm{j}_\mathrm{i}}\right)^2 - \left(|\sum_{i=1}^{2} \vec{p}_{\mathrm{T}}^{\,\mathrm{j}_\mathrm{i}}|\right)^2} \tag{5.2}$$

and $E_{\mathrm{T}}{}^{\mathrm{j}_\mathrm{i}} = E^{\mathrm{j}_\mathrm{i}} \sin\theta$ is the transverse energy of jet j_i and $\vec{p}_{\mathrm{T}}^{\,\mathrm{j}_\mathrm{i}}$ is the transverse momentum of jet j_i.

For events with three or more jets, a pseudo-dijet sytem is defined by clustering the jets into two pseudo-jets. The E_{T} for each of the pseudo-jet is the scalar sum of E_{T} of its contributing jets, and the pseudo-jets are combined such that ΔE_{T}, the difference in their E_{T} is minimized. Hence the transverse energy of the sub-leading pseudo-jet is given by:

$$E_{\mathrm{T}}{}^{\mathrm{j}_2} = \frac{\sum_i E_{\mathrm{T}}{}^{\mathrm{j}_\mathrm{i}} - \Delta E_{\mathrm{T}}}{2} \tag{5.3}$$

where $\Delta E_{\mathrm{T}} = |E_{\mathrm{T}}{}^{j_1} - E_{\mathrm{T}}{}^{j_2}|$ and M_{T} as:

$$M_{\mathrm{T}} = \sqrt{\left(\sum_i E_{\mathrm{T}}{}^{\mathrm{j}_\mathrm{i}}\right)^2 - \not{H}_T^2} \tag{5.4}$$

and hence the generalized definition for the α_T variable is

$$\alpha_T \approx \frac{\sum_i {E_{\mathrm{T}}}^{\mathrm{j_i}} - \Delta E_{\mathrm{T}}}{2\sqrt{\left(\sum_i {E_{\mathrm{T}}}^{\mathrm{j_i}}\right)^2 - \not{H}_T^2}} \tag{5.5}$$

In most cases, jets in signal regions are boosted such that $E_{\mathrm{T}} \approx p_{\mathrm{T}}$, and equation 5.5 can be written as

$$\alpha_T = \frac{H_T - \Delta H_T}{2\sqrt{H_T^2 - \not{H}_T^2}} \tag{5.6}$$

where $H_T = \sum_{i=1}^{N_{\mathrm{jet}}} {p_{\mathrm{T}}}^{\mathrm{j}_i}$, where N_{jet} is the number of jets within the experimental acceptance and $\not{H}_T = |\sum_{i=1}^{N_{\mathrm{jet}}} \vec{p}_{\mathrm{T}}^{\,\mathrm{j}_i}|$. For dijets events, there are three possible scenarios for the α_T variable, as shown in Figure 5.1. For balanced events without mis-measurements of jet energy, $\not{H}_T = 0$ and $\Delta H_T = 0$ and hence $\alpha_T = 0.5$. For balanced events with mis-measurement on one of the jets, $\not{H}_T \approx \Delta H_T$ and from equation 5.6,

$$\alpha_T = \frac{1}{2}\sqrt{\frac{H_T - \not{H}_T}{H_T + \not{H}_T}} < 0.5 \tag{5.7}$$

And finally for typical SUSY events with a genuine $\not{E}_T$ signature and other jets recoiling against it, $\alpha_T > 0.5$.

An α_T distribution before selection is shown in Figure 5.2. Events with $\alpha_T < 0.5$ are dominated by QCD multijet background, while for $\alpha_T > 0.5$, the QCD multijet background drops sharply due to reasons explained above. Occasionally the multijet background with very rare stochastic fluctuation in measured jet energies, or significant mis-measurements of more than one jet in the events can lead to $\alpha_T > 0.5$, these contribute to $< 1\%$ in the total background for the region beyond $\alpha_T > 0.5$. On the other hand, the drop in electroweak backgrounds for the region beyond $\alpha_T > 0.5$ is much more gradual due the the presence of genuine $\not{E}_T$ signatures in the events.

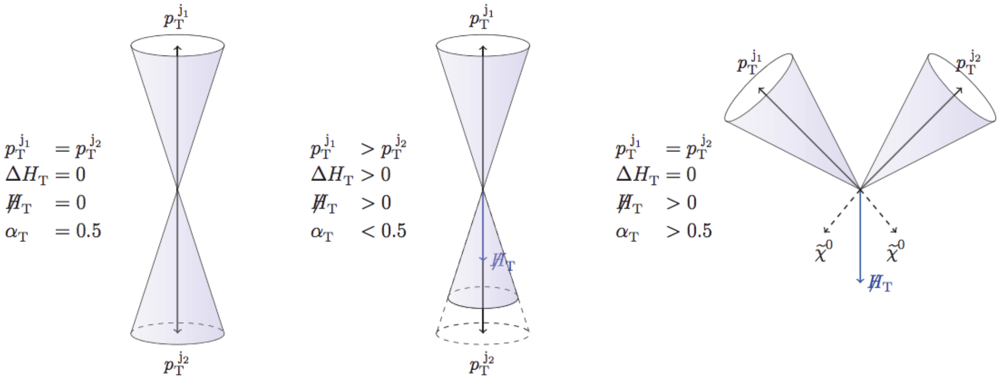

Figure 5.1.: Three possible scenarios for the α_T variable in a dijet event: balanced without mis-measurement (left), balanced with mis-measurement (middle), genuine $\not{E}_T$ (right). From [73].

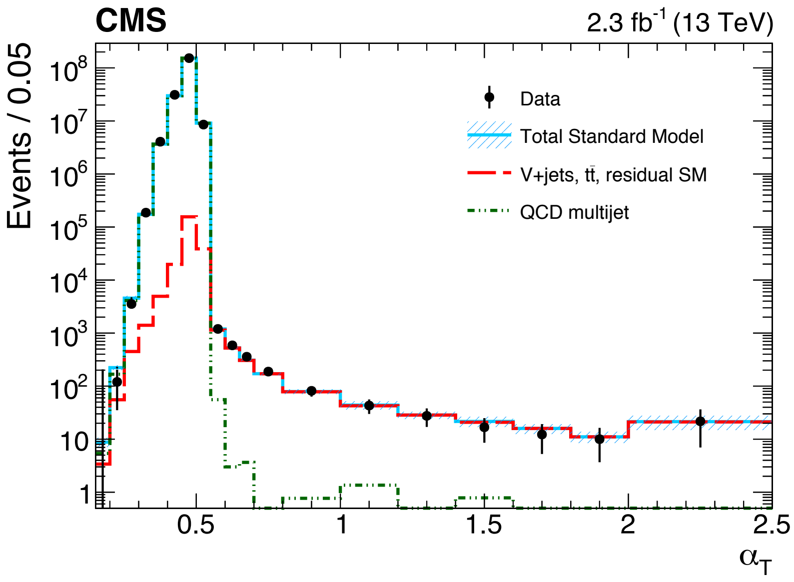

Figure 5.2.: The α_T distribution with data compared to simulation.

5.2.2. The $\Delta\phi^*_{\min}$ variable

In addition to the α_T variable as described in Section 5.2.1, a variable $\Delta\phi^*_{\min}$ is designed to mitigate QCD multijet backgrounds from various reconstruction and instrumental effects and semileptonic heavy flavor decays. The definition of this variable is as follows:

1. Each jet in the event is considered as a probe jet j_i.

2. The $\not{H}_T$ variable, $\vec{\not{H}}_{T_{\mathrm{j_i}}}$, is recalculated without considering the probe jet.
3. The azimuthal angle, $\Delta\phi_i$, is calculated with $\vec{\not{H}}_{T_{\mathrm{j_i}}}$ and the probe jet.
4. The minimum $\Delta\phi_i$, after considering all jets in the event, is defined as the $\Delta\phi^*_{\mathrm{min}}$ variable.

If a jet is mis-measured or has $\not{E}_T$ originating from the semileptonic decay of heavy flavor quarks, the direction of fake $\not{E}_T$ tends to be close to the jet axis leading to low $\Delta\phi^*_{\mathrm{min}}$ values. For SM processes with genuine $\not{E}_T$, jets recoil against neutrinos, leading to high $\Delta\phi^*_{\mathrm{min}}$ values. Furthermore, for the monojet category which has only one jet in each event with $p_{\mathrm{T}} > 40$ GeV the $\Delta\phi^*_{\mathrm{min}}$ variable cannot be defined. The variable is instead defined by considering jets with $p_{\mathrm{T}} > 25$ GeV.

As shown in Figure 5.3, the multijet background has a sharply falling distribution against $\Delta\phi^*_{\mathrm{min}}$ compared to the one with electroweak backgrounds with genuine $\not{E}_T$, which has a much longer tail.

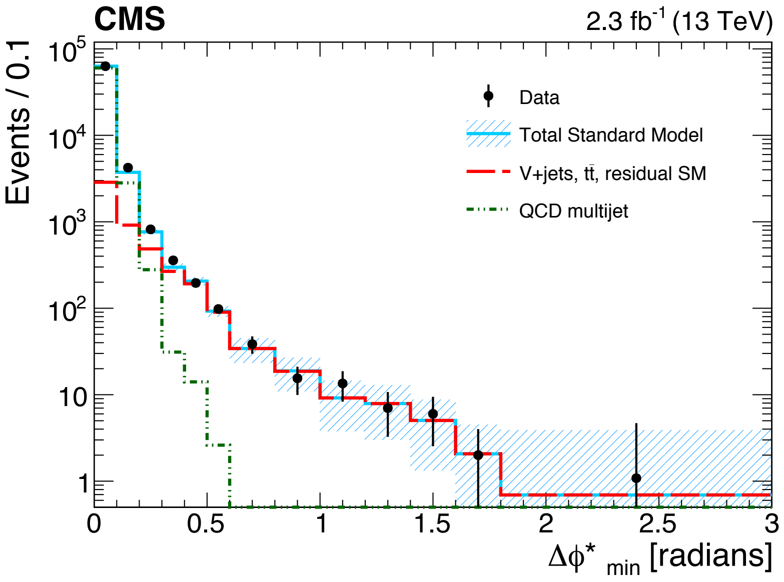

Figure 5.3.: The $\Delta\phi^*_{\mathrm{min}}$ distribution with data compared to simulation.

5.2.3. The $\not{H}_T/\not{E}_T$ variable

The $\not{H}_T/\not{E}_T$ cut aims to reduce contamination from QCD multijet backgrounds with significant fake $\not{E}_T$ due to jet just falling out of kinematic acceptances on the p_{T} (< 40 GeV) or η (< 2.4) threshold. The $\not{E}_T$ variable is computed by all PF candidates in the event, while the $\not{H}_T$ variable is computed only with jets with p_{T} and η requirements (acceptance effects) in the analysis. Therefore, the $\not{E}_T$ variable is more robust against acceptance effects. As described in Section 5.4 later, a cut of $\not{H}_T/\not{E}_T < 1.25$ in the α_T analysis is used to ensure reasonable agreement between the two kinematic variables and mitigate fake $\not{E}_T$ signatures originated from such acceptance effects.

5.2.4. Forward jet veto

The $\not{H}_T$ variable is computed using only jets with $|\eta| < 2.4$. Any jets with large p_{T} in the forward region of $|\eta| > 2.4$ can introduce significant $\not{H}_T$. Therefore, events with at least one jet with $p_{\mathrm{T}} > 40$ GeV in the forward region are vetoed and not considered in the analysis.

5.3. Trigger strategy

5.3.1. Signal region

Trigger strategies are designed to retain low thresholds on the H_T and $\not{H}_T$ variable, and maintain excellent acceptance inclusively to a wide range of new physics models. A suite of signal region triggers with requirements on H_T and α_T are used to select candidate events in HLT. Two other triggers using $\not{H}_T$, $\not{E}_T$ and H_T variables are also utilized complementarily to increase signal trigger efficiency. Table 5.1 shows the full set of signal region triggers used by the analysis.

Trigger efficiencies, as a function of H_T and $\not{H}_T$, are measured using two independent muon and electron reference triggers, for the full set of signal region triggers. Figure 5.4 and 5.5 show the measured efficiency as a function of $\not{H}_T$ for each H_T category. Nearly 100% efficiency is achieved for the lowest $\not{H}_T$ threshold of the analysis $\not{H}_T > 200$ GeV. Corrections are derived from the measurements in the reference trigger samples to account for little inefficiencies at the turn-on region. The central values of the corrections are taken from the measurement with electron reference triggers. The corresponding statistical uncertainties for the corrections, and the systematic difference to the measurement with muon reference triggers, are propagated as the uncertainties for the measurement of trigger efficiencies in signal region.

Region	Level-1 requirement	HLT requirement
Signal region	$H_T > 240$ GeV or $\not{E}_T > 70$ GeV	$H_T > 200$ GeV, $\alpha_T > 0.57$, $\not{E}_T > 90$ GeV
Signal region	$H_T > 240$ GeV or $\not{E}_T > 70$ GeV	$H_T > 250$ GeV, $\alpha_T > 0.55$, $\not{E}_T > 90$ GeV
Signal region	$H_T > 240$ GeV or $\not{E}_T > 70$ GeV	$H_T > 300$ GeV, $\alpha_T > 0.53$, $\not{E}_T > 90$ GeV
Signal region	$H_T > 240$ GeV or $\not{E}_T > 70$ GeV	$H_T > 350$ GeV, $\alpha_T > 0.52$, $\not{E}_T > 90$ GeV
Signal region	$H_T > 240$ GeV or $\not{E}_T > 70$ GeV	$H_T > 400$ GeV, $\alpha_T > 0.51$, $\not{E}_T > 90$ GeV
Signal region	$H_T > 240$ GeV	$H_T > 800$ GeV
Signal region	$\not{E}_T > 70$ GeV	$\not{E}_T > 90$ GeV or $\not{H}_T > 90$ GeV
$\mu +$jets region	${p_\mathrm{T}}^\mu > 20$ GeV	${p_\mathrm{T}}^\mu > 22$ GeV
$\mu\mu +$jets region	${p_\mathrm{T}}^\mu > 20$ GeV	${p_\mathrm{T}}^\mu > 22$ GeV

Table 5.1.: Summary of the HLT trigger paths used in the analysis.

5.3.2. $\mu +$ jets and $\mu\mu +$ jets control region

Events in $\mu +$jets and $\mu\mu +$jets control regions are selected by requiring a muon with $p_\mathrm{T} > 22$ GeV at HLT. The corresponding trigger efficiency is measured using the tag-and-probe method [57], in bins of muon p_T and η, and applied to corresponding simulated samples in the control regions.

5.4. Selection

This section details selection requirements to define signal and control regions. Section 5.4.1 defines a set of baseline selection common to all signal and controls regions. Specific selections to define signal and control regions are described in Section 5.4.2 and 5.4.3.

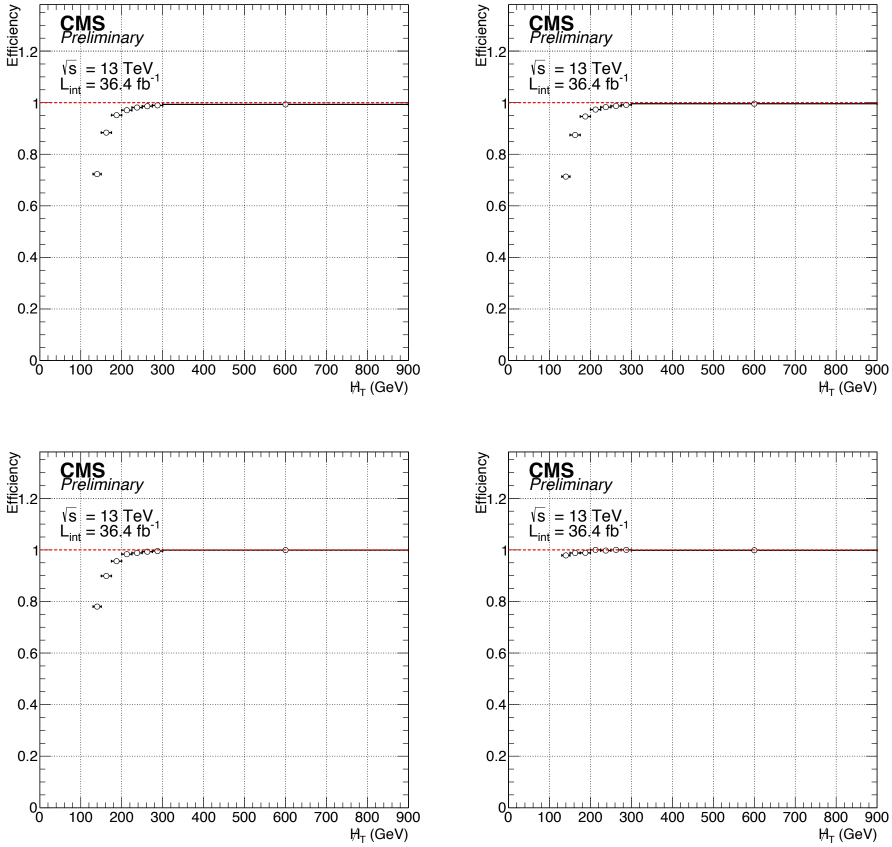

Figure 5.4.: Signal trigger efficiency in the $\not{H}_T$ dimension for each H_T category determined from data using a $e+$jets event sample.

5.4.1. Preselection

The $\not{E}_T$ variable is subject to various detector- or beam-related effects and can lead to significant fake $\not{E}_T$, for example, beam halos, spurious detector noise, detector inefficiencies, and reconstruction failures. Dedicated filters are employed to reject these events with $> 99\%$ efficiency. These filters include:

- Primary vertex filter: requires at least one well reconstructed vertex.
- CSC beam halo filter: rejects events with beam halo muons by measured by CSC.
- HBHE Noise and isolation filter: rejects events with spontaneous energy spikes in HCAL.

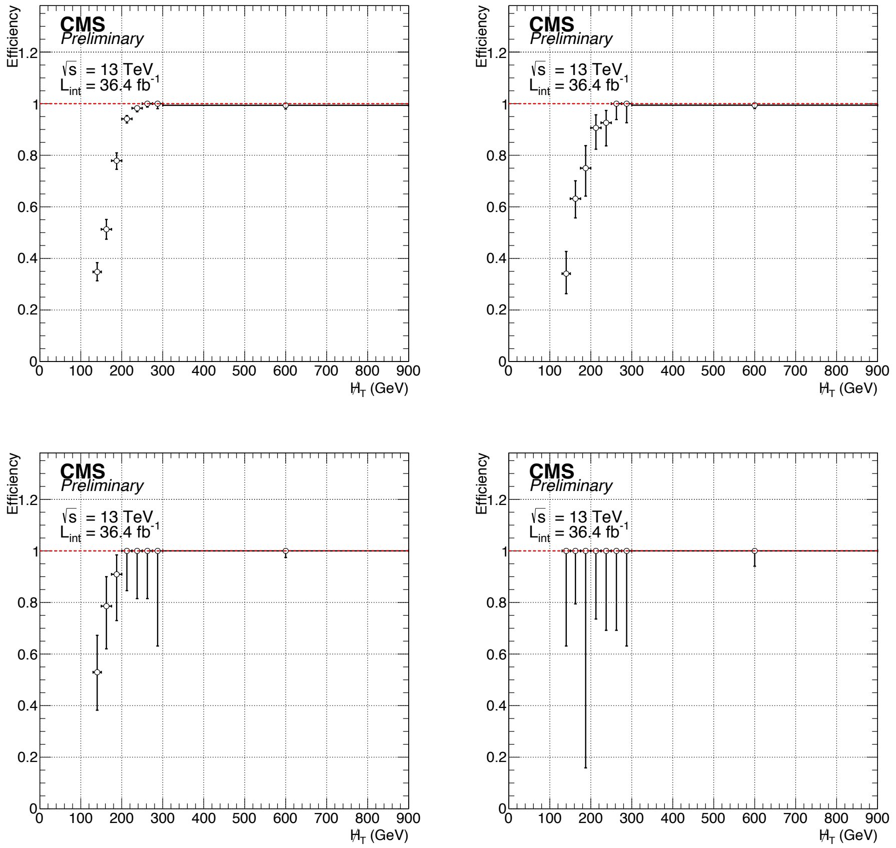

Figure 5.5.: Signal trigger efficiency in the $\not{H}_T$ dimension for each H_T category determined from data using a $\mu + $jets event sample.

- ECAL Endcap supercluster Noise filter: rejects events with spontaneous pulses in ECAL Endcap.
- ECAL trigger primitive filter: rejects events with significant energy deposits in dead cell regions.
- bad muon and charged hadron filters: rejects events with badly reconstructed muon and charged hadron by the PF algorithm.

In addition, the α_T analysis also employs specific cleaning cuts to further reject events with misreconstruction and beam halos. The charged hadron energy fraction (CHF) of the leading jet in each event is required to be $0.1 < \text{CHF} < 0.95$, to further reject events affected by beam halos but not filtered by the CSC beam halo filter.

Jets in the analysis are required to have $p_{\mathrm{T}} > 40$ GeV and $|\eta| < 2.4$. The leading jet in the event is required to satisfy $p_{\mathrm{T}} > 100$ GeV. The energy scale of each event is estimated with the H_T variable. The estimator for $\not{E}_T$ used by this search is given by the $\not{H}_T$ variable. Significant hadronic activity and large $\not{E}_T$ in the event is ensured by requiring $H_T > 200$ GeV and $\not{H}_T > 200$ GeV, respectively.

As described in Section 5.2.3 and 5.2.4, a $\not{H}_T / \not{E}_T$ cut and forward jet veto are applied as preselection to mitigate effects due to acceptance from p_{T} and η threshold or forward regions.

All preselection requirements are summarized in Table 5.2.

$\not{E}_T$ quality	Primary Vertex, CSC Beam Halo, HBHE Noise and Isolation, ECAL Endcap SC Noise, ECAL TP, Bad Muon, Bad Charged Hadron
Beam halo	$0.1 < \mathrm{CHF} < 0.95$ for highest-p_{T} jet
Jet j_i acceptance	Each jet j_i that satisfies ${p_{\mathrm{T}}}^{\mathrm{j}_i} > 40$ GeV and $\mid \eta^{\mathrm{j}_1} \mid < 2.4$
Jet j_1 acceptance	${p_{\mathrm{T}}}^{\mathrm{j}_1} > 100$ GeV
Jets below threshold	$\not{H}_T / \not{E}_T < 1.25$
Forward jet veto	Veto events containing a jet satisfying $p_{\mathrm{T}} > 40$ GeV and $\mid \eta \mid > 2.4$
Energy sums	$H_T > 200$ GeV and $\not{H}_T > 200$ GeV

Table 5.2.: Summary of the pre-selection criteria.

5.4.2. Signal region

The signal region selection is designed to strongly suppress QCD background, which is often difficult to model because it arises from stochastic fluctuations, and electroweak background, while maintaining good acceptance to a wide range of SUSY models with significant $\not{E}_T$.

To select hadronic signal region, any events with at least one isolated muon, photon or electron, as described in Section 4.2, are vetoed. Furthermore, events containing at least one isolated track with $p_{\mathrm{T}} > 10$ GeV are also vetoed to suppress background processes with final states containing non-reconstructed muons or electrons, or τ leptons with single-prong decays.

As described in Section 5.2.1 to 5.2.4, three dedicated variables and one veto are used to reject QCD backgrounds. In particular, as the $\not{H}_T$ and H_T variable are correlated via the α_T variable as shown in equation 5.6, a H_T dependent α_T threshold is chosen to maintain a similar $\not{H}_T$ threshold due to changing H_T requirements. These thresholds are also motivated by the trigger requirements as explained in Section 5.3. The α_T thresholds are summarized in Table 5.3. No α_T cut is applied for $H_T > 900$ GeV. At least two jets in an event are required to define the α_T variable, therefore, the α_T thresholds are not applicable to the events containing only one jet, the monojet category. Categorizations of events are detailed in Section 5.5.

As shown also in Table 5.3, a flat requirement of $\Delta\phi^*_{\text{min}} > 0.5$ is applied to all events. For events in the monojet category, the $\Delta\phi^*_{\text{min}}$ variable is computed with all jets with $p_{\text{T}} > 25$ GeV.

H_T [GeV]	200–250	250–300	300–350	350–400	400–900	900–1200	>1200
α_T threshold	0.65	0.60	0.55	0.53	0.52	(none)	(none)
$\Delta\phi^*_{\text{min}}$ threshold	0.5	0.5	0.5	0.5	0.5	0.5	0.5

Table 5.3.: Minimum requirements on α_T for each H_T bin. For all H_T bins satisfying $H_T >$ 900 GeV, no α_T cut is applied. Also shown is the flat $\Delta\phi^*_{\text{min}}$ requirement.

5.4.3. Control regions

The $\mu +$ jets control region, $\mu\mu +$ jets control region and multijet control region are utilized in the α_T analysis. These three control regions are used to predict QCD and electroweak backgrounds in the signal region, and validate various assumptions on analysis methods and strategies. Their selections are orthogonal to the signal region selections and designed to have negligible signal contamination from hadronic SUSY models. Table 5.4 summarizes each of the selections for these three control regions. Section 5.4.3 to 5.4.3.1 explain selections of each control region respectively.

$\mu +$ jets control region

The selection for the $\mu +$ jets control region is designed to enhance the SM processes with W bosons decaying to a muon and a neutrino, such as W + jets and $\text{t}\bar{\text{t}}$ + jets

$\mu + \text{jets}$	1μ with $p_{\mathrm{T}} > 30$ GeV, $\mid \eta \mid < 2.1$, $I^{\mu}_{\mathrm{rel}} < 0.1$, $\Delta R(\mu, \mathrm{j}_i) > 0.5$, $30 < m_{\mathrm{T}}(\vec{p}^{\,\mu}_{\mathrm{T}}, \not{E}_T) < 125$ GeV
$\mu\mu + \text{jets}$	2μ with $p_{\mathrm{T}} > 30$ GeV, $\mid \eta \mid < 2.1$, $I^{\mu}_{\mathrm{rel}} < 0.1$, $\Delta R(\mu_{1,2}, \mathrm{j}_i) > 0.5$, $\mid m_{\mu\mu} - m_{\mathrm{Z}} \mid < 25$ GeV
Multijet	SR selection + inverted $\not{H}_T / \not{E}_T$ and $\Delta\phi^{*}_{\mathrm{min}}$ requirements

Table 5.4.: Summary of the event selection criteria for the control regions.

production, with a W boson from a top quark decaying to a muon and a neutrino in final state. Events with exactly one isolated, central and high-p_{T} muon are selected, on top of the preselection described in Section 5.4.1. The muon is required to have $p_{\mathrm{T}} > 30$ GeV and $|\eta| < 2.1$ and to be well separated from each jet $\mathrm{j_i}$ by $\Delta R(\mu, \mathrm{j}_i) > 0.5$. In addition, the transverse mass computed by the muon p_{T} and $\not{E}_T$ is required to satisfy $30 < m_{\mathrm{T}}(\mu, \not{E}_T) < 125$ GeV to ensure the control region enriched in W bosons.

$\mu\mu +$ jets control region

The $\mu\mu + \text{jets}$ control sample is designed to be enriched in $\mathrm{Z}(\rightarrow \mu\mu) + \text{jets}$ production. The selections are similar to ones used for the $\mu + \text{jets}$ control region, except that two oppositely charged isolated muons are required. The two muons are also required to have an invariant mass of within ± 25 GeV range around the mass of the Z boson.

5.4.3.1. Multijet control region

The multijet control region is used to estimate the residual QCD background in the signal region. It is defined by the exact same requirement as the signal region except the $\Delta\phi^{*}_{\mathrm{min}}$ and $\not{H}_T / \not{E}_T$ requirement are inverted. The selection aims to give a data sample enriched in QCD processes.

5.5. Categorization

5.5.1. Categorization in signal region

To maintain a broad coverage to a wide range of hadronic SUSY signal models, events in the signal region are categorized in four discriminating variables: N_{jet}, N_b, H_T and $\not{H}_T$. This extensive categorization ensures good sensitivities to a wide range of SUSY models, which can be characterized efficiently by the four kinematic variables chosen. For example, the N_{jet} and H_T categories can discriminate between SUSY models with different mass splitting scenarios. The N_b categories can improve signal-to-background separation of SUSY models with heavy flavor squarks. The $\not{H}_T$ dimension provides further categorization between uncompressed, intermediate and compressed SUSY models on top of the N_{jet}, N_b and H_T binning. Detail of binning choices are detailed in the following subsections.

Categorization in N_{jet} and topology

Seven N_{jet} categories are defined as shown in Table 5.5. The symmetric category is further split into $N_{jet} = 2,\ 3,\ 4,\ 5$ or ≥ 6 category. Different SUSY models reside in vastly different N_{jet} categories. Light flavor squark and compressed models tend to have low jet multiplicity with large energy, while uncompressed models of gluino or top squark production have larger jet multiplicities. SM backgrounds also varies vastly across N_{jet} categories, with $\mathrm{W} + \mathrm{jets}$ and $\mathrm{Z} + \mathrm{jets}$ populating low N_{jet} categories and $\mathrm{t\bar{t}} + \mathrm{jets}$ in high N_{jet} categories.

Events are also often conveniently categorized according to the “topology” exhibited by the two leading jets in the event. The topology is defined by the p_{T} of the subleading jet in the event, as summarized in Table 5.6. Events with subleading jet j_2 that satisfies ${p_{\mathrm{T}}}_{ji2} > 100$ GeV are classified as the “symmetric” topology. This topology is sensitive to a wide range of SUSY models involving pair production of gluinos or squarks. Events with subleading jet j_2 that satisfies ${p_{\mathrm{T}}}_{ji2} < 40$ GeV are classified as the “monojet” topology, and if the subleading jet satisfies $40 < {p_{\mathrm{T}}}_{ji2} < 100$ GeV the corresponding event is classified as the “asymmetric” topology. The addition of monojet and asymmetric category improve acceptance to DM and compressed SUSY models.

N_{jet}	Topology	Label
1	Monojet	eq1j
$\geq$2	Asymmetric	ge2a
2	Symmetric	eq2j
3	Symmetric	eq3j
4	Symmetric	eq4j
5	Symmetric	eq5j
$\geq$6	Symmetric	ge6j

Table 5.5.: Summary of N_{jet} categorization.

Monojet	${p_T}^{j2} < 40$ GeV
Asymmetric	$40 < {p_T}^{j2} < 100$ GeV
Symmetric	${p_T}^{j2} > 100$ GeV

Table 5.6.: Summary of topologies, based on p_T requirement for the subleading jet.

Categorization in H_T

The H_T variable provides an estimate of the energy scale of events. For SUSY models, H_T is correlated with the mass splitting between the sparticle produced and the LSP. If the sparticle produced is heavy and the LSP is light, decay products from sparticles will have a lot of energy and leads to a high H_T value. On the other hand if the mass of the sparticle and LSP is close, limited energy will be delivered to the decay products, leading to a small H_T value. Five H_T categories are defined for the signal region. The lowest H_T threshold is 200 GeV from preselection requirements, while the last bin is an inclusive bin $H_T > 1200$ GeV.

- 200–400 GeV,
- 400–600 GeV,
- 600–900 GeV,

- 900–1200 GeV,
- >1200 GeV.

On the other hand, a finer H_T scheme is defined for the muon control regions, from where predictions are derived for different backgrounds, as described in Section 5.5.2 and 5.5.3. Background predictions from control regions are aggregated to give predictions in signal regions. This aggregation is implemented in the likelihood model and assumptions on correlation between each category and systematic uncertainty are preserved [74]. Table 5.7 shows the aggregation scheme of the prediction derived from muon control regions to the signal region. The Likelihood is described in detail in Section 9.

Control regions	Signal region
200–250	200–400
250–300	200–400
300–350	200–400
350–400	200–400
400–500	400–600
500–600	400–600
600–750	600–900
750–900	600–900
900–1050	900–1200
1050–1200	900–1200
>1200	>1200

Table 5.7.: Summary of the H_T [GeV] binning schemes used in the control and signal region.

Categorization in N_b

A categorization in N_b improves sensitivities to SUSY models involving heavy-flavor squarks, which can typically produce two to four bottom quarks in final states. Events are categorized in five categories as shown in Table 5.8.

N_b	Label
0	eq0b
1	eq1b
2	eq2b
3	eq3b
$\geq$4	ge4b

Table 5.8.: Summary of N_b categorization.

Categorization in $\not{H}_T$

Significant $\not{H}_T$ can be present in events if a large portion of energy is carried away by neutrinos or LSPs in SUSY models. By categorizing in both the H_T and $\not{H}_T$ variable, good sensitivities to uncompressed, intermediate and compressed SUSY models are maintained. The $\not{H}_T$ dimension is at most divided into four bins with boundaries at 200–400, 400–600, 600–900, and ≥900 GeV. As such, the $\not{H}_T$ binning scheme aligns with the H_T bin boundary. This binning scheme is then modified according to available statistics in the simulation samples. In particular, at least 500 unweighed events are required in each (N_{jet}, H_T, $\not{H}_T$) bin, inclusive with respect to N_b. Adjacent $\not{H}_T$ bins are merged until this requirement is satisfied.

Summary of signal region categorization

Table 5.9 shows the $\not{H}_T$ binning scheme as a function of N_{jet}, N_b, and H_T in the α_T analysis. The total number of (N_{jet}, H_T, N_b, $\not{H}_T$) categories in the signal region is 276.

5.5.2. Categorization in $\mu +$ jets control region

Categorizations of control regions mimic closely the one in the signal region, to mitigate any systematic effects when deriving predictions. For the $\mu +$ jets control region, events are categorized in N_{jet}, N_b and H_T, and there is no categorization in the $\not{H}_T$ dimension. In particular, the categorizations in N_{jet} and N_b are identical to those in the signal region. A finer H_T scheme, with in total eleven categories, is

N_{jet}	N_b	H_T [GeV]			
		400	600	900	1200
$\geq 2a$	0	200, >400	200, 400, >600	200, >900	–
$\geq 2a$	1	200, >400	200, 400, >600	200, >900	–
$\geq 2a$	2	200, >400	200, 400, >600	200, >900	–
$\geq 2a$	3	200, >400	200, 400, >600	–	–
2	0	200, >400	200, 400, >600	200, 400, 600, >900	200, 400, 600, >900
2	1	200, >400	200, 400, >600	200, 400, 600, >900	200, 400, 600, >900
2	2	200, >400	200, 400, >600	200, 400, 600, >900	
3	0	200, >400	200, 400, >600	200, 400, 600, >900	200, 400, 600, >900
3	1	200, >400	200, 400, >600	200, 400, 600, >900	200, 400, 600, >900
3	2	200, >400	200, 400, >600	200, 400, 600, >900	200, 400, 600, >900
3	3	200, >400	200, 400, >600	200, 400, 600, >900	
4	0	200, >400	200, 400, >600	200, 400, 600, >900	200, 400, 600, >900
4	1	200, >400	200, 400, >600	200, 400, 600, >900	200, 400, 600, >900
4	2	200, >400	200, 400, >600	200, 400, 600, >900	200, 400, 600, >900
4	3	200, >400	200, 400, >600	200, 400, 600, >900	–
5	0	200, >400	200, 400, >600	200, 400, 600, >900	200, 400, 600, >900
5	1	200, >400	200, 400, >600	200, 400, 600, >900	200, 400, 600, >900
5	2	200, >400	200, 400, >600	200, 400, 600, >900	200, 400, 600, >900
5	3	200, >400	200, 400, >600	200, 400, 600, >900	–
5	≥ 4	200, >400	–	–	–
≥ 6	0	200, >400	200, 400, >600	200, 400, >600	200, 400, 600, >900
≥ 6	1	200, >400	200, 400, >600	200, 400, >600	200, 400, 600, >900
≥ 6	2	200, >400	200, 400, >600	200, 400, >600	200, 400, 600, >900
≥ 6	3	200, >400	200, 400, >600	200, 400, >600	200, 400, 600, >900
≥ 6	≥ 4	200, >400	–	–	–

Table 5.9.: Summary of the $\not{H}_T$ binning scheme as a function of N_{jet}, N_b, and H_T [GeV] in the signal region.

defined to ensure the finest control of background prediction. All eleven categories are shown in Table 5.7. The last H_T bin in each (N_{jet},N_b) category is required to have at least one data count in $\mu +$ jets control region to allow a meaningful prediction. The total number of categories in the $\mu +$ jets control sample is 204.

5.5.3. Categorization in $\mu\mu +$ jets control region

Similar to the $\mu +$ jets control sample, events in the $\mu\mu +$ jets control region are categorized also in N_{jet}, N_b and H_T. However, due to lack of data statistics in this control region for $N_b \geq 2$, only two N_b categories are employed: $N_b = 0$ and $N_b \geq 1$. The total number of categories in the $\mu\mu +$ jets control sample is 121.

5.5.4. Categorization in multijet control region

Events in multijet control region are categorized in (N_{jet},H_T), identically as in the signal region. This control region is used to predict the QCD background in signal region.

Chapter 6.

Data and simulated samples

The analysis uses data collected in 2016 by the CMS detector during the 25 ns run of the LHC at $\sqrt{s} = 13$ TeV, and simulated samples for background and signal contributions which are produced for this p-p collision run in 2016.

6.1. Data

Data events recorded by the CMS detector are collected with various trigger selections described in Section 5.3, which includes α_T-H_T,$\slashed{H}_T$-$\slashed{E}_T$ and H_T triggers for the signal region, and single muon triggers for muon control regions. Figure 6.1 shows the integrated luminosity delivered by LHC and collected by CMS against time in 2016. Only data with good quality are used in the analysis and the dataset corresponds to an integrated luminosity of 35.9 ± 0.9 fb^{-1} [75].

6.2. Simulated samples

The dominant backgrounds, $\mathrm{Z}(\rightarrow \nu\bar{\nu}) +$ jets, $\mathrm{Z}(\rightarrow \ell\ell) +$ jets, $\mathrm{t\bar{t}} +$ jets, $\mathrm{W} +$ jets and QCD multijet samples are generated with Madgraph5_aMCATNLO 2.2.2 [77] at leading order (LO), and s-channel production of single top and $\mathrm{t\bar{t}V}$ events are generated with the same generator at next-to-leading order (NLO) in the strong coupling constant α_s. Single top samples in t-channel and tW-channel are generated

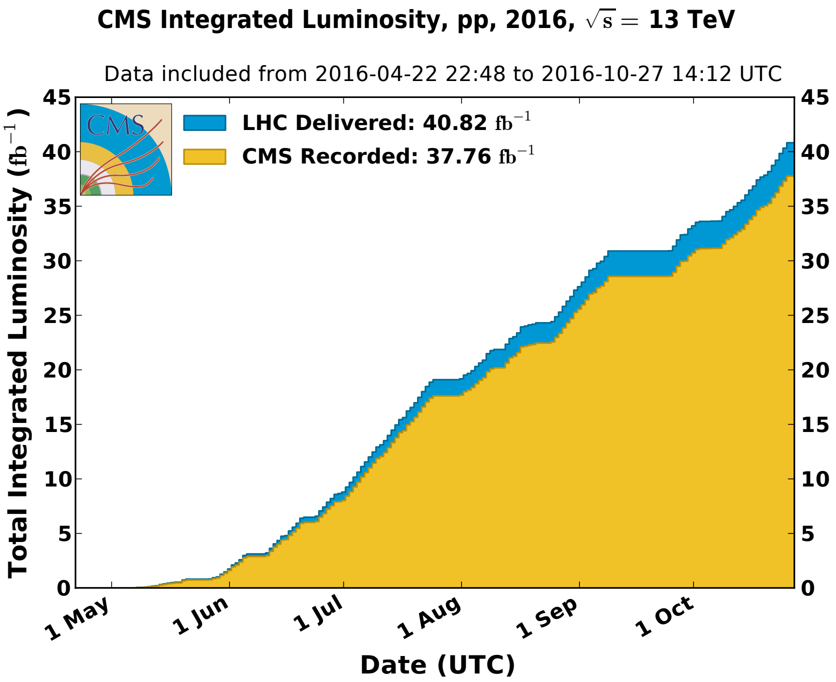

Figure 6.1.: Integrated luminosity delivered by LHC and collected by CMS against time. From [76].

by NLO POWHEG v2 [78,79], while diboson samples are generated by PYTHIA 8.205 [80].

NNPDF 3.0 LO and NLO [81] parton distribution functions (PDFs) are used with the corresponding LO and NLO generators as described above.

Full detector response of the CMS detector is simulated using the GEANT4 package [82]. Inclusive simulated event samples are normalized to inclusive cross sections calculated in NNLO precision. Table B.1-B.2 shows a list of inclusive cross sections for reweighting simulated samples.

6.3. Corrections to simulated samples

6.3.1. Pileup reweighting

The distribution of the number of pileup (PU) interactions in MC is different from that in data, which varies over time. This difference between MC and data is corrected with the pileup reweighting factors. These factors are the ratios of the distribution of the number of interactions in data and MC. The distribution for data is derived by measuring the instantaneous luminosity of colliding bunches and multiplying by the total inelastic proton-proton cross section. Figure 6.2 shows the distribution of the mean number of interactions per crossings.

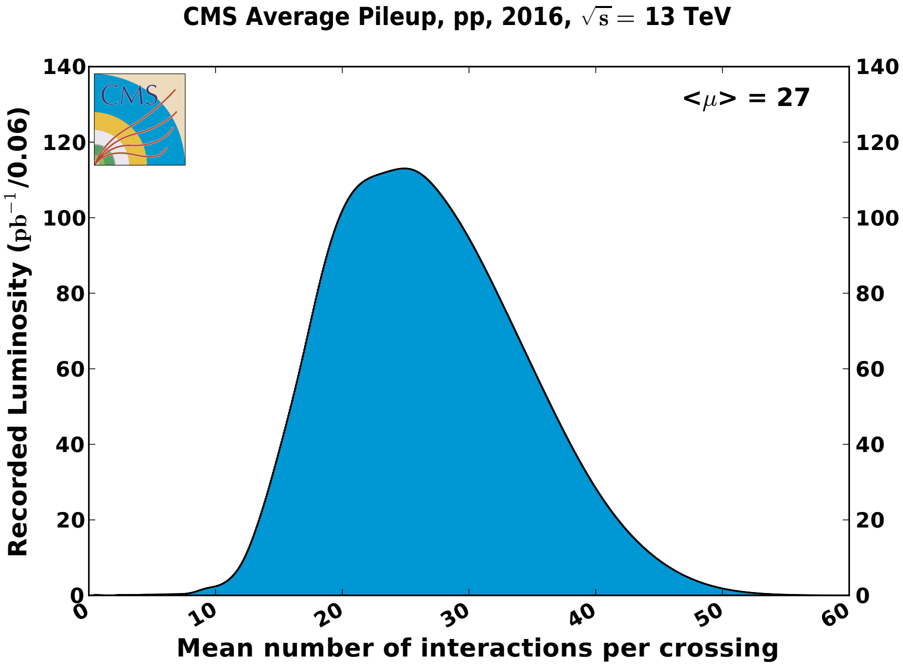

Figure 6.2.: Mean number of interactions per bunch crossing for the 2016 proton-proton run at 13 TeV. The cross section is taken to be 80 mb. From [76].

6.3.2. W, Z and γ boson p_{T}-dependent higher order correction

MC samples for leading backgrounds in the analysis are simulated at leading order in α_s accuracy. Missing higher order corrections can result in distortions in W, Z and γ boson p_{T} spectra. Theoretical corrections [83] are applied to account for this effect, and a 100% uncertainty is assumed for these corrections.

6.3.3. Initial state radiation (ISR)

To improve modeling on the multiplicity of additional jets from ISR and associated jet production for $\mathrm{t\bar{t}} + \mathrm{jets}$ process, reweighting factors are derived in $\mathrm{t\bar{t}} + \mathrm{jets}$ samples with dileptonic decay, as a function of the number of additional jets from ISR [84]. These reweighting factors are applied in the N_{jet} distribution of $\mathrm{t\bar{t}}$ in the analysis.

6.3.4. Lepton and photon efficiency

Selection efficiencies for leptons and photons are different in MC and data. Such discrepancy typically arises from mis-modeling in object identification, reconstruction or trigger selection. Such differences are mitigated by scale factors, which are ratios of the selection efficiency measured in data samples, such as $\mathrm{Z} \to \ell\ell$, using the tag-and-probe method [85], to that predicted in MC, and are binned with the properties of physics object, such as p_{T}, η.

6.3.5. B-tagging efficiency

Similar to lepton and photon scale factors in Section 6.3.4, the difference in b-tagging efficiencies between data and MC is corrected with b-tag scale factors. The scale factors are derived in jet p_{T}, η and flavor (bottom jet, charm jet and light jet) in three different data samples described in Table 4.1. The scale factors are used to correct simulation samples in event-by-event basis. For each event, the probability of a given b-tagging configuration in simulation and data is given by

$$P_{\mathrm{MC}} = \prod_{i=\mathrm{tagged}} \epsilon_i \prod_{j=\mathrm{nottagged}} (1 - \epsilon_j) \tag{6.1}$$

and

$$P_{\mathrm{Data}} = \prod_{i=\mathrm{tagged}} \epsilon_i \times \mathrm{SF}_i \prod_{j=\mathrm{nottagged}} (1 - \epsilon_j \times \mathrm{SF}_j) \tag{6.2}$$

where ϵ_i and SF_i are the corresponding b-tagging efficiency calculated in simulation and scale factor for jet i with $p_{\mathrm{T}i}$, η_i and flavor i. The product sum runs over all jets in the event. Consequently, the event is reweighed by a factor

$$w = \frac{P_{\mathrm{Data}}}{P_{\mathrm{MC}}} \tag{6.3}$$

6.3.6. Trigger efficiency

Trigger efficiency in data for signal and each control regions are measured, as described in Section 5.3, and differences to that emulated in MC are corrected.

6.3.7. Sideband correction

The normalization of simulated samples may have discrepancies to that observed in data, due to mis-modeling of kinematic variables or missing higher order corrections in inclusive cross sections for various SM processes. Process-dependent corrections, called sideband corrections, are determined with maximum likelihood fit to data in sidebands and applied to simulated samples.

Specifically, a simultaneous fit in the sideband 150 GeV $< \not{H}_T <$ 200 GeV of the $\mu +$ jets and $\mu\mu +$ jets control region is used to derive correction factors for $\mathrm{W} +$ jets, $\mathrm{t\bar{t}} +$ jets and $\mathrm{Z} +$ jets normalizations. Table 6.1 shows the values of the correction factors for each of the processes involved.

Process	**Sideband**	**Selection**	**Correction**
$\mathrm{W}+\text{jets}$	$150 < \not{H}_T < 200\,\text{GeV}$	$\mu+\text{jets}$	1.06
$\mathrm{Z}+\text{jets}$	$150 < \not{H}_T < 200\,\text{GeV}$	$\mu\mu+\text{jets}$	0.91
$\mathrm{t\bar{t}}+\text{jets}$	$150 < \not{H}_T < 200\,\text{GeV}$	$\mu+\text{jets}$, $\mu\mu+\text{jets}$	0.93

Table 6.1.: Cross section corrections for SM backgrounds derived with fit to sidebands in data.

Chapter 7.

B-tag formula method

7.1. Introduction

The fine binning in N_b as described in Section 5.5 leads to loss in MC statistics, due to explicit cuts on b-tagging discriminators as described in Section 4. A method called the “formula method” is used to increase the statistical power from simulations for bins with high b-jet multiplicities, $N_b \geq 2$. The idea of the method is to calculate the N_b distribution for each (N_{jet},H_T,$\not{H}_T$) category with generator-level information, b-tag and mis-tag efficiencies, utilizing the full available MC statistics.

The b-tagging algorithm, as described in Section 4, has non-unity b-tag efficiency and non-zero mis-tag probabilities. The algorithm can identify correctly a jet coming from a b-quark (b) as a b-jet, or mis-identify jets coming from a charm quark (c) or light-flavored (LF) quark, i.e. u, d, s quarks or gluons, as a b-jet.

For each (N_{jet},H_T,$\not{H}_T$) category, the following procedures are used to calculate the N_b distribution:

- Step 1: derive the b-tag efficiency ϵ_{b}, mis-tag efficiencies for c-jet ϵ_{c} and light jets ϵ_{LF} with simulated samples for backgrounds, averaging over jet p_{T} and η. Corrections are applied on a jet-by-jet basis to each efficiency derived from simulation (ϵ_{b}, ϵ_{c} and ϵ_{LF}) in order to match the corresponding measurements from data, as described in Section 4.

- Step 2: categorize MC events with the number of true b-jets, c-jets and light-jets according to generator level information, $N\left(n_{\mathrm{b}}^{\mathrm{gen}}, n_{\mathrm{c}}^{\mathrm{gen}}, n_{\mathrm{c}}^{\mathrm{gen}}\right)$.
- Step 3: For each categorization $N\left(n_{\mathrm{b}}^{\mathrm{gen}}, n_{\mathrm{c}}^{\mathrm{gen}}, n_{\mathrm{c}}^{\mathrm{gen}}\right)$ in step 2, the probability of having $n^{\mathrm{tag}} = n_{\mathrm{b}}^{\mathrm{tag}} + n_{\mathrm{c}}^{\mathrm{tag}} + n_{\mathrm{LF}}^{\mathrm{tag}}$ b-tagged jets is given by

  $$\begin{aligned} P\left(n^{\mathrm{tag}} | n_{\mathrm{b}}^{\mathrm{gen}}, n_{\mathrm{c}}^{\mathrm{gen}}, n_{\mathrm{LF}}^{\mathrm{gen}}\right) = P_{\mathrm{bino}}\left(n_{\mathrm{b}}^{\mathrm{tag}} | n_{\mathrm{b}}^{\mathrm{gen}}\right) \times P_{\mathrm{bino}}\left(n_{\mathrm{c}}^{\mathrm{tag}} | n_{\mathrm{c}}^{\mathrm{gen}}\right) \times \\ P_{\mathrm{bino}}\left(n_{\mathrm{LF}}^{\mathrm{tag}} | n_{\mathrm{LF}}^{\mathrm{gen}}\right) \end{aligned} \tag{7.1}$$

  where $P_{\mathrm{bino}}(k|n\epsilon) = \frac{n!}{k!(n-k)!}\epsilon^k(1-\epsilon)^{n-k}$ is the binomial distribution, with the number of trials n as $n_{\mathrm{i}}^{\mathrm{gen}}$, the number of success trials k as $n_{\mathrm{i}}^{\mathrm{tag}}$ and the success probability ϵ as ϵ_{i}, where i can be b, c or LF. Each categorization $N\left(n_{\mathrm{b}}^{\mathrm{gen}}, n_{\mathrm{c}}^{\mathrm{gen}}, n_{\mathrm{c}}^{\mathrm{gen}}\right)$ can contribute to a $N_b = n^{\mathrm{tag}}$ bin, weighted by $P\left(n^{\mathrm{tag}} | n^{\mathrm{gen}}\right)$. The total contribution to this bin with $N_b = n^{\mathrm{tag}}$ is computed by considering all categorizations $N\left(n_{\mathrm{b}}^{\mathrm{gen}}, n_{\mathrm{c}}^{\mathrm{gen}}, n_{\mathrm{c}}^{\mathrm{gen}}\right)$,

  $$\begin{aligned} N(n^{\mathrm{tag}}) = \sum_{n_{\mathrm{b}}^{\mathrm{gen}}, n_{\mathrm{c}}^{\mathrm{gen}}, n_{\mathrm{LF}}^{\mathrm{gen}}} & \left[N\left(n_{\mathrm{b}}^{\mathrm{gen}}, n_{\mathrm{c}}^{\mathrm{gen}}, n_{\mathrm{LF}}^{\mathrm{gen}}\right) \times \right. \\ \sum_{n^{\mathrm{tag}} = n_{\mathrm{b}}^{\mathrm{tag}} + n_{\mathrm{c}}^{\mathrm{tag}} + n_{\mathrm{LF}}^{\mathrm{tag}}} & \left. P\left(n_{\mathrm{b}}^{\mathrm{tag}}, n_{\mathrm{c}}^{\mathrm{tag}}, n_{\mathrm{LF}}^{\mathrm{tag}} | n_{\mathrm{b}}^{\mathrm{gen}}, n_{\mathrm{c}}^{\mathrm{gen}}, n_{\mathrm{LF}}^{\mathrm{gen}}\right)\right] \end{aligned} \tag{7.2}$$

As a simple example, consider a bin with 2 reconstructed jets, in which 1000 events contain 2 light-flavored jets, i.e. $(n_{\mathrm{b}}^{\mathrm{gen}} = 0, n_{\mathrm{c}}^{\mathrm{gen}} = 0, n_{\mathrm{LF}}^{\mathrm{gen}} = 2)$ and 500 events contain 1 light-flavored jet and 1 b-jet, i.e. $(n_{\mathrm{b}}^{\mathrm{gen}} = 1, n_{\mathrm{c}}^{\mathrm{gen}} = 0, n_{\mathrm{LF}}^{\mathrm{gen}} = 1)$, and a b-tag efficiency $\epsilon_{\mathrm{b}} = 0.65$ and a light-flavor (mis-tag) efficiency $\epsilon_{\mathrm{LF}} = 0.01$. The

N_b distribution is then calculated as follows:

$$\begin{aligned}
N(0) &= 1000 \times (1-\epsilon_{\mathrm{LF}})^2 + \\
&\quad 500 \times (1-\epsilon_{\mathrm{b}}) \times (1-\epsilon_{\mathrm{LF}}) \\
&= 1153.35 \\
N(1) &= 1000 \times (1-\epsilon_{\mathrm{LF}}) \times \epsilon_{\mathrm{LF}} \times 2 + \\
&\quad 500 \times (1-\epsilon_{\mathrm{b}}) \times \epsilon_{\mathrm{LF}} \ + \ 500 \times \epsilon_{\mathrm{b}} \times (1-\epsilon_{\mathrm{LF}}) \\
&= \ 343.3 \\
N(2) &= \ 500 \times \epsilon_{\mathrm{b}} \times \epsilon_{\mathrm{LF}} + \\
&1000 \times \epsilon_{\mathrm{LF}}^2 \\
&= \quad 3.35
\end{aligned}$$

The method provides a more reliable estimation with much less statistical fluctuations for categories with $N_b \geq 2$, since full statistical power for each (N_{jet}, H_T, $\not{H}_T$) category is utilized.

7.2. Systematic uncertainty

The formula method introduces correlations between different N_b bins in each (N_{jet},H_T,$\not{H}_T$) category. The correlations are accounted for by generating toys by randomization of inputs for the method, $N\left(n_{\mathrm{b}}^{\mathrm{gen}}, n_{\mathrm{c}}^{\mathrm{gen}}, n_{\mathrm{c}}^{\mathrm{gen}}\right)$, ϵ_{b}, ϵ_{c}, ϵ_{LF}, and calculating N_b distribution for each toy. Each category in $N\left(n_{\mathrm{b}}^{\mathrm{gen}}, n_{\mathrm{c}}^{\mathrm{gen}}, n_{\mathrm{c}}^{\mathrm{gen}}\right)$ is randomized by a random variable from a Poisson distribution $P_{\mathrm{pois}}(x|\lambda)$, where λ is the mean of the distribution taken as the prediction in the corresponding category. Each b-tagging and mis-tagging efficiency (ϵ_{b}, ϵ_{c}, ϵ_{LF}) is randomized separately by a Gaussian distribution $P_{\mathrm{gaus}}(\epsilon|\epsilon_0, \sigma)$, where ϵ_0 and σ are the mean and standard deviation of the Gaussian distribution respectively. An ensemble with one thousand toys is generated and the N_b distribution is calculated for each toy with the method. The corresponding covariance and correlation matrix are calculated with the ensemble of N_b distributions. The covariance matrix is diagonalized and the corresponding eigenvectors are used to form templates for systematic uncertainties. Figure 7.1-7.2

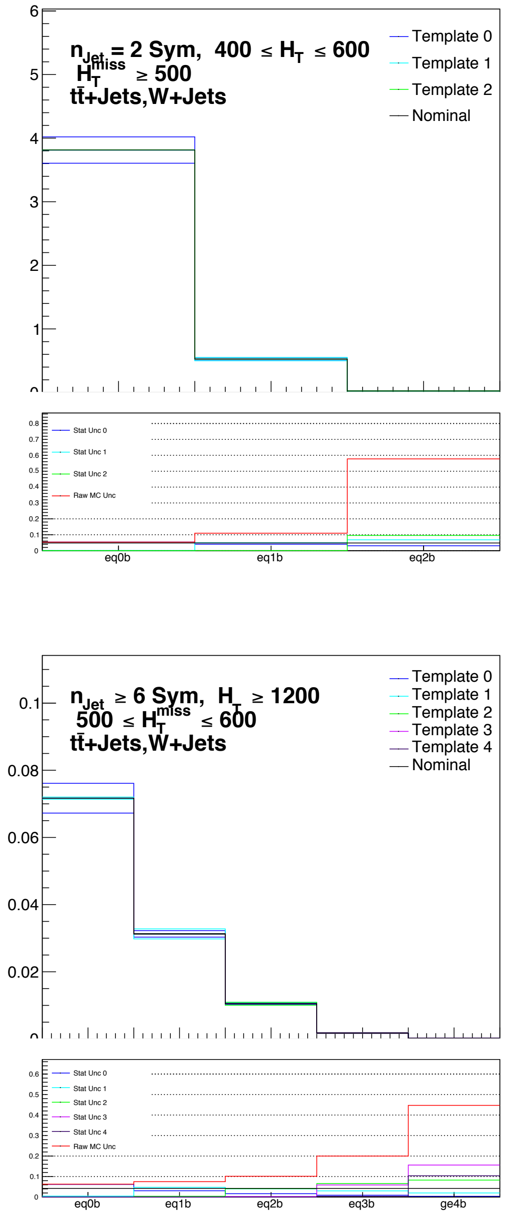

Figure 7.1.: Systematic templates from toys for W + jets and $t\bar{t}$ + jets. The red line represents statistical uncertainty of direct b-tagging for comparison.

show systematic templates from the eigenvectors. It is observed that the method reduces statistical uncertainties for categories with $N_b \geq 2$ by a factor of 2 to 4.

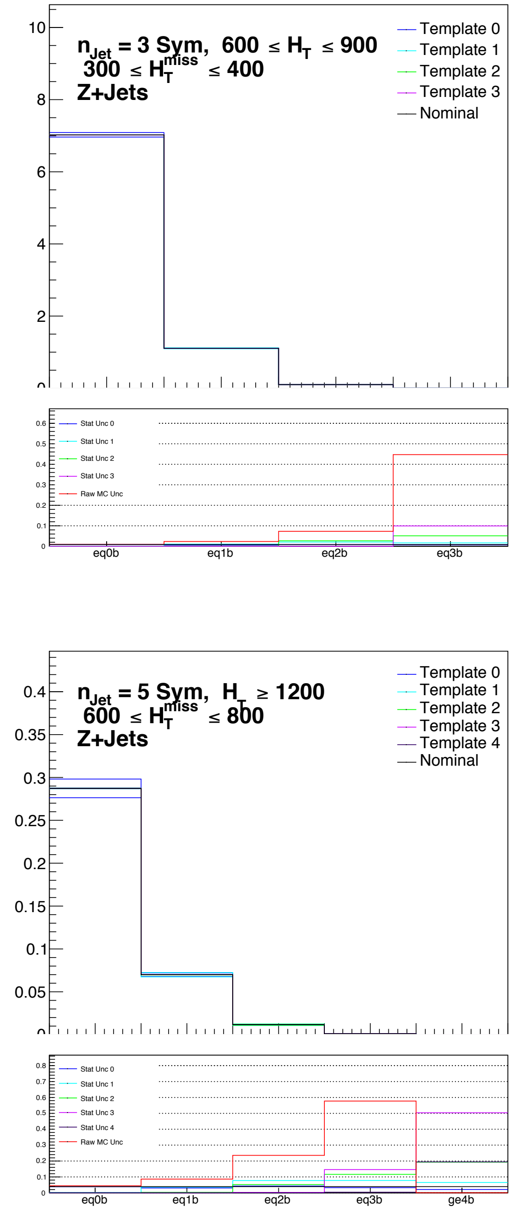

Figure 7.2.: Systematic templates from toys for $Z(\rightarrow \nu\bar{\nu}) + \text{jets}$. The red line represents statistical uncertainty of direct b-tagging for comparison.

Chapter 8.

Background Estimation for the α_T analysis

8.1. Lost lepton background estimation

8.1.1. Transfer factor method

Estimation of the lost lepton background in the signal region relies on the use of transfer factors, which transform observed data counts $N_{obs}^{\mu+\text{jets}}\left(N_{jet}, H_T, N_b\right)$ in the $\mu+$jets control region in a category of (N_{jet}, H_T, N_b) to estimates of lost lepton background $N_{pred}^{\text{t}\bar{\text{t}}\text{W}}\left(N_{jet}, H_T, N_b\right)$ in the corresponding bin in signal region. Transfer factors are defined as the ratio of event yields from MC for the same (N_{jet}, H_T, N_b) category:

$$TF^{\mu+\text{jets},\text{t}\bar{\text{t}}\text{W}}\left(N_{jet}, H_T, N_b\right) = \frac{N_{MC}^{\text{t}\bar{\text{t}}\text{W}}\left(N_{jet}, H_T, N_b\right)}{N_{MC}^{\mu+\text{jets}}\left(N_{jet}, H_T, N_b\right)} \tag{8.1}$$

The prediction of lost lepton background in each (N_{jet}, H_T, N_b) category can be written as:

$$\begin{aligned} N_{pred}^{\text{t}\bar{\text{t}}\text{W}}\left(N_{jet}, H_T, N_b\right) &= TF^{\mu+\text{jets},\text{t}\bar{\text{t}}\text{W}} \times N_{obs}^{\mu+\text{jets}}\left(N_{jet}, H_T, N_b\right) & (8.2) \\ &= \frac{N_{MC}^{\text{t}\bar{\text{t}}\text{W}}\left(N_{jet}, H_T, N_b\right)}{N_{MC}^{\mu+\text{jets}}\left(N_{jet}, H_T, N_b\right)} \times N_{obs}^{\mu+\text{jets}}\left(N_{jet}, H_T, N_b\right) & (8.3) \end{aligned}$$

Transfer factors are robust against systematic effects, which cancel out in the ratio of simulation in signal and control regions. The selection for the $\mu+$jets control region mimics the signal region selection to ensure a sample enriched in $W+$jets and $t\bar{t}+$jets events and suppressed signal contamination for accurate estimates of lost lepton backgrounds. In addition, categorizations of the signal region and $\mu+$jets control region are identical to mitigate any potential systematic effects. Figure 8.1 shows the value of transfer factors $TF^{\mu+\text{jets},t\bar{t}W}$.

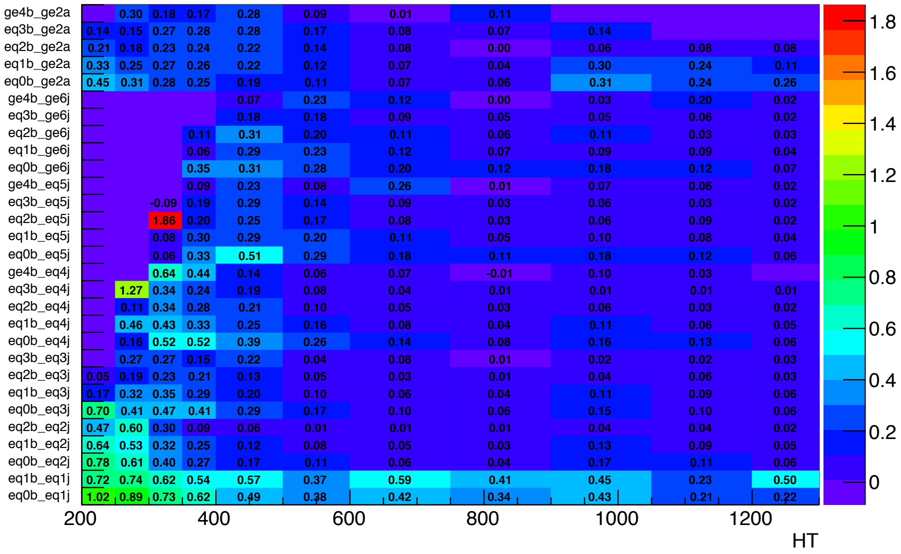

Figure 8.1.: Transfer factors $\mu+$jets $\to$ $t\bar{t}W$ for each (N_{jet}, H_T, N_b) category

8.1.2. $\not{H}_T$ templates

While transfer factors provide data-driven estimates for each (N_{jet}, H_T, N_b) category, estimates of lost lepton background along the $\not{H}_T$ dimension are provided with MC templates. Estimates for lost lepton background in each $(N_{jet}, H_T, N_b, \not{H}_T)$ category can be rewritten as:

$$N_{pred}^{t\bar{t}W}\left(N_{jet}, H_T, N_b, \not{H}_T\right) = \frac{N_{MC}^{t\bar{t}W}\left(N_{jet}, H_T, N_b, \not{H}_T\right)}{N_{MC}^{\mu+\text{jets}}\left(N_{jet}, H_T, N_b\right)} \times N_{obs}^{\mu+\text{jets}}\left(N_{jet}, H_T, N_b\right) \quad (8.4)$$

The normalization for each $\not{H}_T$ template is fixed by the transfer factor and its shape is taken from simulation. Validation of $\not{H}_T$ templates is described in Section 8.1.3.

8.1.3. Systematic uncertainties

Pileup reweighting

Simulation samples are reweighed by the distribution of number of interactions in data, as described in Section 6.3.1. The uncertainty on the inelastic proton-proton cross section of 5% is propagated by obtaining pileup weights for the cross section at ± 1 sigma values. The uncertainty derived from this effect is typically at the few percent level on the lost lepton yield prediction.

$\mathrm{W} + $ jets and $\mathrm{t\bar{t}}$ composition

The admixture of $\mathrm{W} + $ jets and $\mathrm{t\bar{t}} + $ jets in the signal and $\mu + $ jets control region may be different, due to different kinematic selections for each region. Any potential bias introduced due to this admixture difference is addressed by including two separate systematic uncertainties which vary cross sections of $\mathrm{W} + $ jets and $\mathrm{t\bar{t}}$ process with the measurement of inclusive cross section of each process with the CMS experiment [86, 87].

***W*, *Z* and γ boson-p_{T} reweighting**

MC samples for leading backgrounds in the analysis are simulated at leading order accuracy. Missing higher order corrections can result in distortions in boson p_{T} spectra. Theoretical corrections [83] are applied to mitigate this effect, and a 100% uncertainty is assumed for these corrections. Corresponding effects on transfer factors are typically at the few percent level, and up to 10% in high H_T categories. Figure 8.2 shows the effect on transfer factors against the variables N_{jet} and H_T.

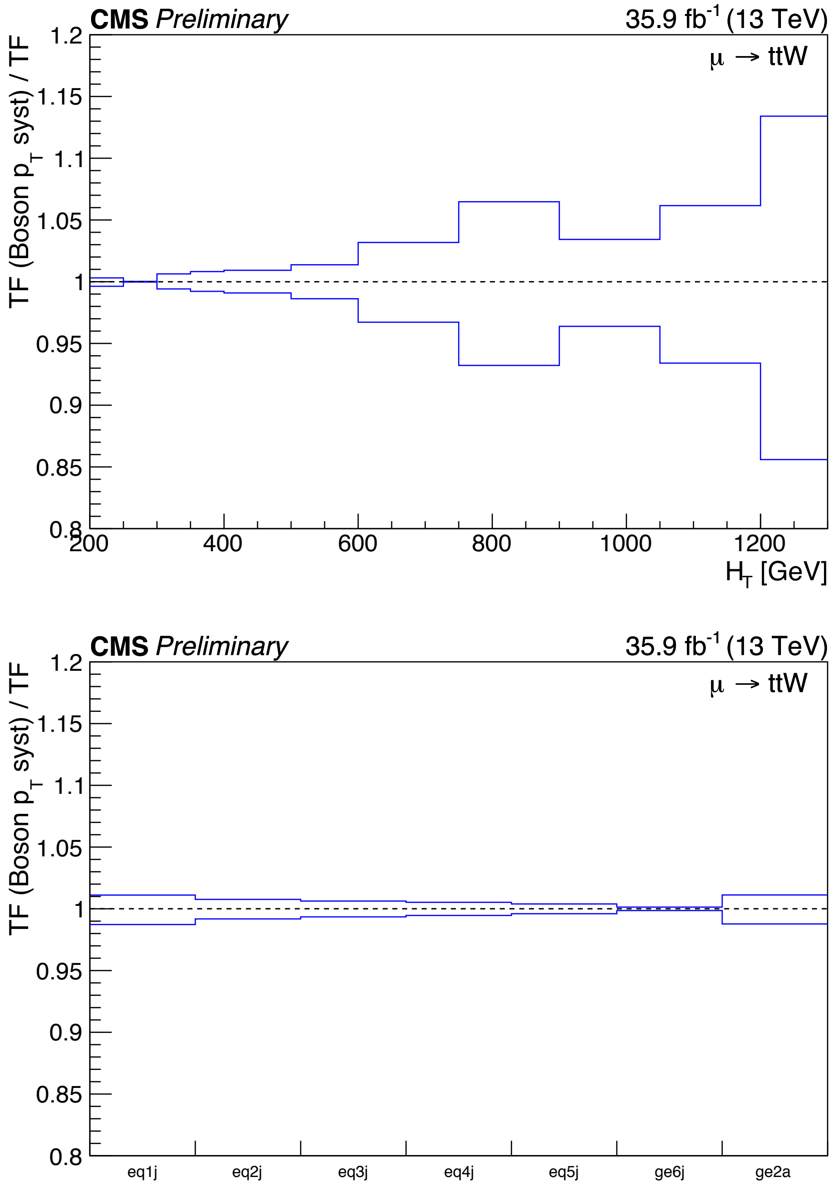

Figure 8.2.: Effect of boson-p_T uncertainty variation on transfer factors $\mu +$ jets $\rightarrow$ $t\bar{t}W$ against N_{jet} and H_T

Initial state radiation

Uncertainties for the ISR correction applied to $t\bar{t}+$ jets simulation described in Section 6.3.3 are assumed to have a relative uncertainty of 50%. Corresponding effects on transfer factors are typically at the few percent level as shown in Figure 8.3.

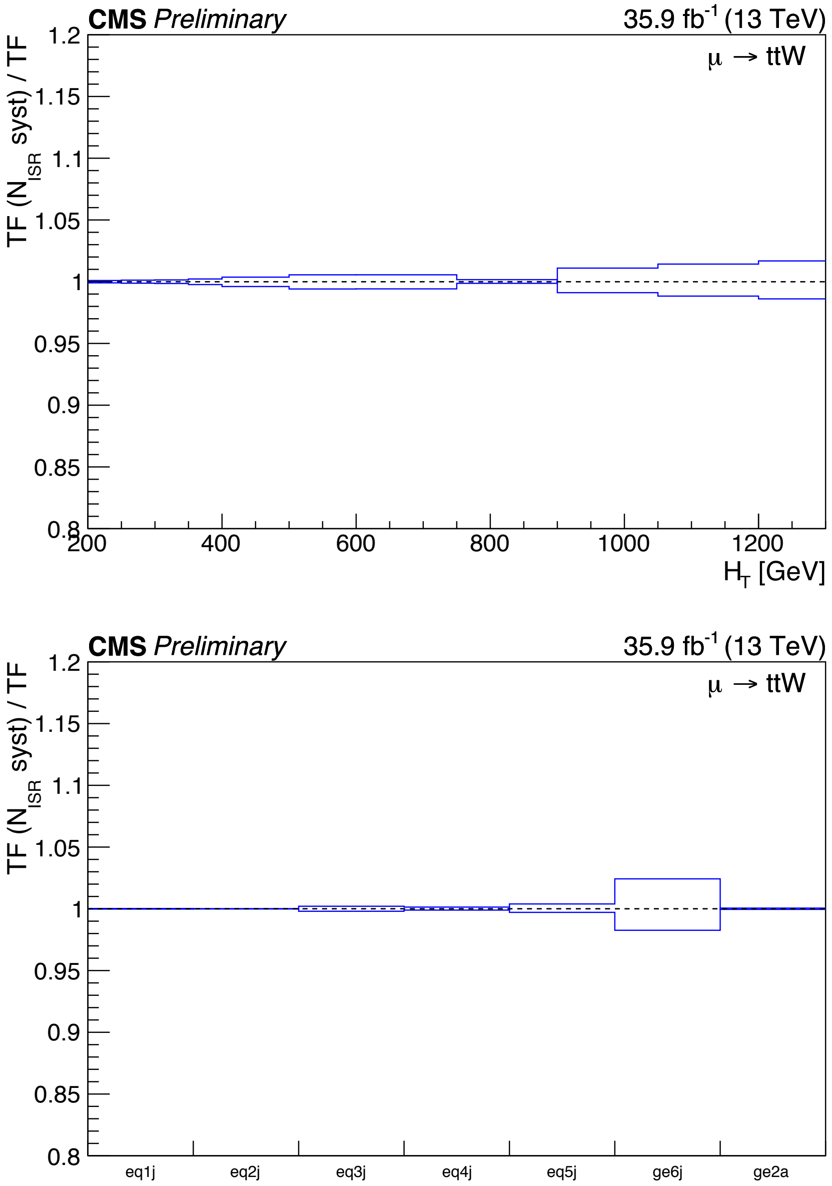

Figure 8.3.: Effect of ISR reweighting uncertainty variation on transfer factors $\mu + \text{jets} \rightarrow t\bar{t}W$ against N_{jet} and H_T

Trigger efficiency

Systematic uncertainties for trigger efficiency are taken as the difference between the measurements with the muon and electron reference trigger, as detailed in Section 5.3. Effects on transfer factors are typically $0 - 3\%$, as shown in Figure 8.4.

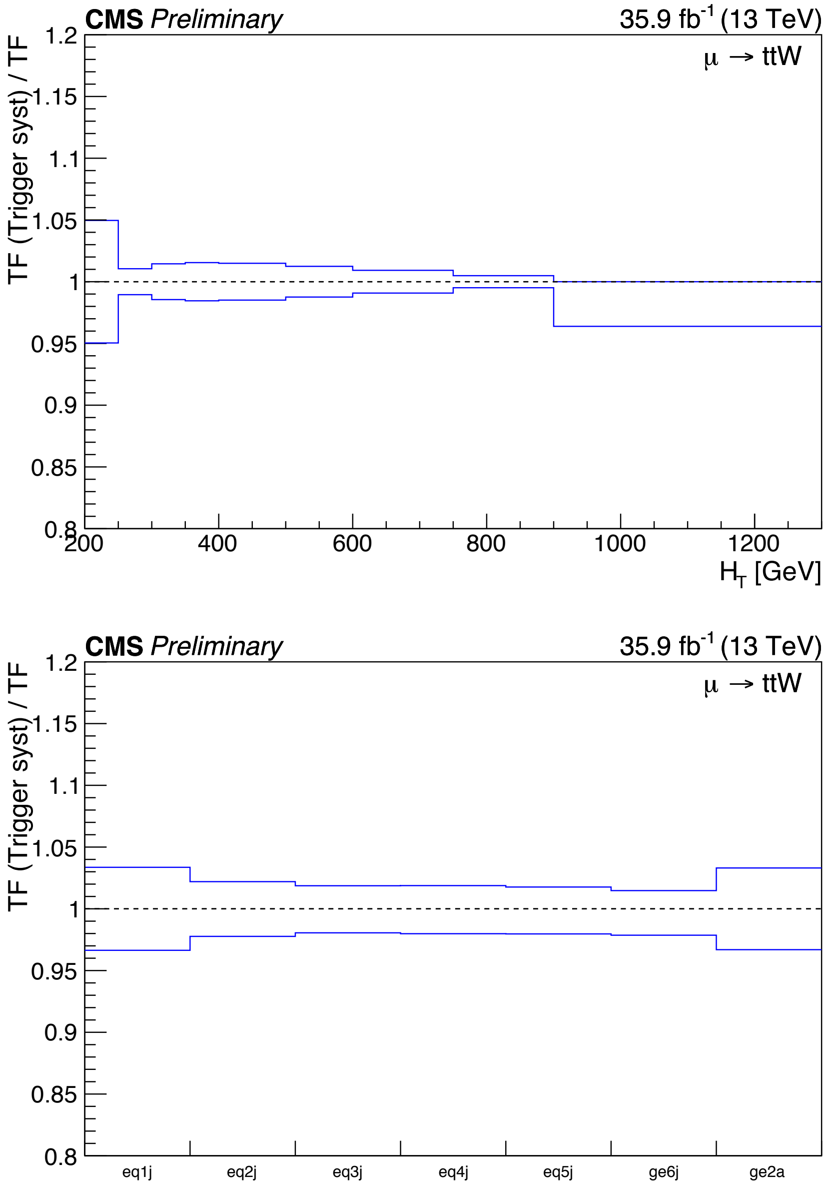

Figure 8.4.: Effect of trigger efficiency uncertainty variation on transfer factors $\mu + \text{jets} \rightarrow$ $t\bar{t}W$ against N_{jet} and H_T

Lepton efficiency

Events from $W + \text{jets}$ and $t\bar{t} + \text{jets}$ processes can enter the signal region if the leptons are not identified or out of the detector acceptance, or below the p_T or η thresholds, or not reconstructed properly. These effects are measured with a dedicated MC sample, obtained by the signal region selection but without lepton vetoes. Lepton reconstruction efficiencies are varied up and down within their uncertainties and their effects on the transfer factors are inspected. The effect is found to be at most 2% in the signal region. In addition, uncertainties for lepton efficiency can affect yields in the $\mu +$ jets and $\mu\mu +$ jets control region. The effect is also studied in the same way by varying the lepton efficiency within uncertainty, and found to be in the range of $0 - 3\%$.

B-tagging efficiency

Similar to the lepton efficiency uncertainties, the b-tagging efficiency is varied up and down within its uncertainty. Their effects on transfer factors are expected to be small since no extrapolation across different N_b categories is performed in the lost lepton background estimation. Efficiencies for the identification for b-jets and c-jets are varied together, while efficiencies associated with light jets are varied separately. The effects on transfer factors are shown in Figure 8.5-8.6.

Jet energy scale

Systematic uncertainties with jet energy corrections are propagated through the analysis. The corrections are varied up and down within their uncertainties and variations on transfer factors are inspected. The effects are typically in range of 3% to 6%.

Systematic uncertainty in data-driven tests

To address additional systematic effects, a suite of data-driven tests are performed to inspect simulation modeling and derive systematic uncertainties. In data-driven tests, data in control samples are used to further probe sources of bias in transfer factors due to extrapolation in the α_T and $\Delta\phi^*_{\mathrm{min}}$ variable and the W boson polarization. Events in one control sample (probe region) are used to predict events from another control sample (test region), using transfer factors with the ratio in

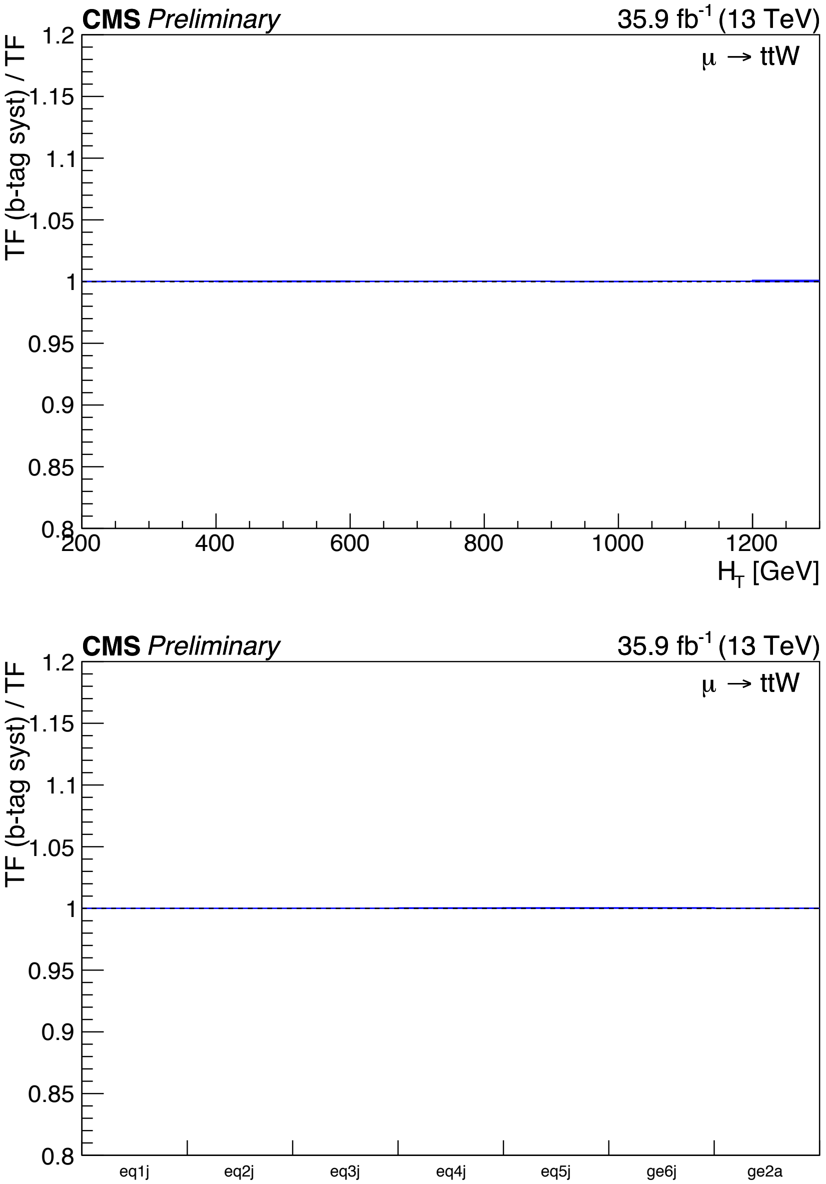

Figure 8.5.: Effect of b-tagging efficiency for b-jets and c-jets uncertainty variation on transfer factors $\mu + \text{jets} \rightarrow t\bar{t}W$ against N_{jet} and H_T

simulation:

$$N^{test}_{pred} = \frac{N^{test}_{MC}}{N^{probe}_{MC}} \times N^{probe}_{data} \tag{8.5}$$

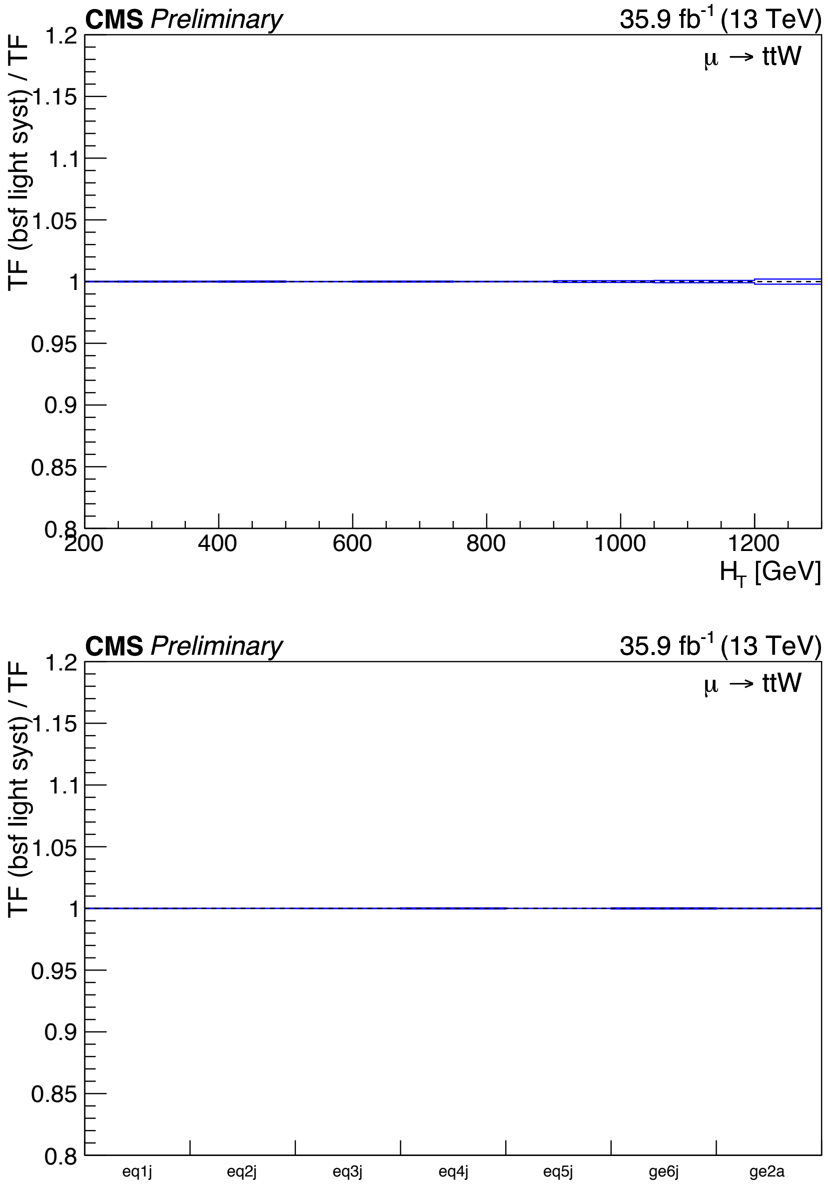

Figure 8.6.: Effect of b-tagging efficiency for light jets uncertainty variation on transfer factors $\mu + \text{jets} \rightarrow t\bar{t}W$ against N_{jet} and H_T

where N^{probe}_{data}, N^{probe}_{MC} and N^{test}_{MC} are the data count, MC yield in the probe region, and the MC yield in the test region respectively. The prediction N^{test}_{pred} is contrasted against the data count in the test region N^{test}_{data}, and the closure between the test region and probe region is defined as the ratio

$$R_{\text{closure}} = \frac{N_{data}^{test} - N_{data}^{pred}}{N_{data}^{pred}} \tag{8.6}$$

$R_{closure}$ indicates the level of agreement between the test and probe region. Data-driven tests are performed in each N_{jet} and H_T category separately. For each category, the systematic uncertainty is defined by the value of $R_{closure}$ added in quadrature to statistical uncertainties. Systematics derived using data-driven tests are applied to transfer factors per H_T category (correlated over N_{jet}) and per N_{jet} category (correlated over H_T). All sources of uncertainty derived with data-driven tests are explained in the following.

Extrapolation in $\boldsymbol{\alpha_T}$ and $\boldsymbol{\Delta\phi^*_{\min}}$

No α_T and $\Delta\phi^*_{\min}$ requirements are applied in the $\mu +$ jets and $\mu\mu +$ jets control region, while α_T and $\Delta\phi^*_{\min}$ cuts are required in the signal region to suppress QCD background. Modeling of the α_T and $\Delta\phi^*_{\min}$ variable is derived from the $\mu +$ jets sample with a dedicated data-driven method, and corresponding systematic uncertainties due to different α_T and $\Delta\phi^*_{\min}$ requirements in signal and control regions are estimated.

For α_T extrapolation, the $\mu +$ jets sample is divided into events with the same α_T requirement as in the signal region and the requirement inverted, as the test and probe region respectively. Data-driven tests are performed in each N_{jet} and H_T category. Figure 8.7 shows results of these tests, and the gray band shows the systematic uncertainty propagated through the analysis.

Similar for $\Delta\phi^*_{\min}$ extrapolation, $\mu +$ jets sample is divided into events with the same $\Delta\phi^*_{\min}$ requirement as in the signal region and the requirement inverted, as the test and probe region respectively. Figure 8.7 shows the results of these tests, and the gray band shows again the systematic uncertainty propagated through the analysis.

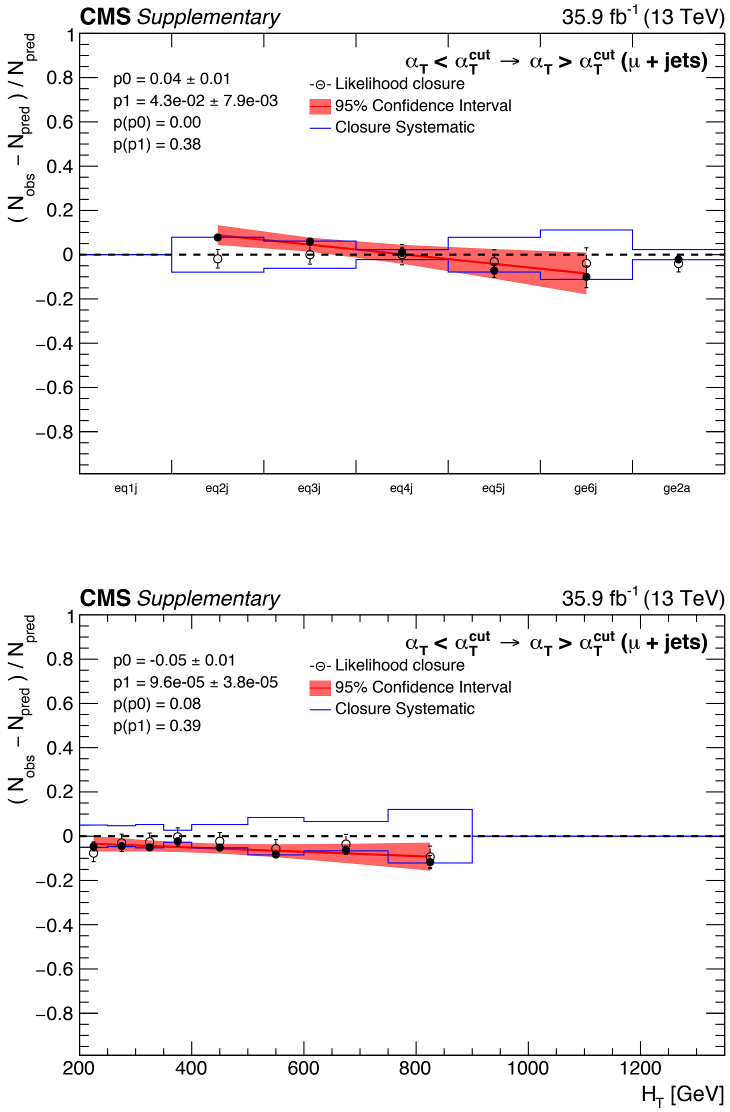

Figure 8.7.: Data-driven test for modeling of the α_T variable in each N_{jet} and H_T category. The black points indicate the closure R_{closure} defined by Equation 8.6. Each blue band is derived by summing in quadrature the central value and the statistical uncertainty of each black point. The red band is derived by performing a linear orthogonal polynomial fit, described in Section 8.1.3 to the black points and varying the linear parameter within 95% confidence interval. Finally the white points are derived by implementing the closure tests in a likelihood with all theoretical and experimental systematic uncertainties as nuisance parameters and R_{closure} as free parameters and performing a maximum likelihood fit to extract the parameters R_{closure}.

Non-closure is observed in each test. A systematic uncertainty, calculated by adding the central value R_{closure} and its statistical uncertainty in quadrature, (overlaid on Figure 8.7-8.8 as blue solid lines) is derived to account for the non-closure.

The effect of W boson polarization on lepton acceptance

The left-handedness of the electroweak interaction, described in Chapter 2, leads to left-handed W bosons being more copiously produced in proton-proton collisions [88] than right-handed W bosons. As there are no right-handed neutrinos, a left-handed W^+ (W^-) boson decays more often to a left-handed neutrino (left-handed electron) along the direction of motion of the W boson and a right-handed positron (right-handed anti-neutrino) in the opposite direction. This means neutrinos from the W^+ decay are more boosted than those from the W^- decay. The signal region selection, which primarily aims at selecting events with high $\not{E}_T$, accepts more events of μ^+ than μ^- in the $\mu+$jets control region. To check the modeling of W polarization, a specific data-driven test is performed by dividing the $\mu+$jets control region into events with μ^+ or μ^-. Figure 8.9 shows results of the test. A good closure is observed and a systematic uncertainty (blue solid line) derived from adding the closure and its statistical uncertainty in quadrature.

Systematic uncertainty in $\not{H}_T$ templates

Background estimates of lost lepton background for each (N_{jet}, N_b, H_T) category are derived with the transfer factor method as described in Section 8.1.1 and relevant systematic uncertainties are estimated with MC-based and data-driven methods as explained above. Another data-driven method is used to address potential biases and validate the assumption of good modeling in the $\not{H}_T$ dimension. The level of closure as a function of $\not{H}_T$ is utilized to determine alternative templates to cover sources of bias for the lost lepton background estimation in the likelihood model.

When looking at the $\not{H}_T$ dimension inclusively in H_T, significant bias can arise from theoretical uncertainties by mixing events at different energy scales. These biases can be mitigated by binning in H_T as a proxy of the energy scale of each event. This assumption is validated using the $\mu+$jets control region for lost lepton

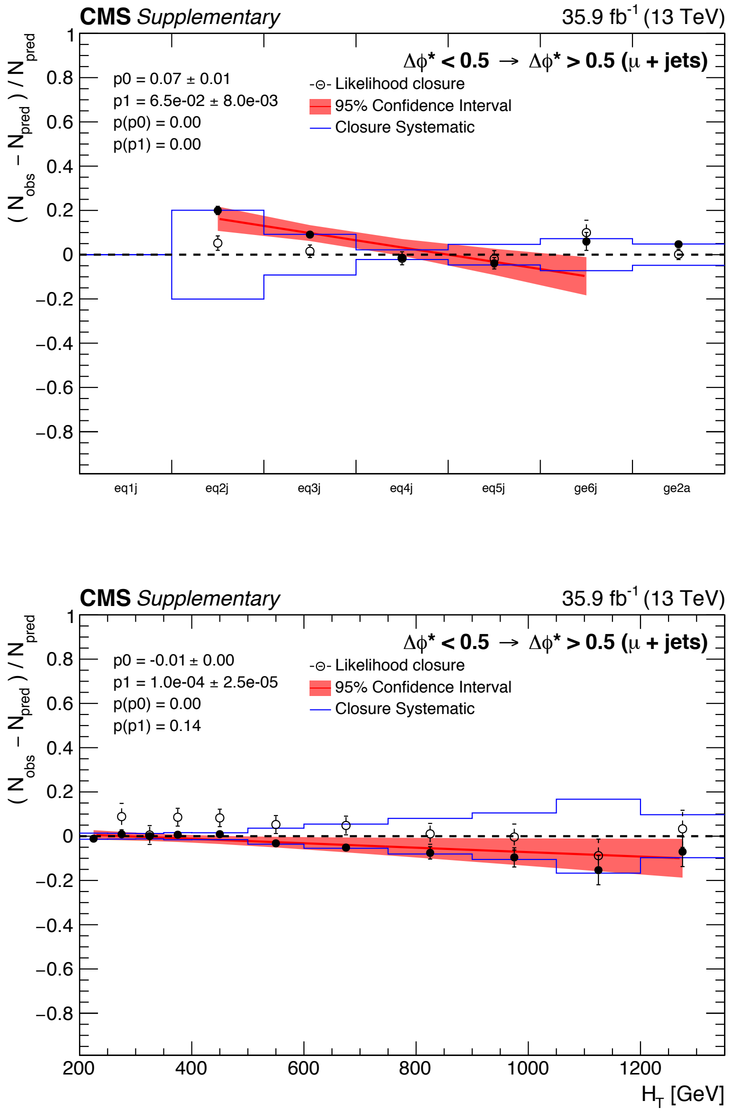

Figure 8.8.: Data-driven test for modeling of the $\Delta\phi^*_{\text{min}}$ variable in each N_{jet} and H_T category. The black points indicate the closure R_{closure} defined by Equation 8.6. Each blue band is derived by summing in quadrature the central value and the statistical uncertainty of each black point. The red band is derived by performing a linear orthogonal polynomial fit, described in Section 8.1.3 to the black points and varying the linear parameter within 95% confidence interval. Finally the white points are derived by implementing the closure tests in a likelihood with all theoretical and experimental systematic uncertainties as nuisance parameters and R_{closure} as free parameters and performing a maximum likelihood fit to extract the parameters R_{closure}.

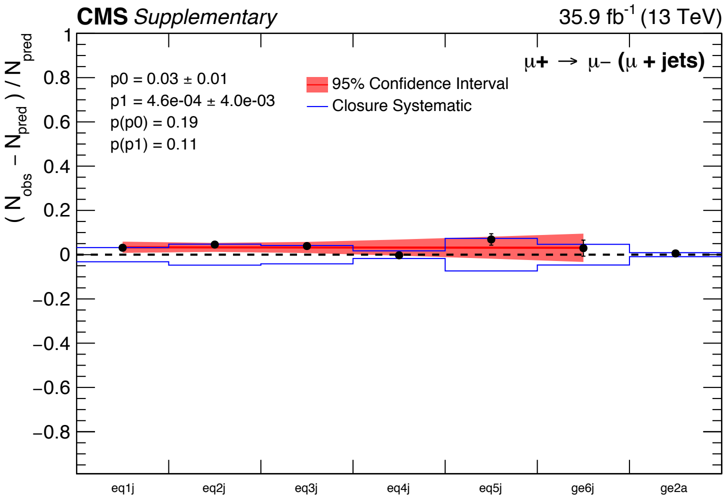

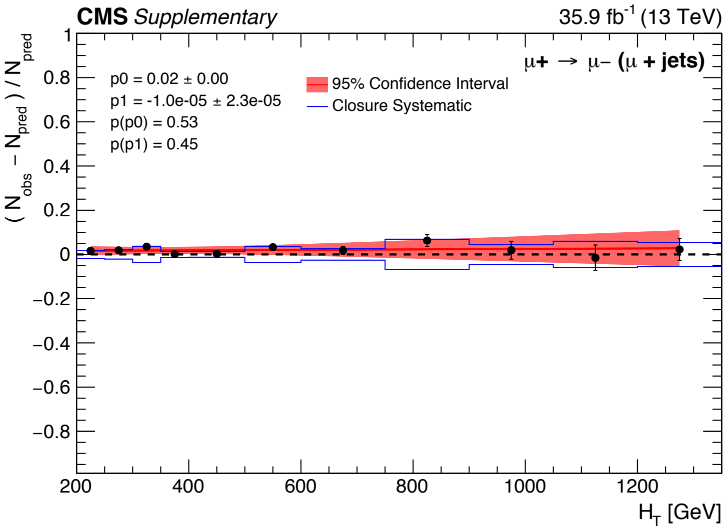

Figure 8.9.: Data-driven test for modeling of the α_T variable in each N_{jet} and H_T category. The black points indicate the closure R_{closure} defined by Equation 8.6. Each blue band is derived by summing in quadrature the central value and the statistical uncertainty of each black point. The red band is derived by performing a linear orthogonal polynomial fit, described in Section 8.1.3 to the black points and varying the linear parameter within 95% confidence interval.

background. For each (N_{jet}, H_T, N_b) category, the ratio of data to MC distribution in $\not{H}_T$ is parametrized as a first order (linear) orthogonal polynomial. The n-th order orthogonal polynomial is defined as

$$f_n(x) = \sum_{k=0}^{k=n} (p_k) \times (\bar{x} - x)^k \tag{8.7}$$

where $\bar{x}$ is the weighted mean of the distribution [89]. One special property of 8.7 is that the parameters p_k as odd numbers k are decorrelated to those with even numbers. For a linear orthogonal polynomial, the normalization parameter (p_0) and shape parameter (p_1) are not correlated. Mathematically, the normalization estimate for each (N_{jet}, H_T, N_b) category corresponds to the p_0 parameter and is estimated separately by the transfer factor method, while the p_1 parameter corresponds to the shape distribution in the $\not{H}_T$ dimension. Figure 8.10 shows the best fit value for the p_1 parameter in units of the associated uncertainty (statistical 'pull'), in each (N_{jet}, N_b, H_T) category. No significant bias is found in the modeling of $\not{H}_T$.

Two set of systematic uncertainties in the $\not{H}_T$ dimension are derived with the $\mu +$ jets control region in the N_{jet} and H_T dimension separately. Systematic uncertainties in the H_T dimension address potential bias from the mixing of different energy scales of each event, while those in the N_{jet} dimension provide handles on mis-modeling from radiation of additional partons. A simultaneous fit is performed with all (N_{jet}, N_b, H_T) categories. For H_T-shape systematics, one nuisance parameter for the p_1 parameter is injected per H_T bin and correlated across the N_{jet} dimension. The N_{jet}-shape systematics are derived instead with the correlation pattern reversed. Figure 8.11 shows the post-fit values and uncertainties for the p_1 parameters. The post-fit value and uncertainty for each p_1 parameter is added in quadrature, and the resulting sum is used to define alternative templates for the $\not{H}_T$ dimension for the likelihood model. Figure 8.12 shows the systematic uncertainty per 100 GeV-interval in $\not{H}_T$ from the derived uncertainties.

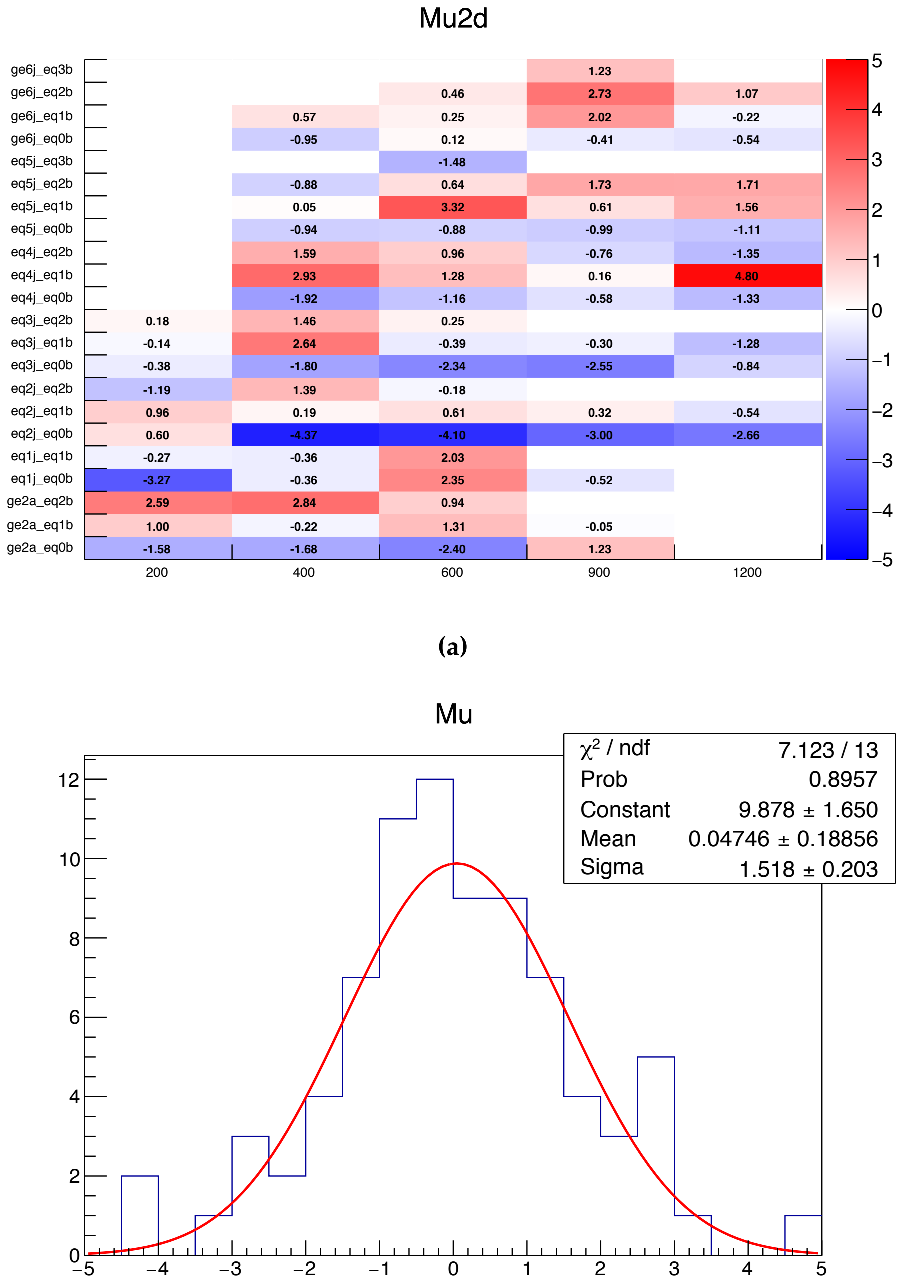

	200	400	600	900	1200
ge6j_eq3b				1.23	
ge6j_eq2b			0.46	2.73	1.07
ge6j_eq1b		0.57	0.25	2.02	-0.22
ge6j_eq0b		-0.95	0.12	-0.41	-0.54
eq5j_eq3b			-1.48		
eq5j_eq2b		-0.88	0.64	1.73	1.71
eq5j_eq1b		0.05	3.32	0.61	1.56
eq5j_eq0b		-0.94	-0.88	-0.99	-1.11
eq4j_eq2b		1.59	0.96	-0.76	-1.35
eq4j_eq1b		2.93	1.28	0.16	4.80
eq4j_eq0b		-1.92	-1.16	-0.58	-1.33
eq3j_eq2b	0.18	1.46	0.25		
eq3j_eq1b	-0.14	2.64	-0.39	-0.30	-1.28
eq3j_eq0b	-0.38	-1.80	-2.34	-2.55	-0.84
eq2j_eq2b	-1.19	1.39	-0.18		
eq2j_eq1b	0.96	0.19	0.61	0.32	-0.54
eq2j_eq0b	0.60	-4.37	-4.10	-3.00	-2.66
eq1j_eq1b	-0.27	-0.36	2.03		
eq1j_eq0b	-3.27	-0.36	2.35	-0.52	
ge2a_eq2b	2.59	2.84	0.94		
ge2a_eq1b	1.00	-0.22	1.31	-0.05	
ge2a_eq0b	-1.58	-1.68	-2.40	1.23	

(a)

(b)

Figure 8.10.: The best fit value for the linear parameter in units of the associated statistical uncertainty, i.e. the statistical pull, as a function of N_{jet}, N_b, and H_T. (8.11a) The histogram of the pull values. (8.11b)

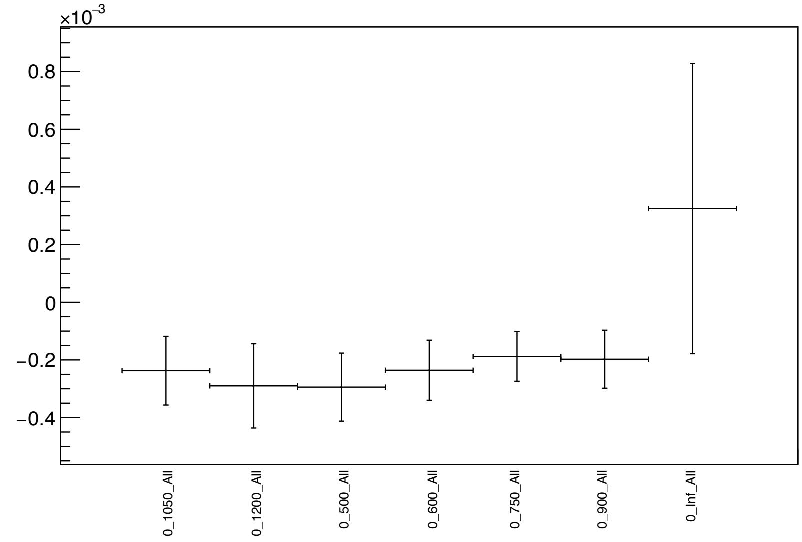

(a)

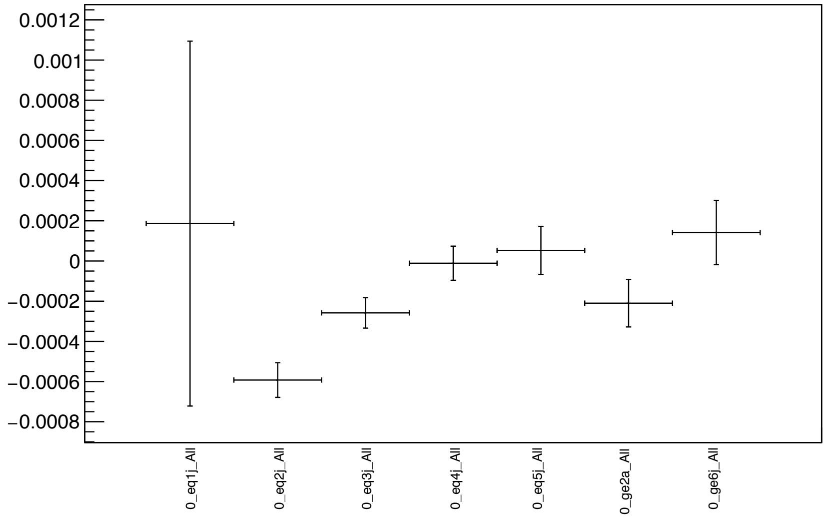

(b)

Figure 8.11.: Post fit values and uncertainties of the linear parameters used to determine the systematics, correlated in N_{jet} (8.12a) and H_T (8.12b).

8.2. $Z(\rightarrow \nu\bar{\nu}) + $ jets background estimation

8.2.1. Transfer factor method

Background estimates for $Z(\rightarrow \nu\bar{\nu}) +$ jets are derived in a similar way as in Section 8.1, but in this case using the transfer factor from the $\mu\mu +$ jets control region.

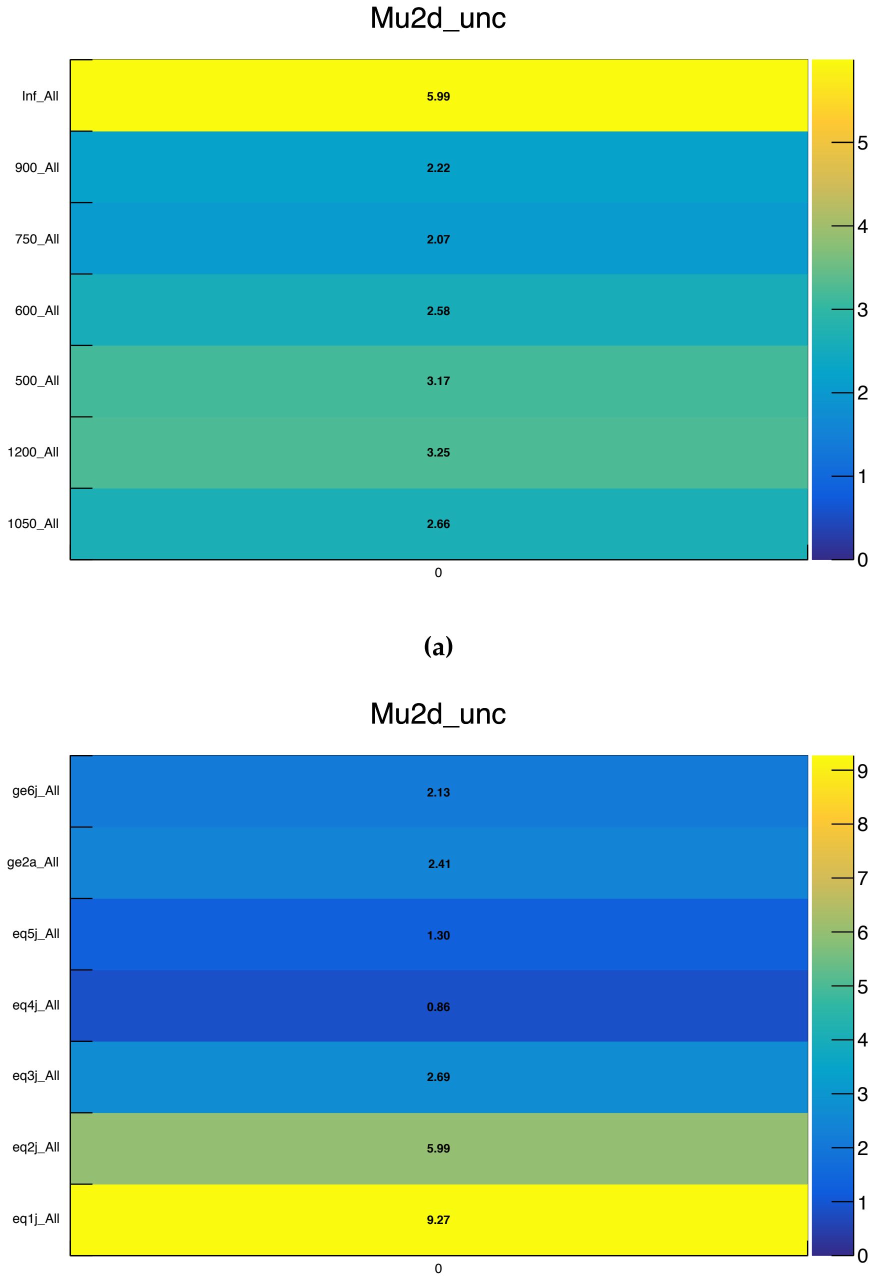

(a)

(b)

Figure 8.12.: Systematic uncertainties (%) per 100 GeV-interval in $\not{H}_T$ for effects correlated in (8.13a) N_{jet} and (8.13b) H_T, as determined in the $\mu +$jets control region.

The transfer factors transform observed data counts $N_{obs}^{\mu\mu+\text{jets}}\left(N_{jet}, H_T, N_b\right)$ in a category of (N_{jet},H_T,$N_b = 0\,,\, \geq 1$) of the $\mu\mu +$jets control region to estimates of

$\mathrm{Z}(\to \nu\bar{\nu}) + \text{jets}$ background $N_{pred}^{\text{Z+jets}}\left(N_{jet}, H_T, N_b\right)$ in the same category in the signal region:

$$TF^{\mu\mu\text{+jets,Z+jets}}\left(N_{jet}, H_T, N_b\right) = \frac{N_{MC}^{\text{Z+jets}}\left(N_{jet}, H_T, N_b\right)}{N_{MC}^{\mu\mu\text{+jets}}\left(N_{jet}, H_T, N_b\right)} \tag{8.8}$$

$$\begin{aligned} N_{pred}^{\text{Z+jets}}\left(N_{jet}, H_T, N_b\right) &= TF^{\mu\mu\text{+jets,Z+jets}} \times N_{obs}^{\mu\mu\text{+jets}}\left(N_{jet}, H_T, N_b\right) & (8.9)\\ &= \frac{N_{MC}^{\text{Z+jets}}\left(N_{jet}, H_T, N_b\right)}{N_{MC}^{\mu\mu\text{+jets}}\left(N_{jet}, H_T, N_b\right)} \times N_{obs}^{\mu\mu\text{+jets}}\left(N_{jet}, H_T, N_b\right) & (8.10) \end{aligned}$$

In particular, background estimates with transfer factors fix the integrated normalization for each (N_{jet},H_T,$N_b \geq 1$) category. Within each category, estimates for each N_b bins are obtained from simulation.

Similar to the lost lepton background estimation, the selection criteria for $\mu\mu +$ jets control region closely mimic those for the signal region. The only difference is the requirement of a di-muon final state and additional kinematic requirements, to ensure a $\mathrm{Z}(\to \mu\mu) + \text{jets}$-enriched control region, as described in Section 5.4.3.

8.2.2. $\not{H}_T$ templates

Similarly to the lost lepton background estimation, for each (N_{jet}, H_T, N_b) category, estimates of $\mathrm{Z}(\to \nu\bar{\nu}) + \text{jets}$ along the $\not{H}_T$ dimension are provided with MC templates and equation 8.9 can be rewritten as:

$$N_{pred}^{\text{Z+jets}}\left(N_{jet}, H_T, N_b, \not{H}_T\right) = \frac{N_{MC}^{\text{Z+jets}}\left(N_{jet}, H_T, N_b, \not{H}_T\right)}{N_{MC}^{\mu\mu\text{+jets}}\left(N_{jet}, H_T, N_b\right)} \times N_{obs}^{\mu\mu\text{+jets}}\left(N_{jet}, H_T, N_b\right) \tag{8.11}$$

8.2.3. Systematic uncertainties

Relevant uncertainties, and their representative magnitudes and assumptions on inter-bin correlations, for $\mathrm{Z}(\to \nu\bar{\nu}) + \text{jets}$ background estimation are listed in Table 8.1. Sources of uncertainty are divided into three categories. The first category includes theoretical and experimental effects addressed by alternative MC templates for $\pm 1\sigma$ variations on these effects. The second category includes uncertainties derived from closure tests and $\not{H}_T$ validation, as described in Section 8.1.3 and 8.1.3.

Source of uncertainty	Nuisance parameters / correlation	Range (%)	Type
Finite-size simulated samples	1 per (N_{jet}, H_T, N_b, $\not{H}_T$) category	1–100	Unique
Minimum bias cross section (pileup)	1, correlated across N_{jet}, H_T, N_b, $\not{H}_T$	2.3–2.8	Shared
μ_R / μ_F scales	1, correlated across N_{jet}, H_T, N_b, $\not{H}_T$	0.9–4.7	Shared
Parton density functions	1, correlated across N_{jet}, H_T, N_b, $\not{H}_T$	0.0–3.3	Shared
QCD + EWK NLO corrections	1, correlated across N_{jet}, H_T, N_b, $\not{H}_T$	2.2–14.3	Shared
Signal trigger efficiency	1, correlated across N_{jet}, H_T, N_b, $\not{H}_T$	0.0–2.0	Shared
Lepton efficiency (selection)	1, correlated across N_{jet}, H_T, N_b, $\not{H}_T$	0.0–4.2	Unique
Jet energy scale	1, correlated across N_{jet}, H_T, N_b, $\not{H}_T$	5.3–8.0	Shared
b-quark tag efficiency	1, correlated across N_{jet}, H_T, N_b, $\not{H}_T$	0.3–0.6	Shared
light-quark mis-tag probability	1, correlated across N_{jet}, H_T, N_b, $\not{H}_T$	0.2–1.8	Shared
α_T extrapolation	1 per N_{jet}, 1 per H_T category	3.3–9.4 (N_{jet}), 2.1–5.9 (H_T)	Unique
$\Delta\phi^*_{\min}$ extrapolation	1 per N_{jet}, 1 per H_T category	2.7–22. (N_{jet}), 1.6–18. (H_T)	Unique

Table 8.1.: Sources of systematic uncertainties in the transfer factors used to estimate the $Z(\rightarrow \nu\bar{\nu}) +$ jets background based on the $\mu\mu +$ jets control region. Also shown are the nuisance parameters and correlation scheme, as well as representative ranges for the relative uncertainties in percentage. The representative range is taken from the 16% and 84% percentiles on the transfer factor variations across all analysis bins for each source of systematic. The "type" refers to whether the nuisance parameters are unique to the $Z(\rightarrow \nu\bar{\nu}) +$ jets background or shared with the lost lepton background estimate.

The $\not{H}_T$ validation for the $Z(\rightarrow \nu\bar{\nu}) +$ jets background estimation employs the same method as the lost lepton background estimation in Section 8.1.3. To mimic the kinematics in the signal region closely, the modeling of the $\not{H}_T$ dimension is validated with the $\mu\mu +$ jets control region, instead of the $\mu +$ jets control region. Figure 8.13 shows the statistical pull of the p_1 parameters in each (N_{jet},H_T,N_b) category from the validation. No significant biases or trends are observed with the simulation modeling of the $\not{H}_T$ variable. Systematic uncertainties and templates are also derived in the $\mu\mu +$ jets control region in a similar way as with the lost lepton background estimation. Figure 8.14 shows the best fit values and uncertainties for the p_1 parameters, and Figure 8.15 shows the systematic uncertainty in the final open $\not{H}_T$ bin for each (N_{jet},H_T,N_b) category, typically at the level of $5 - 20\%$.

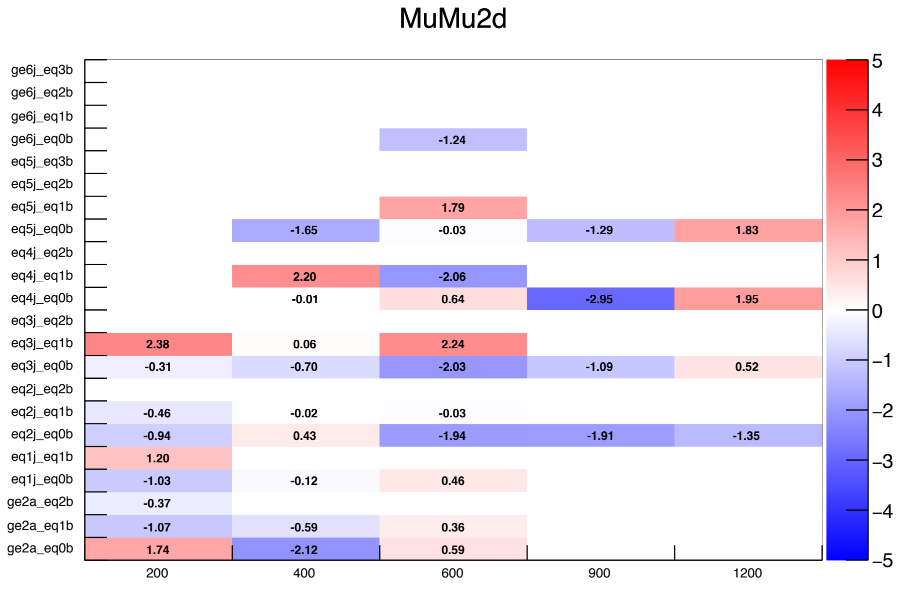

(a)

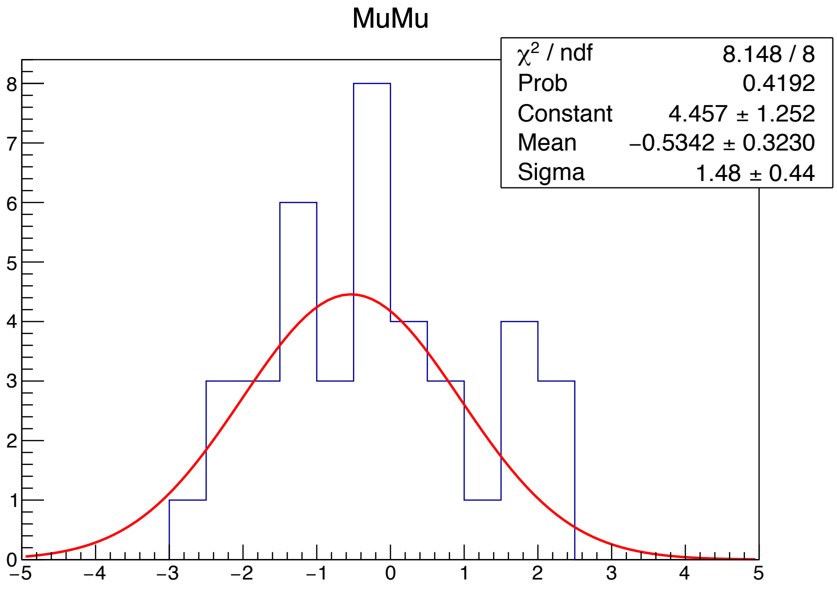

(b)

Figure 8.13.: The best fit value for the linear parameter in units of the associated statistical uncertainty, i.e. the statistical pull, as a function of N_{jet}, N_b, and H_T. (8.14a) The histogram of the pull values. (8.14b)

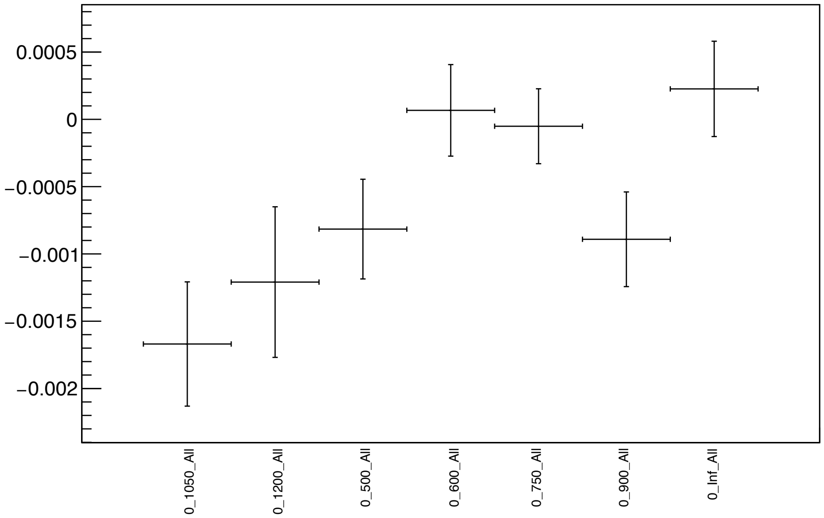

(a)

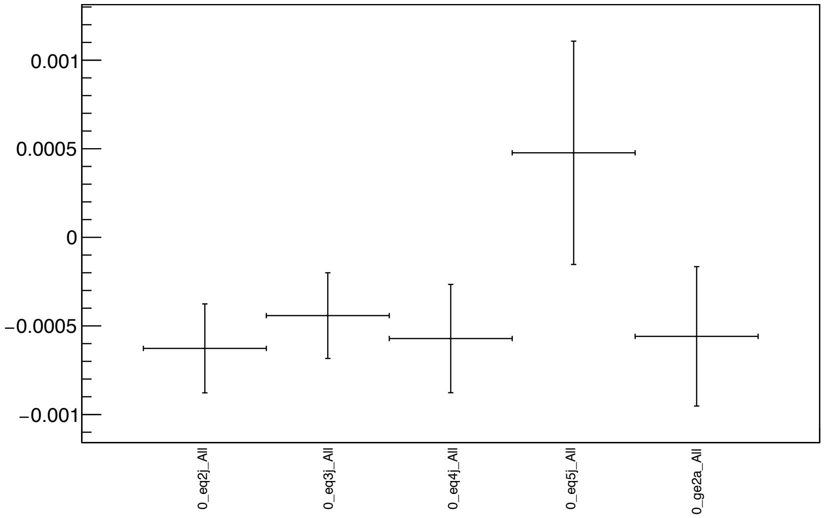

(b)

Figure 8.14.: Post fit values and uncertainties of the linear parameters used to determine the systematics, correlated in N_{jet} (8.15a) and H_T (8.15b).

8.2.4. Modeling of N_b templates

Data-driven estimates from the $\mu\mu +$jets control region are derived inclusively for categories with $N_b \geq 1$, and MC templates are used for the shape. A likelihood-

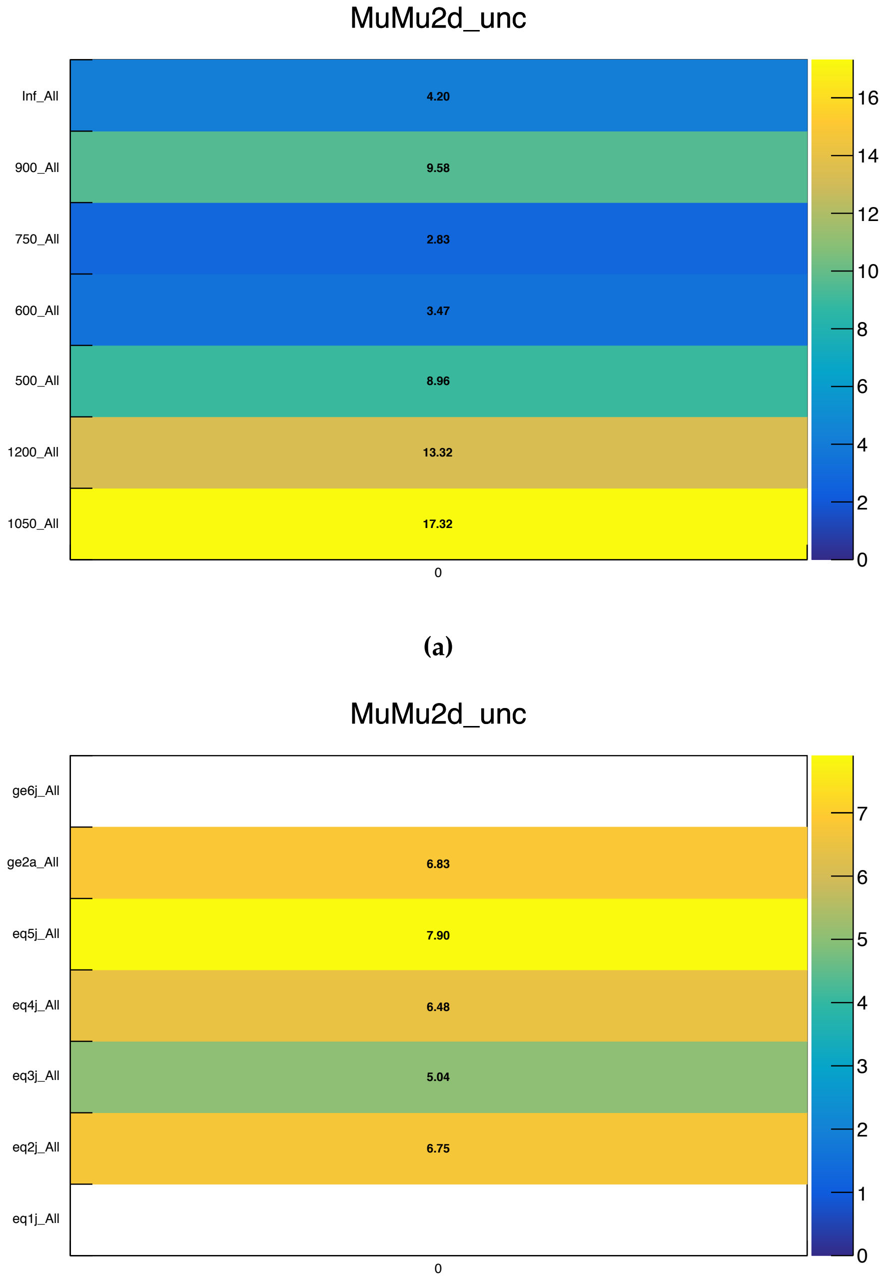

(a)

(b)

Figure 8.15.: Systematic uncertainties (%) per 100 GeV-interval in $\not{H}_T$ for effects correlated in (8.16a) N_{jet} and (8.16b) H_T, as determined in the $\mu\mu$ + jets control region.

based test is employed to scrutinize the modeling of N_b templates for the $Z(\rightarrow \nu\bar{\nu})$ + jets background estimation. A binned likelihood fit to data in the $\mu\mu$ + jets control region is performed. This likelihood model includes the same set of theoretical and experimental uncertainties described above, and flat unconstrained parameters per each (N_{jet},H_T,$N_b = 0$) or (N_{jet},H_T,$N_b \geq 1$) category. N_b templates from MC simulation are tested against data for potential discrepancies in modeling in the N_b dimension.

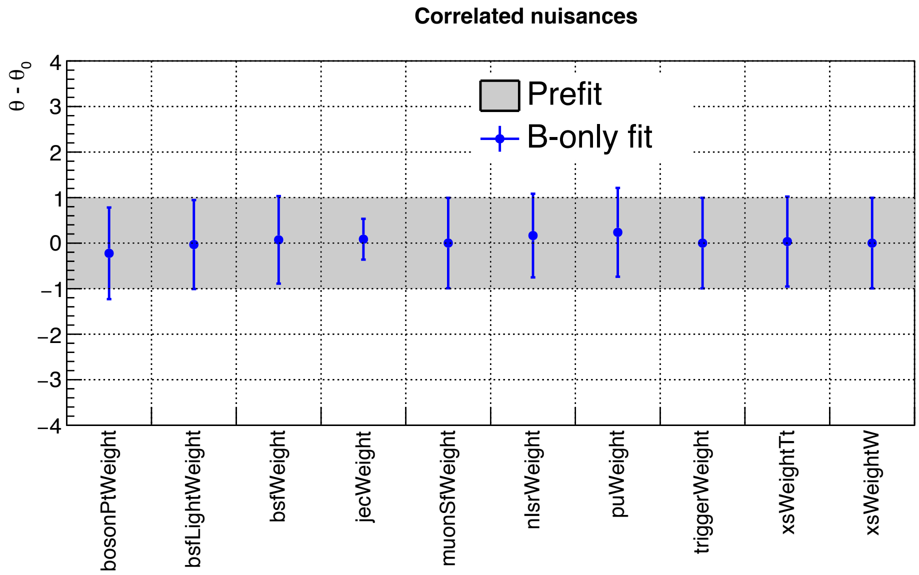

Figure 8.16.: Post-fit nuisances of a likelihood fit to data in the $\mu\mu +$ jets control region subdivided according to $N_b = 0$ and $N_b \geq 1$.

Figure 8.16 shows values and relevant uncertainties for post-fit nuisances from the likelihood fit. No significant bias are observed with the N_b modeling.

8.3. QCD multijet background estimation

One of the major challenges for the analysis is to make accurate estimates of the QCD multijet background, which arises from the production of quarks and gluinos via the strong interaction. The main strategy in the analysis to tackle this difficult background is to suppress the QCD events to a negligible level in the signal region imposing tight requirements on α_T, $\Delta\phi^*_{\mathrm{min}}$, $\not{H}_T/\not{E}_T$ and the forward jet veto described in Section 5.2. A data-driven method is then used to estimate any residual

QCD multijet contamination in the signal region, with three independent QCD-enriched sideband regions. Conservative systematic uncertainties are assigned to cover any potential bias with the method.

8.3.1. QCD-enriched sidebands

Estimates of the QCD backgrounds are determined using three independent sideband regions by inverting one or both requirements on the $\Delta\phi^*_{\rm min}$ and $\not{H}_T / \not{E}_T$ variable. Table 8.2 summarizes the definitions of the three sidebands. They are chosen to be QCD-enriched, but in a similar kinematic phase space as the signal region.

	$0.2 < \Delta\phi^*_{\rm min} < 0.5$	$\Delta\phi^*_{\rm min} > 0.5$
$1.25 < \not{H}_T / \not{E}_T < 3.0$	**A** (“Double sideband”)	**B** (“$\not{H}_T / \not{E}_T$ sideband”)
$\not{H}_T / \not{E}_T < 1.25$	**C** (“$\Delta\phi^*_{\rm min}$ sideband”)	**D** (“Signal region”)

Table 8.2.: Definitions of data sidebands used in the determination of the QCD multijet background in the signal region.

8.3.2. QCD estimation from sidebands

QCD estimates for the signal region are derived in each (N_{jet},H_T) category from three independent data sidebands. Contaminations from electroweak backgrounds (W + jets, $\mathrm{t\bar{t}}$ + jets and $\mathrm{Z}(\rightarrow \nu\bar{\nu})$ + jets) in the sideband regions could be significant and have to be estimated from the corresponding μ + jets and $\mu\mu$ + jets control regions (with the same inverted $\not{H}_T / \not{E}_T$ and $\Delta\phi^*_{\rm min}$ requirements as in the signal region), and data counts $N^{\rm QCD}_{obs}\left(N_{jet}, H_T\right)$ in each sideband region. One simultaneous fit for each data sideband and the corresponding μ + jets and $\mu\mu$ + jets control regions is performed to extract the data-driven corrections to QCD simulation. The likelihood model includes all relevant systematic uncertainties, and unconstrained parameters for each (N_{jet},H_T) category, which measure the ratios between corrected data counts $N^{\rm QCD}_{\rm correct}\left(N_{jet}, H_T\right)$ and QCD simulation in the sideband. Three independent corrections are combined to give the weighted mean:

$$R_{\text{mean}}\left(N_{jet}, H_T\right) = \sum_{i\in SB} \frac{R_i\left(N_{jet}, H_T\right)}{\sigma_i^2\left(N_{jet}, H_T\right)} \tag{8.12}$$

where $R_i\left(N_{jet}, H_T\right)$ and $\sigma_i\left(N_{jet}, H_T\right)$ are the correction and uncertainty extracted from the fit in sideband i. The weighted mean is applied to the QCD prediction from simulation in each (N_{jet},H_T) category separately to obtain the QCD multijet background prediction in the signal region.

Figure 8.17 shows the QCD multijet predictions in each (N_{jet}, H_T) category. Figure 8.18 shows the ratios of QCD multijet and electroweak background predictions in each (N_{jet},H_T) category, and shows that the contribution from QCD background is at sub-percent level compared to electroweak background.

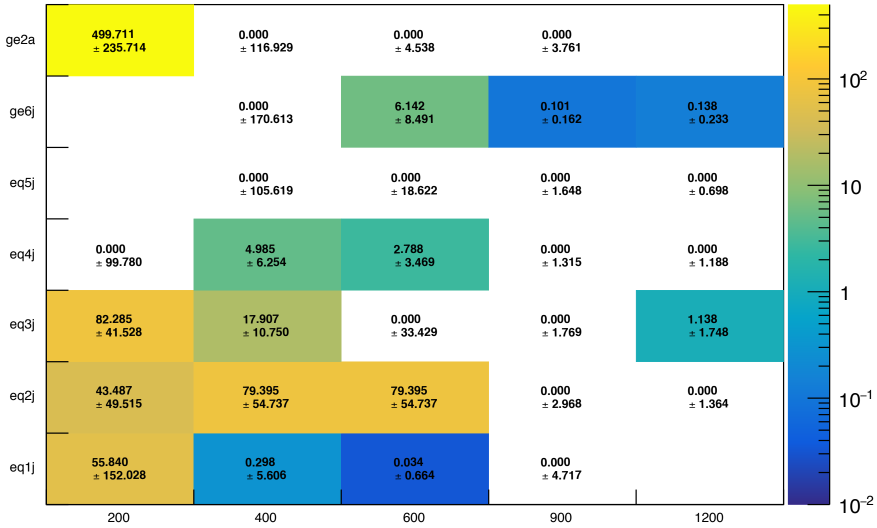

	200	400	600	900	1200
ge2a	499.711 ± 235.714	0.000 ± 116.929	0.000 ± 4.538	0.000 ± 3.761	
ge6j		0.000 ± 170.613	6.142 ± 8.491	0.101 ± 0.162	0.138 ± 0.233
eq5j		0.000 ± 105.619	0.000 ± 18.622	0.000 ± 1.648	0.000 ± 0.698
eq4j	0.000 ± 99.780	4.985 ± 6.254	2.788 ± 3.469	0.000 ± 1.315	0.000 ± 1.188
eq3j	82.285 ± 41.528	17.907 ± 10.750	0.000 ± 33.429	0.000 ± 1.769	1.138 ± 1.748
eq2j	43.487 ± 49.515	79.395 ± 54.737	79.395 ± 54.737	0.000 ± 2.968	0.000 ± 1.364
eq1j	55.840 ± 152.028	0.298 ± 5.606	0.034 ± 0.664	0.000 ± 4.717	

Figure 8.17.: Predicted QCD multijet counts in each (N_{jet},H_T) category

8.3.3. Validation and systematic uncertainty

The QCD multijet prediction utilized three independent sidebands to derive data-driven estimates. The assumption of consistency between the three sidebands is

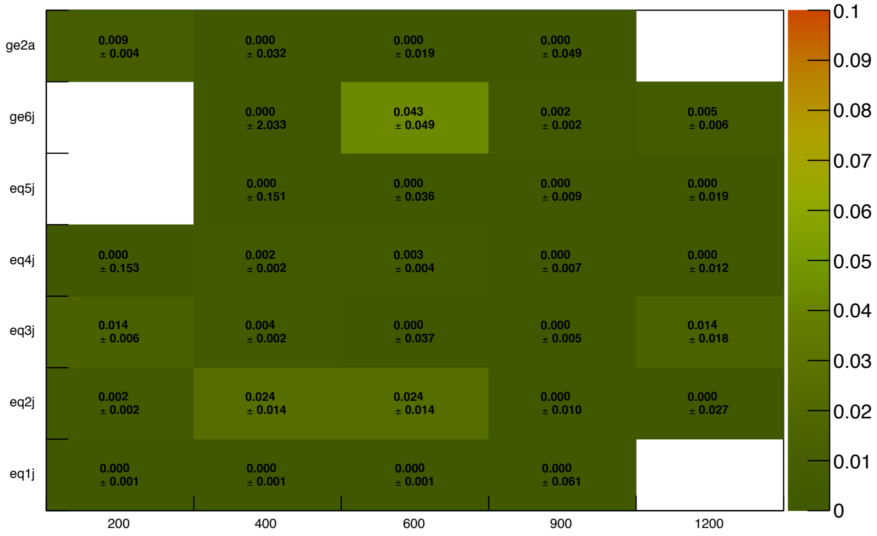

Figure 8.18.: Ratios of QCD multijet to the electroweak background predictions in each (N_{jet},H_T) category

validated by comparing the measurement and corresponding uncertainty of R_i for each sideband. Figure 8.19 and Figure 8.20 shows the ratios of R_i parameters from the $\not{H}_T/\not{E}_T$ sideband to the Double sideband and that from the $\Delta\phi^*_{\text{min}}$ sideband to the Double sideband respectively. Given the level of agreement, a systematic uncertainty of 100% is included on the QCD prediction on each (N_{jet}, H_T) category.

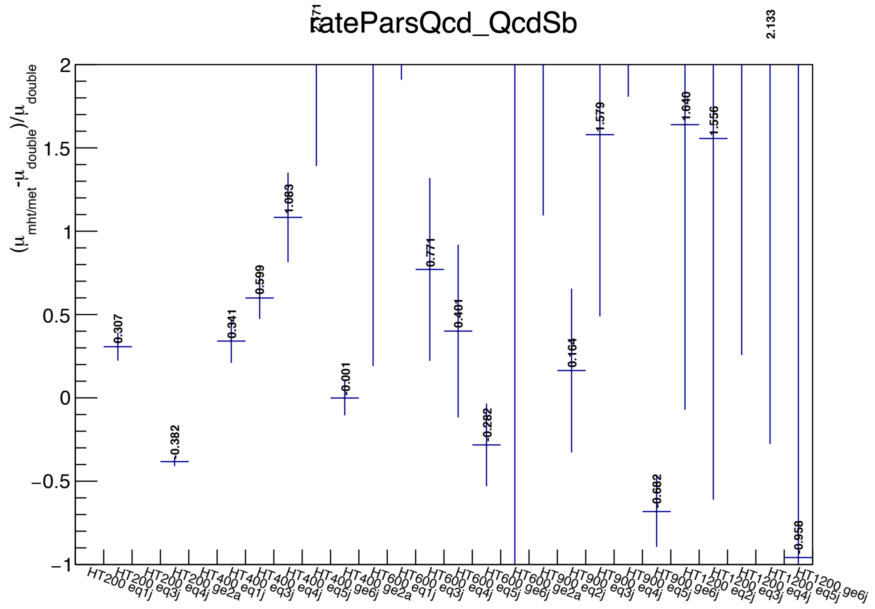

Figure 8.19.: R_B / R_A in each (N_{jet},H_T) category

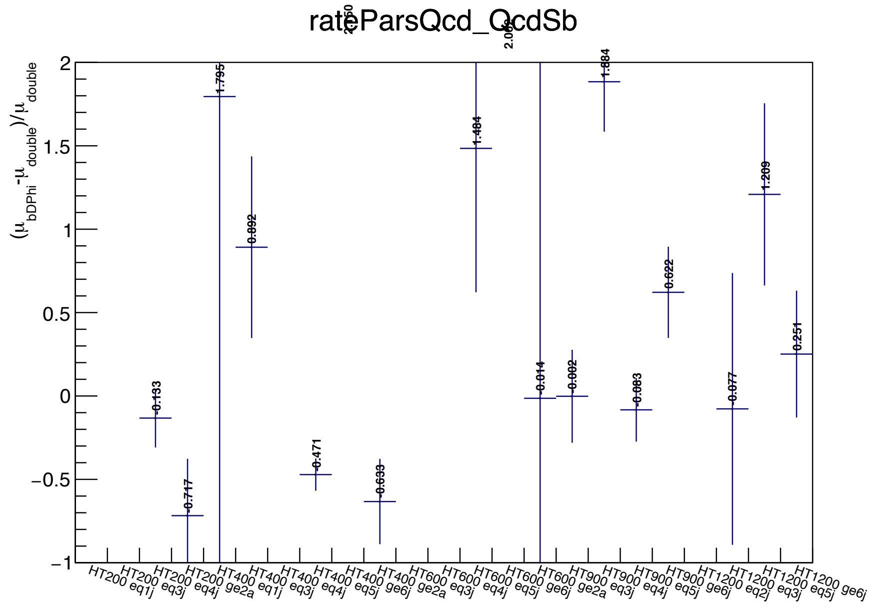

Figure 8.20.: R_C / R_A in each (N_{jet},H_T) category

Chapter 9.

Results and interpretation

9.1. Likelihood model

The likelihood model is designed such that normalizations of each category of N_{jet}, N_b and H_T (abbreviated as H_T^{cat}) are predicted by multiple control regions , while the $\not{H}_T$ shape within each H_T^{cat} category is obtained from simulation. The signal (hadronic) and control components in the likelihood are connected by unconstrained parameters. For each H_T^{cat} category, j, the hadronic component is further decomposed to a product of Poisson likelihoods, each corresponding to a $\not{H}_T$ bin i ($\mathrm{Pois}(n|\lambda) \equiv e^{-n}\frac{\lambda^n}{n!}$):

$$
\begin{aligned}
\mathcal{L}^{j}_{\mathrm{had}} = \prod_i \mathcal{L}^{j,i}_{\mathrm{had}} = \prod_i \mathrm{Pois}(n^{j,i}_{\mathrm{had}} |\, & b^{j,i}_{\mathrm{Z_{inv},had}} \times \phi^{j}(\mu\mu \to \mathrm{Z_{inv}}) \times a^{j}_{\mathrm{Z_{inv}}} \times \rho^{j,i}_{\mathrm{Z_{inv},had}} + \\
& b^{j,i}_{\mathrm{t\bar{t}W,had}} \times \phi^{j}(\mu \to \mathrm{t\bar{t}W}) \times a^{j}_{\mathrm{t\bar{t}W}} \times \rho^{j,i}_{\mathrm{t\bar{t}W,had}} + \\
& b^{j,i}_{\mathrm{QCD,had}} \times \omega^{j,i}_{\mathrm{QCD,had}} + \\
& r \times s^{j,i}_{\mathrm{had}} \times \rho^{j,i}_{s,\mathrm{had}})
\end{aligned}
\tag{9.1}
$$

where $b^{j,i}_{\mathrm{Z}^{/}_{\mathrm{inv}}\mathrm{t\bar{t}W,had}}$ are the prediction from simulation for various electroweak backgrounds; $b^{j,i}_{\mathrm{QCD,had}}$ are the prediction for the QCD multijet component; the a^j parameter links the prediction of the signal components to the control components;

ϕ^j represents systematic uncertainties on the transfer factors from the data-driven tests; ρ^j contains the systematics on simulations, including systematic variations in simulation, systematics on the $\not{H}_T$ shape and statistic uncertainties from the finite size of simulated samples. r is the parameter of interest 'signal strength'. $\omega_{\mathrm{QCD,had}}$ contains the uncertainties on the QCD multijet component.

The likelihood component for the $\mu +$ jets control region is written as:

$$\mathcal{L}^j_\mu = \mathrm{Pois}(n^j_\mu |\, b^j_\mu \times a^j_{\mathrm{t\bar{t}W}} \times \rho^j_\mu + b^j_{\mathrm{QCD},\,\mu} + r \times s^j_\mu \times \rho^j_{s,\mu}) \tag{9.2}$$

where the s^j_μ is the signal contamination in the control region, ρ^j_μ represents the systematic uncertainty from variations in simulation. Similarly, The unconstrained $a^j_{\mathrm{t\bar{t}W}}$ parameter connects the $\mu +$ jets and signal region, and the QCD component, $b^j_{\mathrm{QCD},\,\mu}$, is predicted with simulation.

The $Z_{\mathrm{i}nv}$ component in the signal region is predicted using the $\mu\mu +$ jets regions. Likewise, the likelihood component for $\mu\mu +$ jets control region is written as:

$$\mathcal{L}^j_{\mu\mu} = \mathrm{Pois}(n^j_{\mu\mu} |\, b^j_{\mu\mu} \times a^j_{Z_{\mathrm{i}nv}} \times \rho^j_{\mu\mu} + b^j_{\mathrm{QCD},\,\mu\mu} + r \times s^j_{\mu\mu} \times \rho^j_{s,\mu\mu}) \tag{9.3}$$

Category j here is slightly different from the signal region and $\mu +$ jets control region as the categorization is defined as (N_{jet},H_T,$N_b = 0$) or (N_{jet},H_T,$N_b \geq 1$). One single parameter $a^j_{Z_{\mathrm{i}nv}}$ per each (N_{jet},H_T) category is shared in the corresponding signal region category and $\mu\mu +$ jets control region in case of $N_b \geq 1$.

The modifier (a, ρ, ϕ, ω) and constraint terms (π_k in Equation 9.4) are detailed as follows:

- Systematic uncertainties on the transfer factors and QCD multijet contribution are implemented as 'log normal' uncertainties, which the logarithm of the variable has a prior constraint with Gaussian probability density functions (π_k). Systematic uncertainties are divided into two types (N_{jet}-type, H_T-type). The N_{jet}-type ones are correlated over the H_T dimension and vice versa, as described in Section 8.1.3.

- Systematic uncertainties from variations in simulation and $\not{H}_T$ shapes are included using 'vertical template morphing' [90]. For vertical template morphing, the interpolation of yields is defined quadratically between the $\pm 1\sigma$ variations and linearly beyond this range, with a Gaussian constraint. These uncertainties from simulation and $\not{H}_T$ shapes are fully correlated and uncorrelated across all categories respectively.
- The statistical uncertainty from the formula method is derived using the method described in Section 7.2. The templates are included with vertical template morphing. The uncertainties are fully correlated in the N_b dimension but uncorrelated for each (N_{jet},H_T,$\not{H}_T$) category.

The total likelihood can be written as a product over all H_T^{cat} bins and each nuisance parameter:

$$\mathcal{L} = \prod_{j \in H_T^{cat}} \mathcal{L}^j_{\text{had}} \times \mathcal{L}^j_{\mu\mu} \times \mathcal{L}^j_{\mu} \times \prod_{k \in \text{nuis}} \pi_k \tag{9.4}$$

9.2. Results of the maximum likelihood fit to data

To extract the SM prediction, two simultaneous fits with the SM-only hypothesis are performed, namely control-region-only fit and full fit. The control-region-only fit uses data from control region only while the full fit uses data from the signal and control regions.

Figure 9.1-9.3, ordered by jet category in N_{jet}, show observed data counts, SM prediction and corresponding uncertainties for each category from the control-region-only fit. Figure 9.4-9.6 show results from the full fit including the signal region. Good agreement is observed between the control-region-only and full fit.

Figure 9.7 shows the 1D and 2D pull distribution with each (N_{jet}, H_T, N_b) category from the control-region-only fit, with pull defined as the ratio of data count minus the central value of the prediction divided by the quadrature sum of Poisson statistical uncertainty from data and post-fit uncertainty from the control-region-

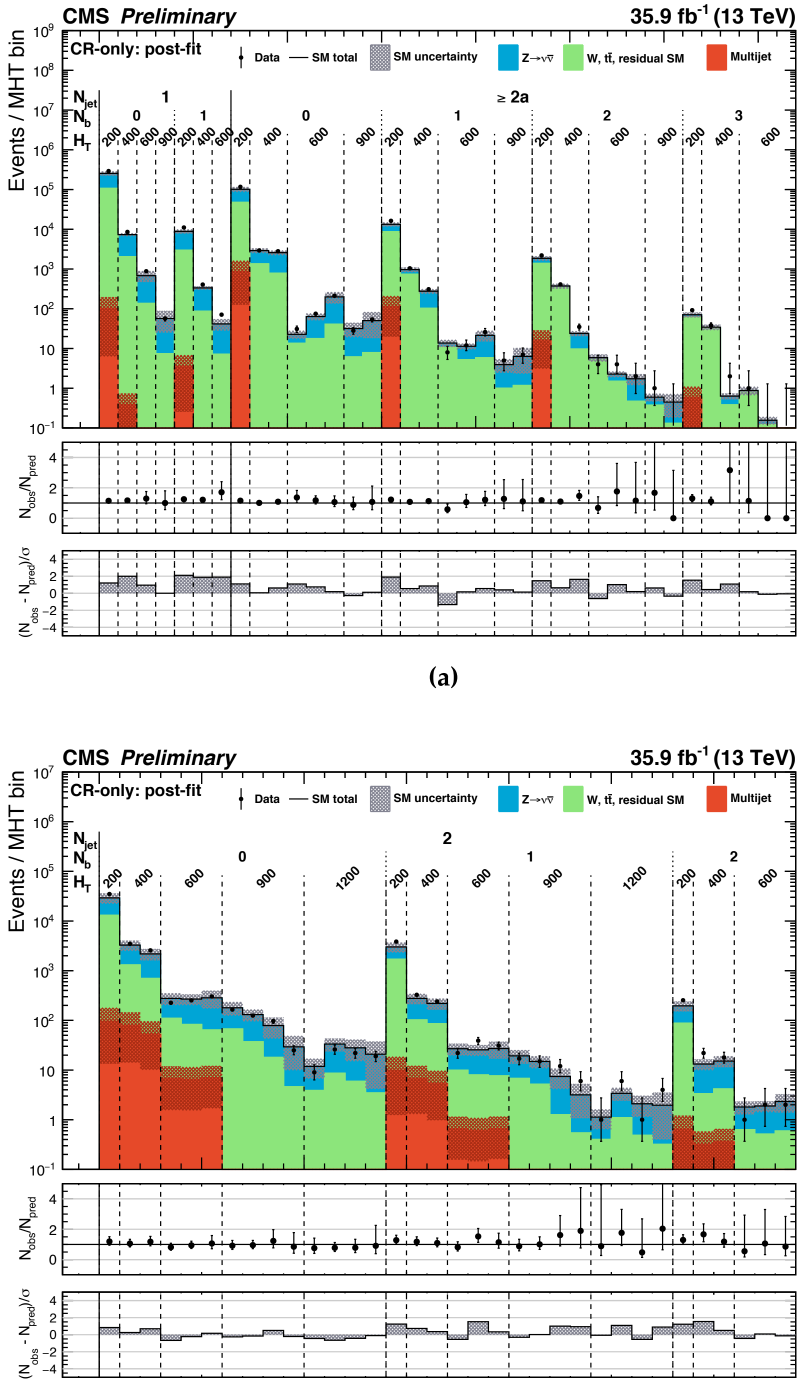

(a)

(b)

Figure 9.1.: CR-only fit in monojet, asymmetric (9.1a) and dijet topology (9.1b)

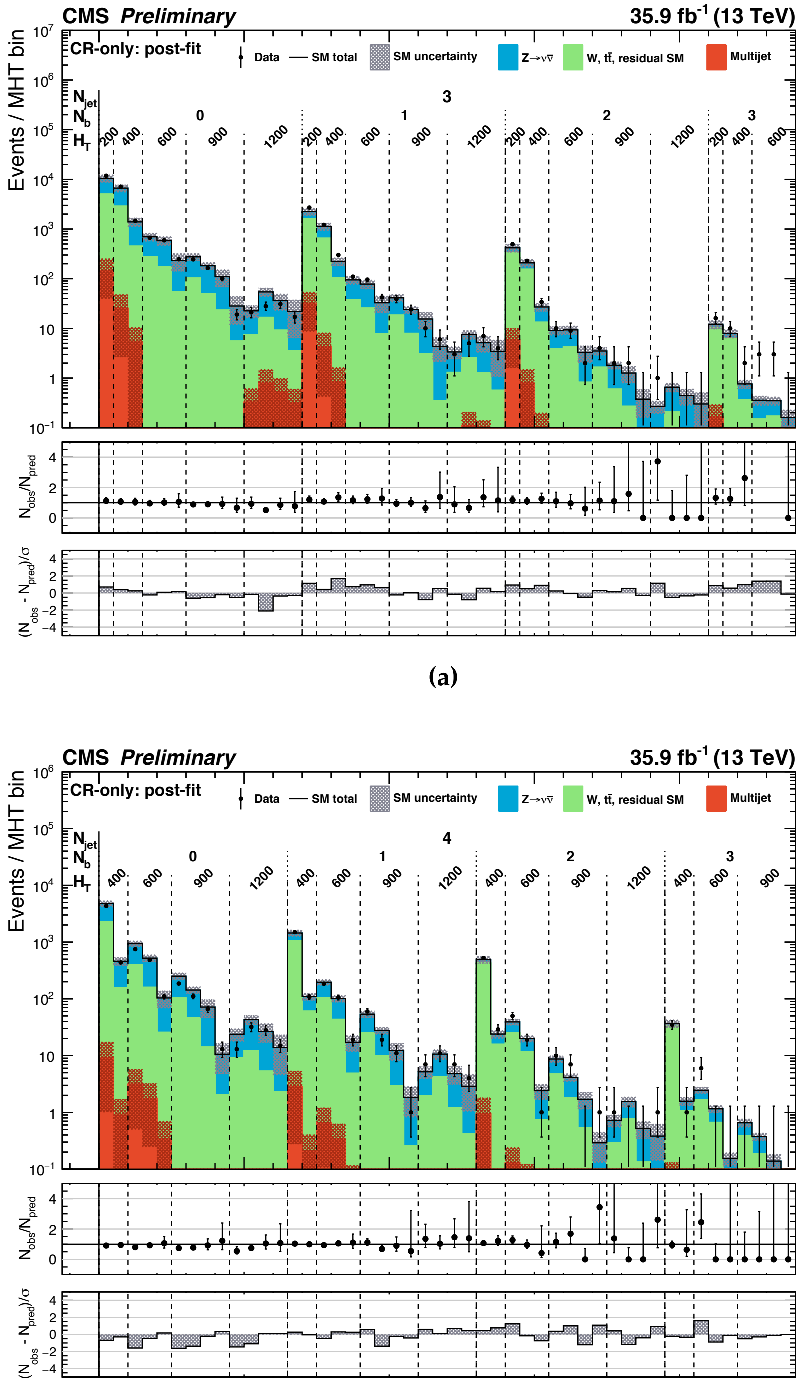

(a)

(b)

Figure 9.2.: CR-only fit in topology with 3 jets (9.2b) and 4 jets (9.2b)

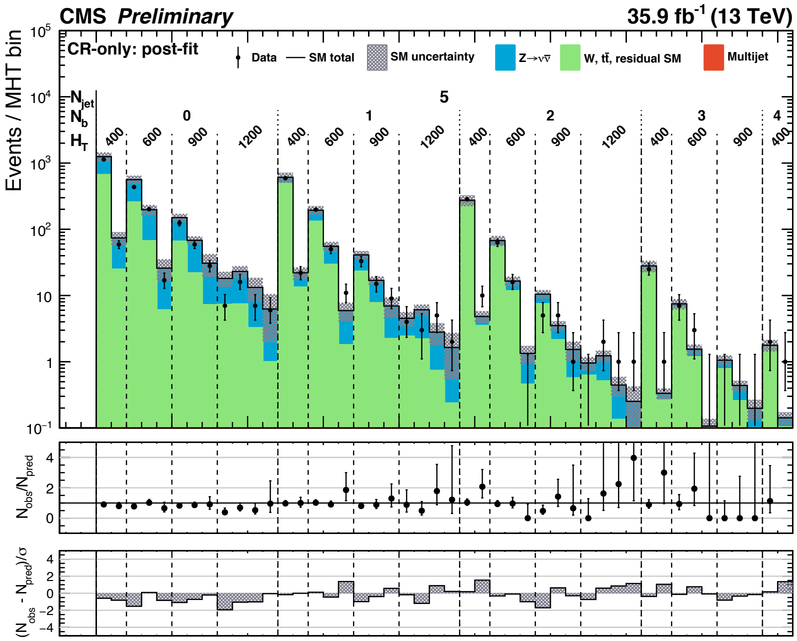

(a)

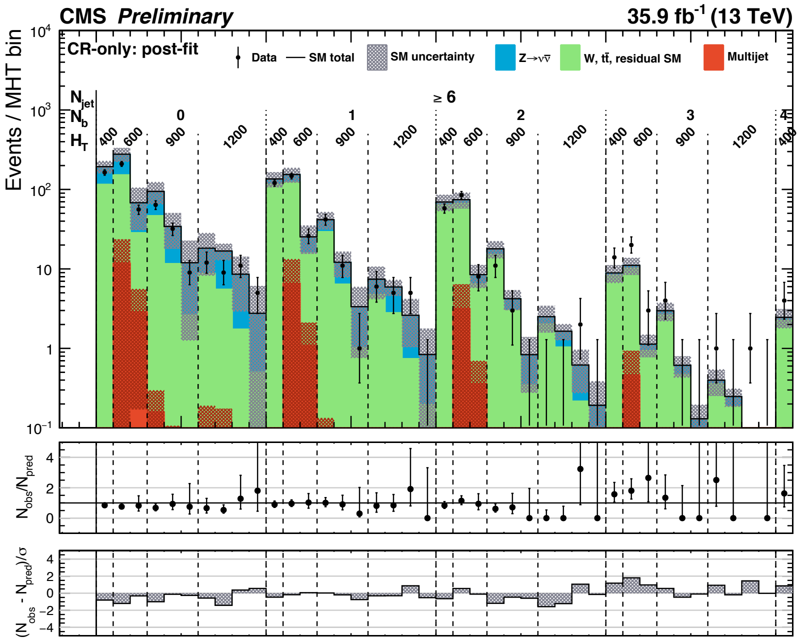

(b)

Figure 9.3.: CR-only fit in topology with 5 jets (9.3a) and ≥ 6 jets (9.3b)

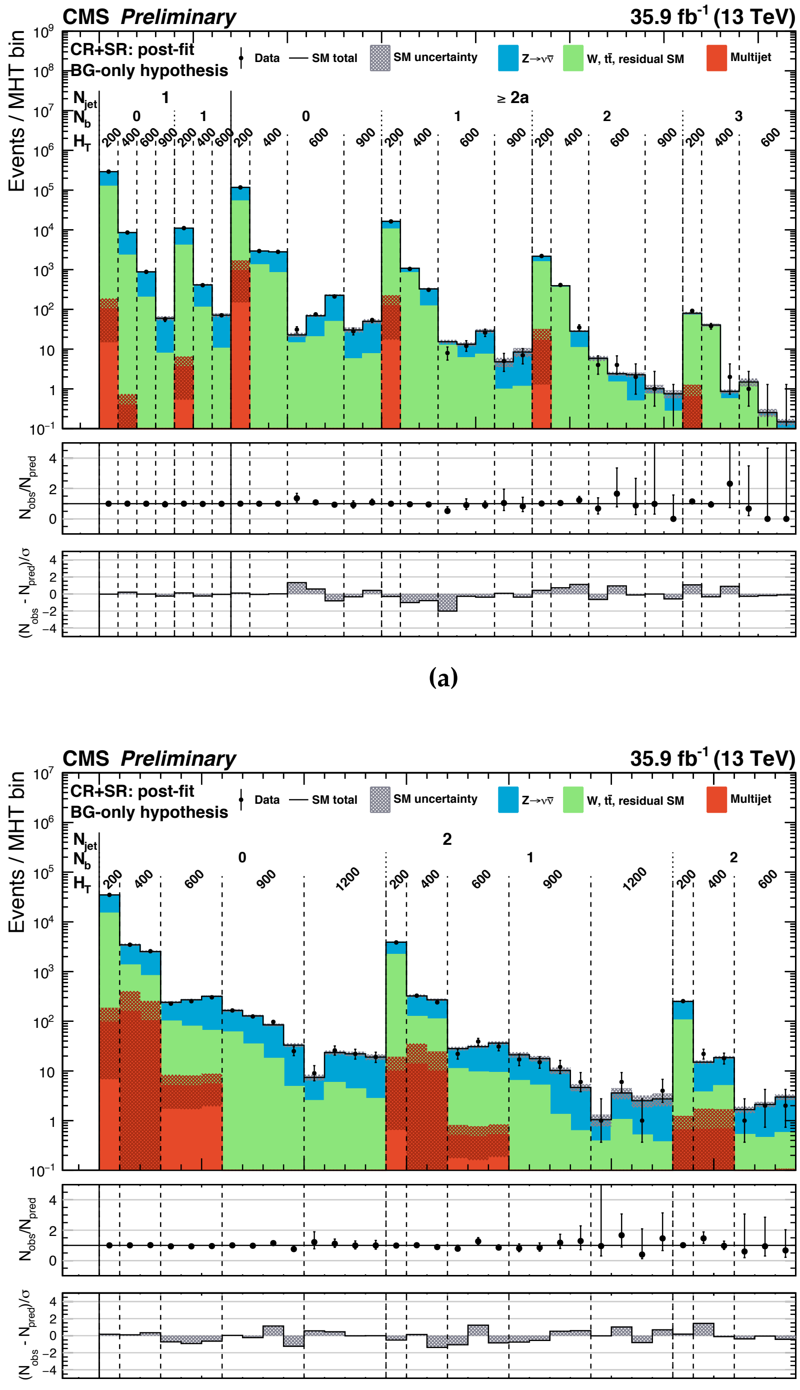

(a)

(b)

Figure 9.4.: Full fit in monojet, asymmetric (9.4a) and dijet topology (9.4b)

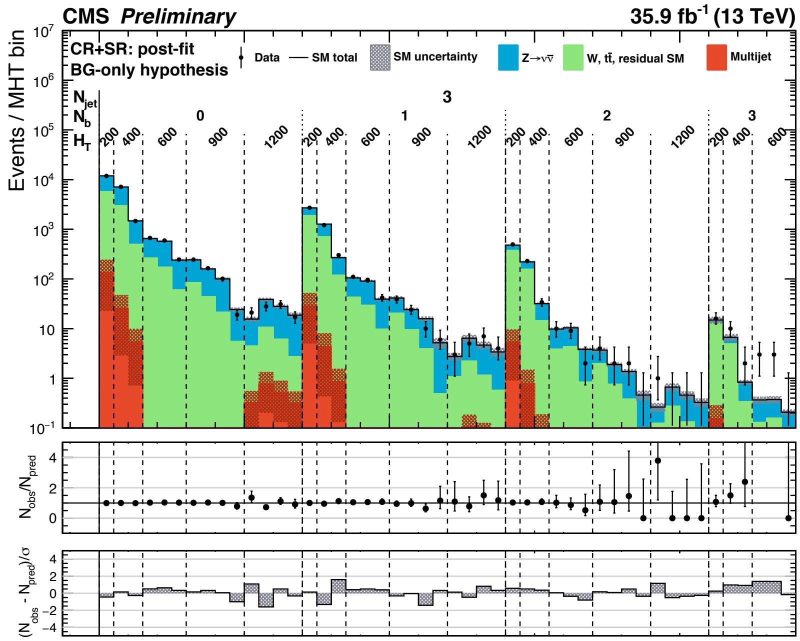

(a)

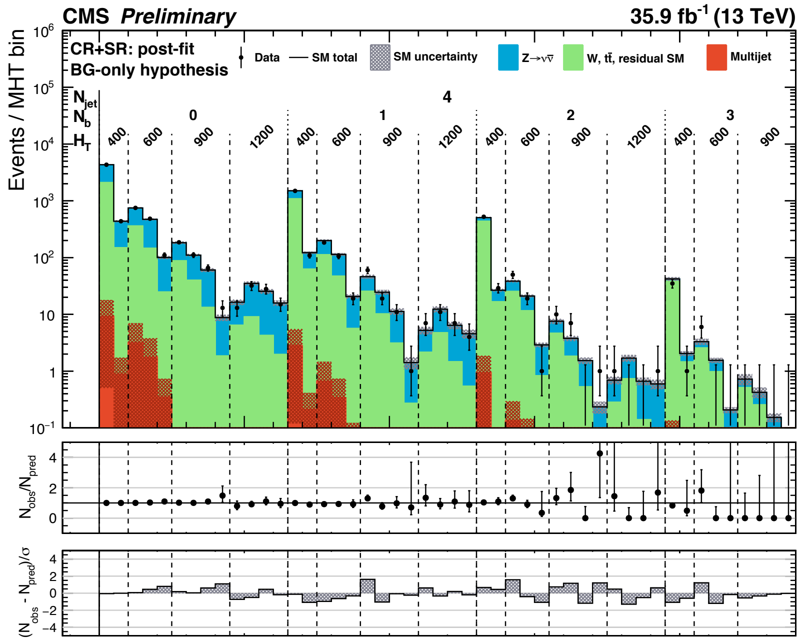

(b)

Figure 9.5.: Full fit in topology with 3 jets (9.5a) and 4 jets (9.5b)

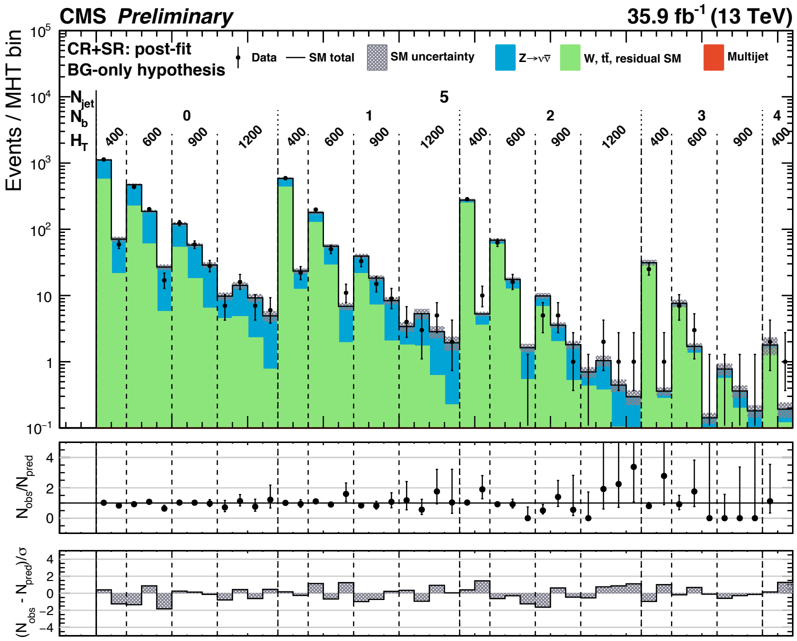

(a)

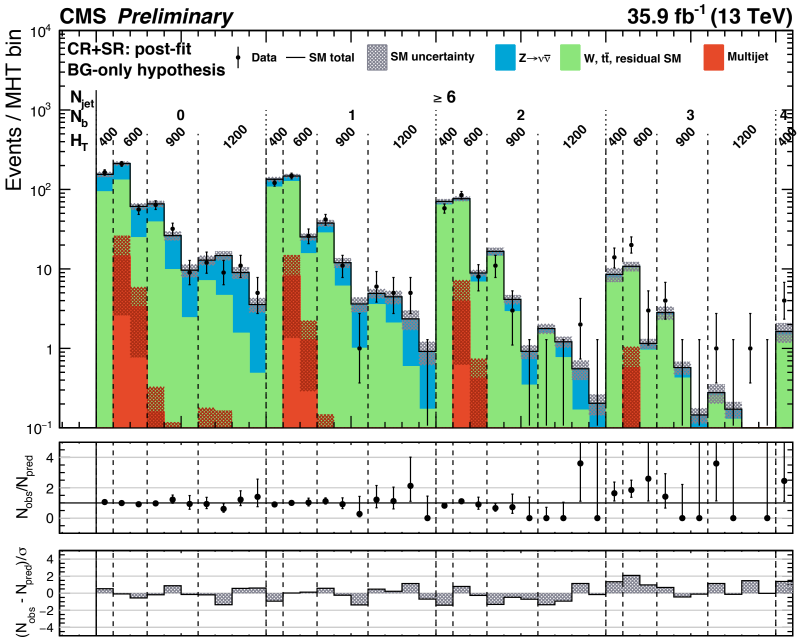

(b)

Figure 9.6.: Full fit in topology with 5 jets (9.6a) and $\geq$ 6 jets (9.6b)

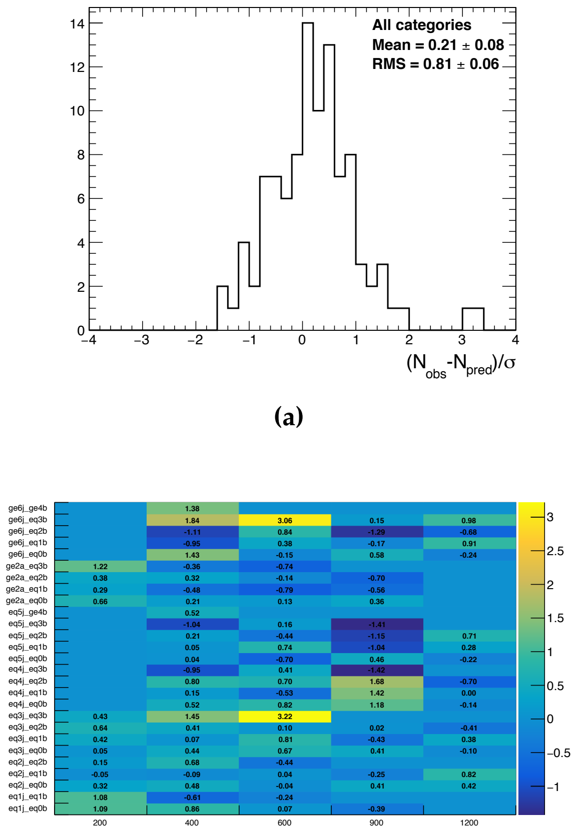

	200	400	600	900	1200
ge6j_ge4b		1.38			
ge6j_eq3b		1.84	3.06	0.15	0.98
ge6j_eq2b		-1.11	0.84	-1.29	-0.68
ge6j_eq1b		-0.95	0.38	-0.17	0.91
ge6j_eq0b		1.43	-0.15	0.58	-0.24
ge2a_eq3b	1.22	-0.36	-0.74		
ge2a_eq2b	0.38	0.32	-0.14	-0.70	
ge2a_eq1b	0.29	-0.48	-0.79	-0.56	
ge2a_eq0b	0.66	0.21	0.13	0.36	
eq5j_ge4b		0.52			
eq5j_eq3b		-1.04	0.16	-1.41	
eq5j_eq2b		0.21	-0.44	-1.15	0.71
eq5j_eq1b		0.05	0.74	-1.04	0.28
eq5j_eq0b		0.04	-0.70	0.46	-0.22
eq4j_eq3b		-0.95	0.41	-1.42	
eq4j_eq2b		0.80	0.70	1.68	-0.70
eq4j_eq1b		0.15	-0.53	1.42	0.00
eq4j_eq0b		0.52	0.82	1.18	-0.14
eq3j_eq3b	0.43	1.45	3.22		
eq3j_eq2b	0.64	0.41	0.10	0.02	-0.41
eq3j_eq1b	0.42	0.07	0.81	-0.43	0.38
eq3j_eq0b	0.05	0.44	0.67	0.41	-0.10
eq2j_eq2b	0.15	0.68	-0.44		
eq2j_eq1b	-0.05	-0.09	0.04	-0.25	0.82
eq2j_eq0b	0.32	0.48	-0.04	0.41	0.42
eq1j_eq1b	1.08	-0.61	-0.24		
eq1j_eq0b	1.09	0.86	0.07	-0.39	

(a)

(b)

Figure 9.7.: Distribution of the significance of the deviations (pulls) observed in data with respect to the SM expectations across all (N_{jet}, H_T, N_b) category displayed as a 1D distribution (9.7a) and a 2D plane (9.7b). The x-axis (y-axis) represents each H_T (N_{jet},N_b) category and the z-axis encodes the pull.

only fit. Pulls represent the level of tension between the data and prediction in the signal region. Figure 9.7a shows that an overall over-estimation of $\sim 0.21\sigma$ is observed across all (N_{jet},N_b,H_T) categories and hence no significant deviation is observed between data and SM predictions. Figure 9.7b shows that no localized biases are observed with particular group of jet or H_T categories. Two categories with pull $> 3\sigma$ are observed. They are caused by the localized upward fluctuation of data in the signal region in each of the two category. No significant data excess is observed in adjacent bins with similar jet topology and kinematics.

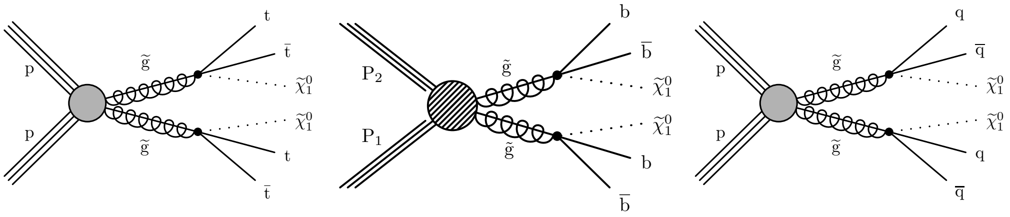

(a) T1tttt **(b)** T1bbbb **(c)** T1qqqq

Figure 9.8.: Feynman diagram of simplified models for gluino pair production.

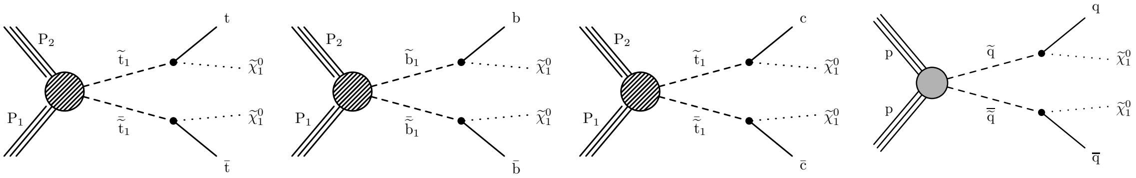

(a) T2tt **(b)** T2bb **(c)** T2cc **(d)** T2qq

Figure 9.9.: Feynman diagram of simplified models for squark pair production.

9.3. Interpretation

No significant excess is observed in the data when compared to the SM background, limits are set on parameters of SUSY models. Simplified models discussed in Section 2.3.3 are used for interpretation of the results. Models are named according to their production mechanism. Gluino pair produced models are prefixed with T1 while squark pair produced models with T2. Three decay channels of the T1-type production are considered, as shown in Figure 9.8. Corresponding models with T2-type production are shown in Figure 9.9. For T2qq models, two different mass mass spectra are considered: a mass spectrum with $\tilde{u}$, $\tilde{d}$, $\tilde{s}$ and $\tilde{c}$ degenerate in mass (eight-fold) and a mass spectrum without such degeneracy (one-fold).

Table 9.1 shows the SUSY models, corresponding production mechanisms and decays considered in the analysis.

Model	Production	Decay	Exclusion plane
T1qqqq	$\mathrm{pp} \rightarrow \tilde{\mathrm{g}}\tilde{\mathrm{g}}^*$	$\tilde{\mathrm{g}} \rightarrow \bar{\mathrm{q}}\mathrm{q}\chi^0$	Figure 9.10c
T1bbbb	$\mathrm{pp} \rightarrow \tilde{\mathrm{g}}\tilde{\mathrm{g}}^*$	$\tilde{\mathrm{g}} \rightarrow \bar{\mathrm{b}}\mathrm{b}\chi^0$	Figure 9.10a
T1tttt	$\mathrm{pp} \rightarrow \tilde{\mathrm{g}}\tilde{\mathrm{g}}^*$	$\tilde{\mathrm{g}} \rightarrow \bar{\mathrm{t}}\mathrm{t}\chi^0$	Figure 9.10b
T2qq (1-fold)	$\mathrm{pp} \rightarrow \tilde{\mathrm{q}}\tilde{\mathrm{q}}^*$	$\tilde{\mathrm{q}} \rightarrow \mathrm{q}\chi^0$	Figure 9.11a
T2qq (8-fold)	$\mathrm{pp} \rightarrow \tilde{\mathrm{q}}\tilde{\mathrm{q}}^*$	$\tilde{\mathrm{q}} \rightarrow \mathrm{q}\chi^0$	Figure 9.11a
T2bb	$\mathrm{pp} \rightarrow \tilde{\mathrm{b}}\tilde{\mathrm{b}}^*$	$\tilde{\mathrm{b}} \rightarrow \mathrm{b}\chi^0$	Figure 9.11c
T2tt	$\mathrm{pp} \rightarrow \tilde{\mathrm{t}}\tilde{\mathrm{t}}^*$	$\tilde{\mathrm{t}} \rightarrow \mathrm{t}\chi^0$	Figure 9.11d
T2cc	$\mathrm{pp} \rightarrow \tilde{\mathrm{t}}\tilde{\mathrm{t}}^*$	$\tilde{\mathrm{t}} \rightarrow \mathrm{c}\chi^0$	Figure 9.11b

Table 9.1.: A summary of simplified models used in the analysis.

9.3.1. Systematic uncertainties on signal models

Sources of theoretical and experimental systematic uncertainty are propagated to the MC simulation of signal models with vertical template morphing in the likelihood model, as described in Section 9.1. Most of the uncertainties are determined in the same way as those for background estimation and evaluated separately for each SUSY model. A systematic of 2.6% on the integrated luminosity is included as the signal model yields are determined from simulation. A summary of uncertainties for each SUSY model with representative mass parameters are shown in Table 9.2.

9.3.2. Statistical procedure for deriving limits

The limit setting procedure is performed for each signal model with a particular set of mass points. Using the likelihood defined in Section 9.1, the profile likelihood ratio can be defined as

$$\lambda(r) = \frac{\mathcal{L}(r, \hat{\boldsymbol{\theta}}(r))}{\mathcal{L}(\hat{r}, \hat{\theta})} \tag{9.5}$$

where r is the parameter of interest, θ are the nuisance parameters, and the estimators $\hat{r}$, $\hat{\theta}$ maximize the likelihood $\mathcal{L}$, and $\hat{\boldsymbol{\theta}}(r)$ maximizes $\mathcal{L}$ for a given value of r. Nuisance parameters smear the profile likelihood function as a function of

Model	$(m_{\text{Susy}}, m_{\text{LSP}})$	Luminosity	ISR	JEC	PU	b-tag	Trigger	MC stat.
T1qqqq	(1700,100)	2.6%	2-4%	2-12%	6-12%	1-1%	1-2%	14-19%
	(1000,850)	2.6%	3-14%	5-14%	9-14%	3-7%	2-4%	6-22%
T1bbbb	(1900,100)	2.6%	3-9%	4-6%	7-14%	7-12%	4-5%	11-19%
	(1300,1100)	2.6%	2-11%	3-11%	5-9%	2-5%	1-3%	11-22%
T1tttt	(1700,100)	2.6%	2-6%	3-15%	2-9%	2-6%	2-4%	12-24%
	(950,600)	2.6%	5-9%	12-26%	7-13%	2-6%	3-7%	15-30%
T2qq (1-fold)	(700,100)	2.6%	2-7%	3-10%	6-9%	0-5%	1-4%	4-22%
	(400,300)	2.6%	5-22%	5-18%	9-15%	3-5%	3-5%	6-20%
T2qq (8-fold)	(1250,100)	2.6%	2-7%	5-14%	5-10%	1-1%	1-3%	12-24%
	(700,600)	2.6%	4-17%	4-13%	9-14%	2-5%	2-4%	6-22%
T2bb	(1000,100)	2.6%	1-7%	4-11%	5-9%	1-4%	0-3%	14-23%
	(550,450)	2.6%	4-15%	4-15%	8-13%	3-7%	2-3%	9-22%
T2tt	(1000,50)	2.6%	3-7%	4-14%	6-10%	1-5%	1-4%	14-27%
	(450,200)	2.6%	4-12%	6-15%	10-14%	4-9%	3-6%	6-19%
	(250,150)	2.6%	13-27%	8-22%	12-25%	6-16%	6-17%	10-23%
T2cc	(500,480)	2.6%	4-18%	5-13%	5-12%	1-4%	2-4%	6-19%

Table 9.2.: Representative range taken from the 16% and 84% percentiles of the uncertainty across the analysis bins for each source of signal systematic for each model with representative mass points $(m_{\text{Susy}}, m_{\text{LSP}})$, chosen along the -1σ exclusion of each exclusion plane.

r, reflecting a loss of sensitivity due to systematic uncertainties. Only scenarios with $r \geq 0$ are considered as the presence of new signal considered in this analysis only leads to data excess. Signals that could lead to data deficit, such as neutrino oscillation or interference, require other limit setting procedures. For the same reason, scenarios with $r < \hat{r}$ are not considered to be less compatible with the data and will not be excluded. As a consequence, the test statistic q_r can be defined as

$$q_r = \begin{cases} -2\ln\frac{\mathcal{L}(r,\hat{\boldsymbol{\theta}}(r))}{\mathcal{L}(0,\hat{\boldsymbol{\theta}}(0))}, (\hat{r} < 0) \\ -2\ln\frac{\mathcal{L}(r,\hat{\boldsymbol{\theta}}(r))}{\mathcal{L}(\hat{r},\hat{\boldsymbol{\theta}})}, (0 < \hat{r} < r) \\ 0, (\hat{r} > r) \end{cases}$$

Increasing values of q_r indicate less compatibility of the assumed value r with the observed data. The compatibility of a given signal model with a assumed value r can be quantified by the p-value, defined as

$$p_r = \int_{q_{\hat{r}}}^{\infty} f(q_r|r)dq_r \tag{9.6}$$

where $f(q_r|r)$ is the probability density function. This function can be estimated by generating pseudo-experiments or approximated by the asymptotic formulae described in [91]. In this analysis, the asymptotic formulae are used instead as it is too computing-intensive to generate pseudo-experiments for each signal model with all mass points.

The $\mathrm{CL_s}$ is defined as

$$\mathrm{CL_s}(r) = \frac{p_r}{1 - p_0} \tag{9.7}$$

where p_0 is the p-value with the background-only hypothesis ($r = 0$). The observed 95% CLs upper limit on r ($_{\mathrm{upper}}$) is defined as the value of r that gives $\mathrm{CL_S}(r) = 0.05$. The corresponding expected limit is defined as the median value (the 50% quantile) of the distribution of r_{upper}, where the distribution is obtained by generating pseudo-experiments under the background-only hypothesis and deriving an 'observed' 95% CLs upper limit on r for each of them. Similarly, the 21% (79%) quantile of the distribution are used to define $+1\sigma$ (-1σ) upper limit. The median and $+1\sigma$ expected limit are approximated by the asymptotic formulae in [91].

9.3.3. Exclusion limits

Exclusion limits are determined for each simplified model, defined with the production and decay channel and mass points. Upper limits at 95% confidence level on the cross section for each model is obtained using the $\mathrm{CL_s}$ criterion [92] and asymptotic formulae [91] to approximate the distributions of the one-sided profile likelihood ratio (test statistic) under the relevant hypothesis (background only or signal plus background).

Upper limits of gluino models (T1qqqq, T1bbbb, T1tttt) and squark models (T2qq, T2bb, T2tt, T2cc) are shown in Figure 9.10 and Figure 9.11. Each plot corresponds to a specific production mechanism and decay process and sparticle and LSP mass points are displayed in the x-axis and y-axis respectively. Theoretical cross sections for each model are calculated with NLO accuracy [93]. Observed and expected exclusion contours and the corresponding $\pm 1\sigma$ uncertainty bands are drawn. Figure 9.12 and 9.13 show a summary exclusion plane of gluino and squark mediated models respectively.

For gluino production models, models with gluino mass up to 1850 GeV and LSP up to 1100 GeV are excluded. The light squark mass is excluded up to 1350 GeV (700 GeV) with LSP mass up to 650 GeV (400 GeV) for the eight-fold (one-fold) degenerate T2qq model. The sbottom mass is excluded up to 1075 GeV with LSP mass up to 550 GeV. The stop mass is excluded up to 1075 GeV with LSP mass up to 400 GeV.

For large mass splittings between various sparticle (gluino, squark, sbottom or stop) and LSP, i.e. high sparticle and low LSP mass, signal counts generally reside in the highest H_T and $\not{H}_T$ bins, in which predictions are limited by statistical uncertainties of data and MC simulation. Limits here are not sensitive to various systematic uncertainties in the analysis. On the other hand, limits for small or intermediate mass splittings between sparticle and LSP are affected by systematic uncertainties in the analysis and are weakened when moving towards the diagonal line where kinematic acceptance of visible decay products from the sparticles are limited.

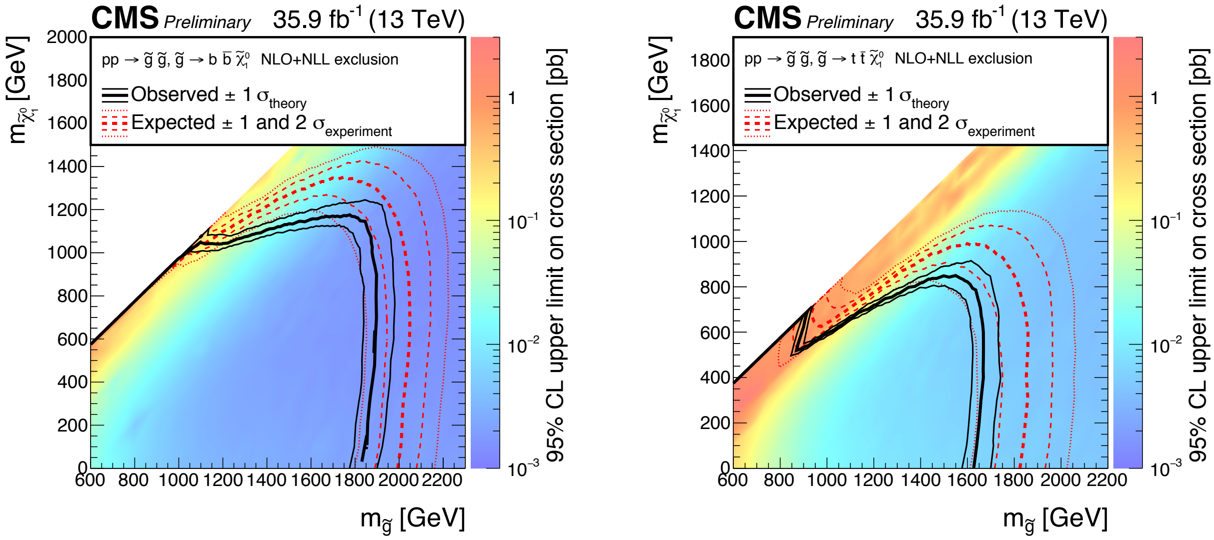

(a) T1bbbb

(b) T1tttt

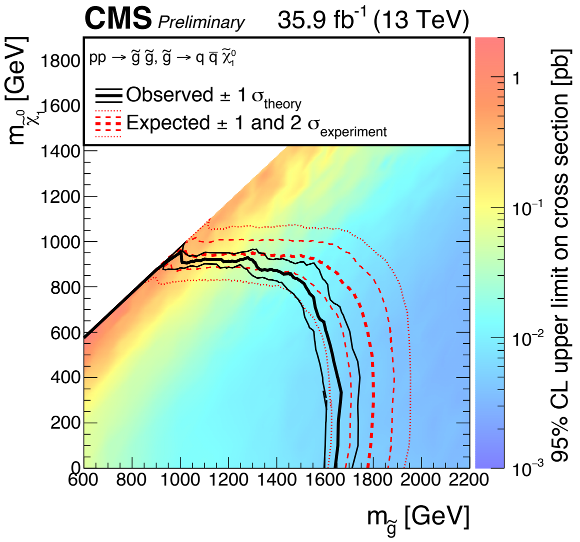

(c) T1qqqq

Figure 9.10.: 95% C.L. observed upper limit on the cross section for gluino models (histogram), with the expected (solid black line) observed (solid red line) exclusion contours.

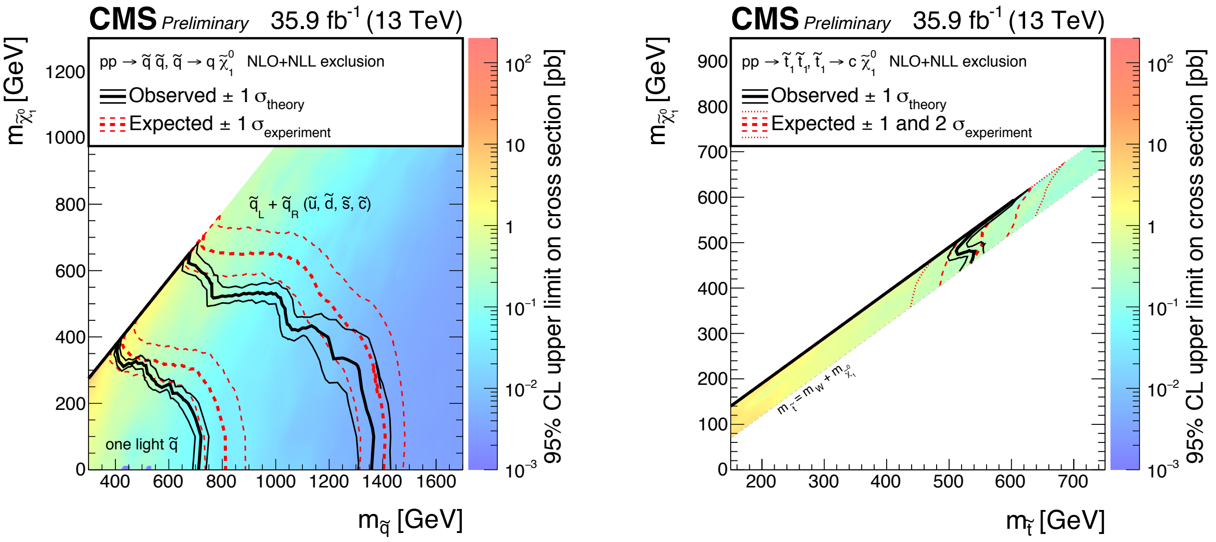

(a) T2qq

(b) T2cc

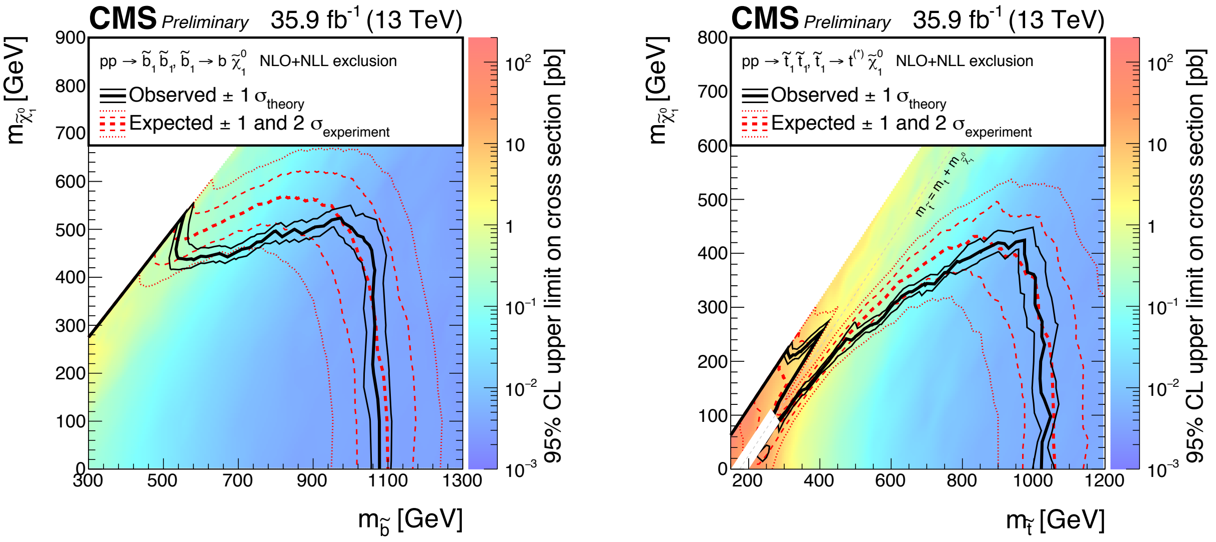

(c) T2bb

(d) T2tt

Figure 9.11.: 95% C.L. observed upper limit on the cross section for squark models (histogram), with the expected (solid black line) observed (solid red line) exclusion contours.

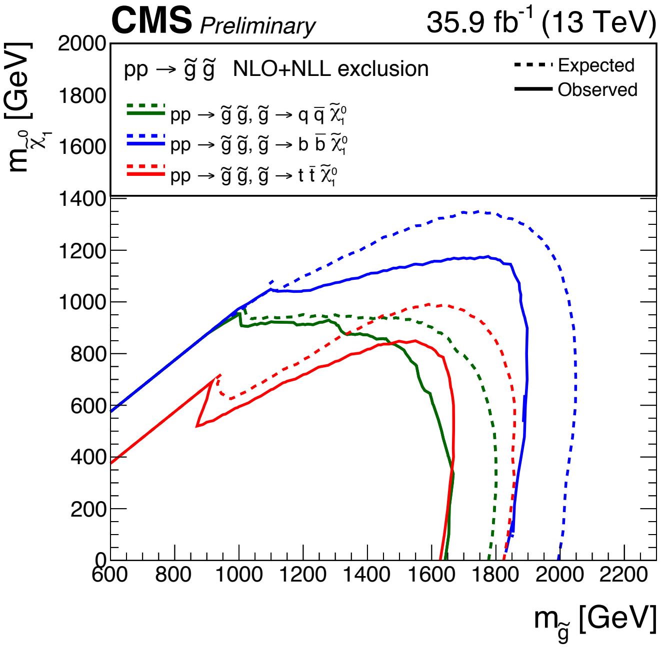

Figure 9.12.: Summary of exclusion limits for gluino-mediated models.

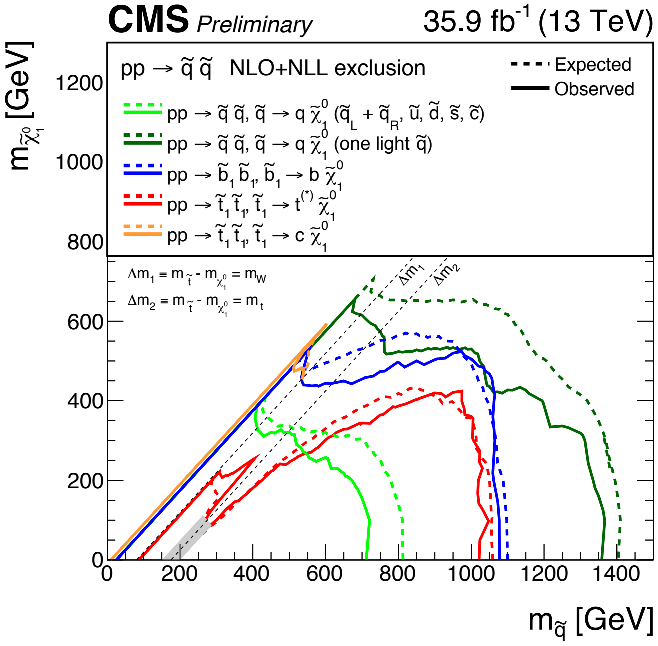

Figure 9.13.: Summary of exclusion limits for squark-mediated models.

9.3.4. Summary

The result of the α_T analysis with 35.9 fb^{-1} proton-proton data indicates no significant deviation of data from SM. CLs upper limits are derived at 95% on simplified SUSY models. The exclusion significantly exceeds beyond the reach of SUSY searches in the hadronic final state with full Run 1 datasets. In particular, an increase of up to 600 GeV (400 GeV) of exclusion in gluino (LSP) mass is achieved in gluino-mediated models. Various gains are observed with squark-mediated models, depending on each specific final state signatures. Similar results are also observed with other hadronic analyses in ATLAS and CMS [94–97].

Chapter 10.

Conclusion

A search for supersymmetry in the hadronic channel, with one or more jets and missing transverse momentum, on proton-proton collisions at $\sqrt{s} = 13$ TeV is reported. The data, corresponding to an integrated luminosity of 35.9 fb^{-1}, were collected with the CMS detector at the LHC in 2016. No evidence of BSM physics is observed. The results are interpreted with simplified gluino-mediated and squark-mediated models. The masses of bottom, top and light flavor squarks are excluded up to 1050 GeV, 1000 GeV and 1300 GeV. The gluino mass is excluded up to 1900 GeV .

The search uses two dedicated variables, the α_T and $\Delta\phi^*_{\text{min}}$ variable, to suppress QCD multijet background to a negligible level. Residual electroweak and QCD multijet backgrounds are estimated data-driven techniques with two control regions. The analysis also maintains a low H_T and $\not{H}_T$ threshold to ensure the inclusiveness and good sensitivity to a wide sensitivity of BSM models.

Previous iterations of the search have been performed on datasets at $\sqrt{s} =$ 8 TeV [98–100] and 2.3 fb^{-1} at $\sqrt{s} = 13$ TeV in 2015 [101]. The search has been updated with the dataset collected in 2016. In particular, the addition of the b-tag formula method reduces the statistical uncertainty in MC simulation and significantly increases the sensitivity of the analysis to a wide range of BSM models with high b-jet multiplicity.

The current experimental limits on gluino and squarks masses imply a significant degree of fine-tuning in various MSSM models [102]. The motivation of a natural weak-scale SUSY theory that could be explored by the LHC has significantly reduced. On the other hand, the naturalness is not the only guiding principle for BSM searches. Alternative models such as split SUSY relax the assumption on naturalness [103] but still realize other appealing features such as offering a dark matter candidate and gauge coupling unification [104]. Experimental signatures often involves long-lived particle signatures and detailed studies of the interaction of these particles and the detector are required [105]. In addition, the observation of the Higgs boson [4,5] also provides a possible new tool to explore unique signatures to BSM physics and the electroweak sector [106–108].

The LHC will continue to deliver data up to a total integrated luminosity of 3000 fb^{-1}. The possibility of uncovering signatures of BSM physics requires exploiting this large dataset with targeted analysis strategies and innovative experimental techniques, e.g. new types of signatures, advanced machine learning algorithms or comprehensive detector upgrades. At the same time, precise measurements on SM physics could also provide hints to potential BSM signatures. Measurements on the properties of the Higgs boson and other electroweak processes are pivotal to complete the understanding of physics at the electroweak scale, and provide possible directions to collider physics.

Bibliography

[1] F.Abe et al. (CDF Collaboration), "Observation of Top Quark Production in pp̄ Collisions with the Collider Detector at Fermilab", *Phys. Rev. Lett.* **74** (1995), no. 2626,.

[2] S. Abachi et al. (D0 Collaboration), "Observation of the Top Quark Production", *Phys. Rev. Lett.* **74** (1995), no. 2632,.

[3] K. Kodama et al. (DONUT Collaboration), "Observation of Tau Neutrinos Interactions", *Phys. Lett. B* **504** (2001) 218–224.

[4] G. Aad et al., "Observation of a new particle in the search for the Standard Model Higgs boson with the ATLAS detector at the LHC", *Phys. Lett.* **B716** (2012) 1–29.

[5] CMS Collaboration, "Observation of a new boson at a mass of 125 GeV with the CMS experiment at the LHC", *Phys. Lett.* **B716** (2012) 30–61, `doi:10.1016/j.physletb.2012.08.021`, `arXiv:1207.7235`.

[6] J. H. Oort, "The force exerted by the stellar system in the direction perpendicular to the galactic plane and some related problems", *Bull. Astron. Inst. Netherlands* **6** (1932) 249–287.

[7] M. Markevitch, A. H. Gonzalez, D. Clowe et al., "Direct constraints on the dark matter self-interaction cross-section from the merging galaxy cluster 1E0657-56", *Astrophys. J.* **606** (2004) 819–824, `doi:10.1086/383178`, `arXiv:astro-ph/0309303`.

[8] Planck Collaboration, "Planck 2015 results. XIII. Cosmological parameters", *Astron. Astrophys.* **594** (2016) A13, `doi:10.1051/0004-6361/201525830`, `arXiv:1502.01589`.

[9] Particle Data Group Collaboration, “Review of Particle Physics”, *Chin. Phys.* **C40** (2016), no. 10, 100001, `doi:10.1088/1674-1137/40/10/100001`.

[10] S. P. Martin, “A Supersymmetry primer”, `doi:10.1142/9789812839657_0001,10.1142/9789814307505_0001`, `arXiv:hep-ph/9709356`. [Adv. Ser. Direct. High Energy Phys.18,1(1998)].

[11] L. Evans and P. Bryant, “LHC Machine”, *JINST* **3** (2008), no. S08001,.

[12] S. Weinberg, “The Quantum theory of fields. Vol. 1: Foundations”, p. 298. Cambridge University Press, 2005.

[13] V. Barger and R. Phillips, “Collider Physics”. Frontiers in Physics. Addison-Wesley Publishing Company, 1987.

[14] D. J. Griffiths, “Introduction to elementary particles; 2nd rev. version”. Physics textbook. Wiley, New York, NY, 2008.

[15] D. J. Gross and F. Wilczek, “Ultraviolet Behavior of Nonabelian Gauge Theories”, *Phys. Rev. Lett.* **30** (1973) 1343–1346, `doi:10.1103/PhysRevLett.30.1343`.

[16] T. Muta, “Foundations of Quantum Chromodynamics: An Introduction to Perturbative Methods in Gauge Theories”. World Scientific lecture notes in physics. World Scientific, 2010.

[17] A. Salam and J. C. Ward, “Electromagnetic and weak interactions”, *Phys. Lett.* **13** (1964) 168–171, `doi:10.1016/0031-9163(64)90711-5`.

[18] S. L. Glashow, “Partial Symmetries of Weak Interactions”, *Nucl. Phys.* **22** (1961) 579–588, `doi:10.1016/0029-5582(61)90469-2`.

[19] S. Weinberg, “A Model of Leptons”, *Phys. Rev. Lett.* **19** (1967) 1264–1266, `doi:10.1103/PhysRevLett.19.1264`.

[20] F. Englert and R. Brout, “Broken Symmetry and the Mass of Gauge Vector Mesons”, *Phys. Rev. Lett.* **13** (1964) 321–323, `doi:10.1103/PhysRevLett.13.321`.

[21] P. W. Higgs, “Broken Symmetries and the Masses of Gauge Bosons”, *Phys.*

Rev. Lett. **13** (1964) 508–509, `doi:10.1103/PhysRevLett.13.508`.

[22] G. S. Guralnik, C. R. Hagen, and T. W. B. Kibble, "Global Conservation Laws and Massless Particles", *Phys. Rev. Lett.* **13** (1964) 585–587, `doi:10.1103/PhysRevLett.13.585`.

[23] C. S. Wu, E. Ambler, R. W. Hayward et al., "Experimental Test of Parity Conservation in Beta Decay", *Phys. Rev.* **105** (1957) 1413–1414, `doi:10.1103/PhysRev.105.1413`.

[24] UA1 Collaboration, "Experimental Observation of Isolated Large Transverse Energy Electrons with Associated Missing Energy at s**(1/2) = 540-GeV", *Phys. Lett.* **122B** (1983) 103–116, `doi:10.1016/0370-2693(83)91177-2`. [,611(1983)].

[25] UA1 Collaboration, "Experimental Observation of Lepton Pairs of Invariant Mass Around 95-GeV/c**2 at the CERN SPS Collider", *Phys. Lett.* **126B** (1983) 398–410, `doi:10.1016/0370-2693(83)90188-0`.

[26] UA2 Collaboration, "Evidence for Z0 —> e+ e- at the CERN anti-p p Collider", *Phys. Lett.* **129B** (1983) 130–140, `doi:10.1016/0370-2693(83)90744-X`.

[27] UA2 Collaboration, "Observation of Single Isolated Electrons of High Transverse Momentum in Events with Missing Transverse Energy at the CERN anti-p p Collider", *Phys. Lett.* **122B** (1983) 476–485, `doi:10.1016/0370-2693(83)91605-2`.

[28] J. Goldstone, A. Salam, and S. Weinberg, "Broken Symmetries", *Phys. Rev.* **127** (1962) 965–970, `doi:10.1103/PhysRev.127.965`.

[29] M. Peskin and D. Schroeder, "An Introduction to Quantum Field Theory". Advanced book classics. Avalon Publishing, 1995.

[30] W. de Boer, "Grand unified theories and supersymmetry in particle physics and cosmology", *Prog. Part. Nucl. Phys.* **33** (1994) 201–302, `doi:10.1016/0146-6410(94)90045-0`, `arXiv:hep-ph/9402266`.

[31] M. H. Poincaré, "Sur la dynamique de l'électron", *Rendiconti del Circolo*

Matematico di Palermo (1884-1940) **21** (Dec, 1906) 129–175, `doi:10.1007/BF03013466`.

[32] Super-Kamiokande Collaboration, "Search for proton decay via $p \to e^+ \pi^0$ and $p \to \mu^+ \pi^0$ in 0.31 megaton-years exposure of the Super-Kamiokande water Cherenkov detector", *Phys. Rev.* **D95** (2017), no. 1, 012004, `doi:10.1103/PhysRevD.95.012004`, `arXiv:1610.03597`.

[33] G. Jungman, M. Kamionkowski, and K. Griest, "Supersymmetric dark matter", *Phys. Rept.* **267** (1996) 195–373, `doi:10.1016/0370-1573(95)00058-5`, `arXiv:hep-ph/9506380`.

[34] C. Csaki, "The Minimal supersymmetric standard model (MSSM)", *Mod. Phys. Lett.* **A11** (1996) 599, `doi:10.1142/S021773239600062X`, `arXiv:hep-ph/9606414`.

[35] S. Braibant, "SUSY searches at LEP", in *Proceedings, 38th Rencontres de Moriond on QCD and High-Energy Hadronic Interactions: Les Arcs, France, March 22-29, 2003.* 2003. `arXiv:hep-ex/0305058`.

[36] CDF, D0 Collaboration, "SUSY searches at the Tevatron", *EPJ Web Conf.* **28** (2012) 09006, `doi:10.1051/epjconf/20122809006`, `arXiv:1202.0712`.

[37] CMS Collaboration, "Summary of comparison plots in simplified models spectra for the 8TeV dataset", 2016.

[38] J. Alwall, P. Schuster, and N. Toro, "Simplified Models for a First Characterization of New Physics at the LHC", *Phys. Rev.* **D79** (2009) 075020, `doi:10.1103/PhysRevD.79.075020`, `arXiv:0810.3921`.

[39] LHC New Physics Working Group Collaboration, "Simplified Models for LHC New Physics Searches", *J. Phys.* **G39** (2012) 105005, `doi:10.1088/0954-3899/39/10/105005`, `arXiv:1105.2838`.

[40] P. Brogi, "Study of inelastic processes in proton-proton collisions at the LHC with the TOTEM Experiment", Master's thesis, INFN, Pisa, 2011.

[41] CMS Collaboration, "CMS physics: Technical design report",.

[42] CMS Collaboration, "Description and performance of track and

primary-vertex reconstruction with the CMS tracker", *JINST* **9** (May, 2014) P10009. 80 p, `doi:10.1088/1748-0221/9/10/P10009`.

[43] P. Adzic et al., "Energy resolution of the barrel of the CMS electromagnetic calorimeter", *JINST* **2** (2007) P04004, `doi:10.1088/1748-0221/2/04/P04004`.

[44] CMS Collaboration, "The CMS electromagnetic calorimeter project",.

[45] CMS Collaboration, "The CMS Experiment at the CERN LHC", *JINST* **3** (2008) S08004, `doi:10.1088/1748-0221/3/08/S08004`.

[46] USCMS, ECAL/HCAL Collaboration, "The CMS barrel calorimeter response to particle beams from 2-GeV/c to 350-GeV/c", *Eur. Phys. J.* **C60** (2009) 359–373, `doi:10.1140/epjc/s10052-009-0959-5,10.1140/epjc/s10052-009-1024-0`. [Erratum: Eur. Phys. J.C61,353(2009)].

[47] CMS Collaboration, "CMS Technical Design Report for the Level-1 Trigger Upgrade", Technical Report CERN-LHCC-2013-011. CMS-TDR-12, (Jun, 2013). Additional contacts: Jeffrey Spalding, Fermilab, Jeffrey.Spalding@cern.ch Didier Contardo, Universite Claude Bernard-Lyon I, didier.claude.contardo@cern.ch.

[48] CMS Collaboration, "Description and performance of track and primary-vertex reconstruction with the CMS tracker", *JINST* **9** (2014), no. 10, P10009, `doi:10.1088/1748-0221/9/10/P10009`, `arXiv:1405.6569`.

[49] R. Fruhwirth, "Application of Kalman filtering to track and vertex fitting", *Nucl. Instrum. Meth.* **A262** (1987) 444–450, `doi:10.1016/0168-9002(87)90887-4`.

[50] K. Rose, "Deterministic annealing for clustering, compression, classification, regression, and related optimization problems", *Proceedings of the IEEE* **86** (1998) 2210–2239, `doi:10.1109/5.726788`.

[51] R. Fruhwirth, W. Waltenberger, and P. Vanlaer, "Adaptive Vertex Fitting", Technical Report CMS-NOTE-2007-008, CERN, Geneva, (Mar, 2007).

[52] M. Cacciari, G. P. Salam, and G. Soyez, "The Anti-k(t) jet clustering

algorithm", *JHEP* **04** (2008) 063, `doi:10.1088/1126-6708/2008/04/063`, `arXiv:0802.1189`.

[53] M. Cacciari, G. P. Salam, and G. Soyez, "FastJet User Manual", *Eur. Phys. J.* **C72** (2012) 1896, `doi:10.1140/epjc/s10052-012-1896-2`, `arXiv:1111.6097`.

[54] CMS Collaboration, "Energy calibration and resolution of the CMS electromagnetic calorimeter in pp collisions at $\sqrt{s}$ = 7 TeV", *JINST* **8** (Jun, 2013) P09009. 51 p. Comments: Submitted to JINST.

[55] CMS Collaboration, "ECAL hit timing with Run1 and Run2 energy reconstruction in early 25ns data at 13 TeV",.

[56] CMS Collaboration, "HCAL Energy Reconstruction Performance",.

[57] CMS Collaboration, "Performance of CMS muon reconstruction in pp collision events at $\sqrt{s} = 7$ TeV", *JINST* **7** (2012) P10002, `doi:10.1088/1748-0221/7/10/P10002`, `arXiv:1206.4071`.

[58] CMS Collaboration, "Performance of Electron Reconstruction and Selection with the CMS Detector in Proton-Proton Collisions at âĹŽs = 8 TeV", *JINST* **10** (2015), no. 06, P06005, `doi:10.1088/1748-0221/10/06/P06005`, `arXiv:1502.02701`.

[59] W. Adam, R. FrÃijhwirth, A. Strandlie et al., "Reconstruction of Electrons with the Gaussian-Sum Filter in the CMS Tracker at the LHC", Technical Report CMS-NOTE-2005-001, CERN, Geneva, (Jan, 2005).

[60] F. Colecchia, "Data-driven estimation of neutral pileup particle multiplicity in high-luminosity hadron collider environments", *J. Phys. Conf. Ser.* **664** (2015), no. 7, 072013, `doi:10.1088/1742-6596/664/7/072013`, `arXiv:1511.03537`.

[61] M. Cacciari and G. P. Salam, "Pileup subtraction using jet areas", *Phys. Lett.* **B659** (2008) 119–126, `doi:10.1016/j.physletb.2007.09.077`, `arXiv:0707.1378`.

[62] G. P. Salam, "Towards Jetography", *Eur. Phys. J.* **C67** (2010) 637–686,

`doi:10.1140/epjc/s10052-010-1314-6`, `arXiv:0906.1833`.

[63] R. K. Ellis, W. J. Stirling, and B. R. Webber, “Jet properties beyond fixed order”, pp. 193–236. Cambridge Monographs on Particle Physics, Nuclear Physics and Cosmology. Cambridge University Press, 1996. `doi:10.1017/CBO9780511628788.007`.

[64] J. Tseng and H. Evans, “Sequential recombination algorithm for jet clustering and background subtraction”, *Phys. Rev.* **D88** (2013) 014044, `doi:10.1103/PhysRevD.88.014044`, `arXiv:1304.1025`.

[65] CMS Collaboration, “Jet algorithms performance in 13 TeV data”, Technical Report CMS-PAS-JME-16-003, CERN, Geneva, (2017).

[66] CMS Collaboration, “Determination of Jet Energy Calibration and Transverse Momentum Resolution in CMS”, *JINST* **6** (2011) P11002, `doi:10.1088/1748-0221/6/11/P11002`, `arXiv:1107.4277`.

[67] “Jet energy scale and resolution performances with 13TeV data”,.

[68] CMS Collaboration, “Identification of b quark jets at the CMS Experiment in the LHC Run 2”,.

[69] CMS Collaboration, “Performance of b-Tagging Algorithms in Proton Collisions at 13 TeV using the 2016 Data”,.

[70] CMS Collaboration, “Performance of missing energy reconstruction in 13 TeV pp collision data using the CMS detector”, Technical Report CMS-PAS-JME-16-004, CERN, Geneva, (2016).

[71] CMS Collaboration, K. Stifter, “The CMS Beam Halo Monitor Detector System”, in *Proceedings, Meeting of the APS Division of Particles and Fields (DPF 2015): Ann Arbor, Michigan, USA, 4-8 Aug 2015.* 2015. `arXiv:1511.00264`.

[72] L. Randall and D. Tucker-Smith, “Dijet Searches for Supersymmetry at the LHC”, *Phys. Rev. Lett.* **101** (2008), no. 221803,.

[73] M. Baber, “Search for supersymmetry in the first $\sqrt{s} = 13$ TeV pp-collisions using the α_T variable with the CMS detector”. PhD thesis, Imperial College London, 2017.

[74] CMS Collaboration, “Simplified likelihood for the re-interpretation of public CMS results”, Technical Report CMS-NOTE-2017-001. CERN-CMS-NOTE-2017-001, CERN, Geneva, (Jan, 2017).

[75] CMS Collaboration, “CMS Luminosity Measurements for the 2016 Data Taking Period”, Technical Report CMS-PAS-LUM-17-001, CERN, Geneva, (2017).

[76] CMS Collaboration, “Public CMS Luminosity Information”, 2016.

[77] J. Alwall, R. Frederix, S. Frixione et al., “The automated computation of tree-level and next-to-leading order differential cross sections, and their matching to parton shower simulations”, *JHEP* **07** (2014) 079, `doi:10.1007/JHEP07(2014)079`, `arXiv:1405.0301`.

[78] S. Alioli, P. Nason, C. Oleari et al., “A general framework for implementing NLO calculations in shower Monte Carlo programs: the POWHEG BOX”, *JHEP* **06** (2010) 043, `doi:10.1007/JHEP06(2010)043`, `arXiv:1002.2581`.

[79] E. Re, “Single-top Wt-channel production matched with parton showers using the POWHEG method”, *Eur. Phys. J.* **C71** (2011) 1547, `doi:10.1140/epjc/s10052-011-1547-z`, `arXiv:1009.2450`.

[80] T. SjÃűstrand, S. Ask, J. R. Christiansen et al., “An Introduction to PYTHIA 8.2”, *Comput. Phys. Commun.* **191** (2015) 159–177, `doi:10.1016/j.cpc.2015.01.024`, `arXiv:1410.3012`.

[81] NNPDF Collaboration, “Parton distributions for the LHC Run II”, *JHEP* **04** (2015) 040, `doi:10.1007/JHEP04(2015)040`, `arXiv:1410.8849`.

[82] GEANT4 Collaboration, “GEANT4: A Simulation toolkit”, *Nucl. Instrum. Meth.* **A506** (2003) 250–303, `doi:10.1016/S0168-9002(03)01368-8`.

[83] CMS Collaboration, “Search for dark matter in proton-proton collisions at 8 TeV with missing transverse momentum and vector boson tagged jets”, *JHEP* **12** (2016) 083, `doi:10.1007/JHEP12(2016)083,10.1007/JHEP08(2017)035`, `arXiv:1607.05764`. [Erratum: JHEP08,035(2017)].

[84] CMS Collaboration, "Search for top-squark pair production in the single-lepton final state in pp collisions at $\sqrt{s}$ = 8 TeV", *Eur. Phys. J.* **C73** (2013), no. 12, 2677, `doi:10.1140/epjc/s10052-013-2677-2`, `arXiv:1308.1586`.

[85] CMS Collaboration, "Muon Identification and Isolation efficiency on full 2016 dataset",.

[86] CMS Collaboration, "Measurement of the differential cross sections for the associated production of a W boson and jets in proton-proton collisions at $\sqrt{s} = 13$ TeV", *Phys. Rev.* **D96** (2017), no. 7, 072005, `doi:10.1103/PhysRevD.96.072005`, `arXiv:1707.05979`.

[87] CMS Collaboration, "Measurement of the $t\bar{t}$ production cross section using events with one lepton and at least one jet in pp collisions at $\sqrt{s}$ = 13 TeV", *JHEP* **09** (2017) 051, `doi:10.1007/JHEP09(2017)051`, `arXiv:1701.06228`.

[88] Z. Bern et al., "Left-Handed W Bosons at the LHC", *Phys. Rev.* **D84** (2011) 034008, `doi:10.1103/PhysRevD.84.034008`, `arXiv:1103.5445`.

[89] K. Johansson, "Discrete orthogonal polynomial ensembles and the Plancherel measure", *ArXiv Mathematics e-prints* (June, 1999) `arXiv:math/9906120`.

[90] H. B. Prosper and L. Lyons, eds., "Proceedings, PHYSTAT 2011 Workshop on Statistical Issues Related to Discovery Claims in Search Experiments and Unfolding, CERN,Geneva, Switzerland 17-20 January 2011", CERN. CERN, Geneva, (2011).

[91] G. Cowan, K. Cranmer, E. Gross et al., "Asymptotic formulae for likelihood-based tests of new physics", *Eur. Phys. J.* **C71** (2011) 1554, `doi:10.1140/epjc/s10052-011-1554-0,10.1140/epjc/s10052-013-2501-z`, `arXiv:1007.1727`. [Erratum: Eur. Phys. J.C73,2501(2013)].

[92] A. L. Read, "Presentation of search results: The CL(s) technique", *J. Phys.* **G28** (2002) 2693–2704, `doi:10.1088/0954-3899/28/10/313`. [,11(2002)].

[93] C. Borschensky, M. KrÃd'mer, A. Kulesza et al., "Squark and gluino production cross sections in pp collisions at $\sqrt{s}$ = 13, 14, 33 and 100 TeV", *Eur. Phys. J.* **C74** (2014), no. 12, 3174,

`doi:10.1140/epjc/s10052-014-3174-y`, `arXiv:1407.5066`.

[94] CMS Collaboration, "Search for supersymmetry in multijet events with missing transverse momentum in proton-proton collisions at 13 TeV", *Phys. Rev.* **D96** (2017), no. 3, 032003, `doi:10.1103/PhysRevD.96.032003`, `arXiv:1704.07781`.

[95] CMS Collaboration, "Search for new physics in the all-hadronic final state with the MT2 variable",.

[96] ATLAS Collaboration, "Search for new phenomena with large jet multiplicities and missing transverse momentum using large-radius jets and flavour-tagging at ATLAS in 13 TeV pp collisions", `arXiv:1708.02794`.

[97] ATLAS Collaboration, "Search for supersymmetry in events with b-tagged jets and missing transverse momentum in pp collisions at $\sqrt{s} = 13$ TeV with the ATLAS detector", `arXiv:1708.09266`.

[98] CMS Collaboration, "Search for supersymmetry in final states with missing transverse energy and 0, 1, 2, or at least 3 b-quark jets in 7 TeV pp collisions using the variable alphaT", *JHEP* **01** (2013) 077, `doi:10.1007/JHEP01(2013)077`, `arXiv:1210.8115`.

[99] CMS Collaboration, "Search for supersymmetry in hadronic final states with missing transverse energy using the variables α_T and b-quark multiplicity in pp collisions at $\sqrt{s} = 8$ TeV", *Eur. Phys. J.* **C73** (2013), no. 9, 2568, `doi:10.1140/epjc/s10052-013-2568-6`, `arXiv:1303.2985`.

[100] CMS Collaboration, "Search for top squark pair production in compressed-mass-spectrum scenarios in proton-proton collisions at $\sqrt{s}$ = 8 TeV using the α_T variable", *Phys. Lett.* **B767** (2017) 403–430, `doi:10.1016/j.physletb.2017.02.007`, `arXiv:1605.08993`.

[101] CMS Collaboration, "A search for new phenomena in pp collisions at $\sqrt{s} = 13\,\mathrm{TeV}$ in final states with missing transverse momentum and at least one jet using the α_T variable", *Eur. Phys. J.* **C77** (2017), no. 5, 294, `doi:10.1140/epjc/s10052-017-4787-8`, `arXiv:1611.00338`.

[102] E. Bagnaschi, G. F. Giudice, P. Slavich et al., "Higgs Mass and Unnatural

Supersymmetry”, *JHEP* **09** (2014) 092, `doi:10.1007/JHEP09(2014)092`, `arXiv:1407.4081`.

[103] J. D. Wells, “Implications of supersymmetry breaking with a little hierarchy between gauginos and scalars”, in *11th International Conference on Supersymmetry and the Unification of Fundamental Interactions (SUSY 2003) Tucson, Arizona, June 5-10, 2003*. 2003. `arXiv:hep-ph/0306127`.

[104] N. Arkani-Hamed and S. Dimopoulos, “Supersymmetric unification without low energy supersymmetry and signatures for fine-tuning at the LHC”, *JHEP* **06** (2005) 073, `doi:10.1088/1126-6708/2005/06/073`, `arXiv:hep-th/0405159`.

[105] G. F. Giudice and A. Romanino, “Split supersymmetry”, *Nucl. Phys.* **B699** (2004) 65–89, `doi:10.1016/j.nuclphysb.2004.11.048,10.1016/j.nuclphysb.2004.08.001`, `arXiv:hep-ph/0406088`. [Erratum: Nucl. Phys.B706,487(2005)].

[106] CMS Collaboration, “Search for top squark and higgsino production using diphoton Higgs boson decays”, *Phys. Rev. Lett.* **112** (2014) 161802, `doi:10.1103/PhysRevLett.112.161802`, `arXiv:1312.3310`.

[107] CMS Collaboration, “Searches for electroweak neutralino and chargino production in channels with Higgs, Z, and W bosons in pp collisions at 8 TeV”, *Phys. Rev.* **D90** (2014), no. 9, 092007, `doi:10.1103/PhysRevD.90.092007`, `arXiv:1409.3168`.

[108] ATLAS Collaboration, “Search for supersymmetry in events with photons, bottom quarks, and missing transverse momentum in protonâĂŞproton collisions at a centre-of-mass energy of 7 TeV with the ATLAS detector”, *Phys. Lett.* **B719** (2013) 261–279, `doi:10.1016/j.physletb.2013.01.041`, `arXiv:1211.1167`.

Appendix A.

Event characterization

A.1. Data and simulation distribution

Figure A.1-A.7 show the data and MC distribution in four kinematic variables used for event categorization in the signal, $\mu +$ jets and $\mu\mu +$ jets control region.

A.2. Background process breakdown

Figure A.10-A.12 show dominant SM background portions in the Signal, $\mu +$ jets and $\mu\mu +$ jets control region.

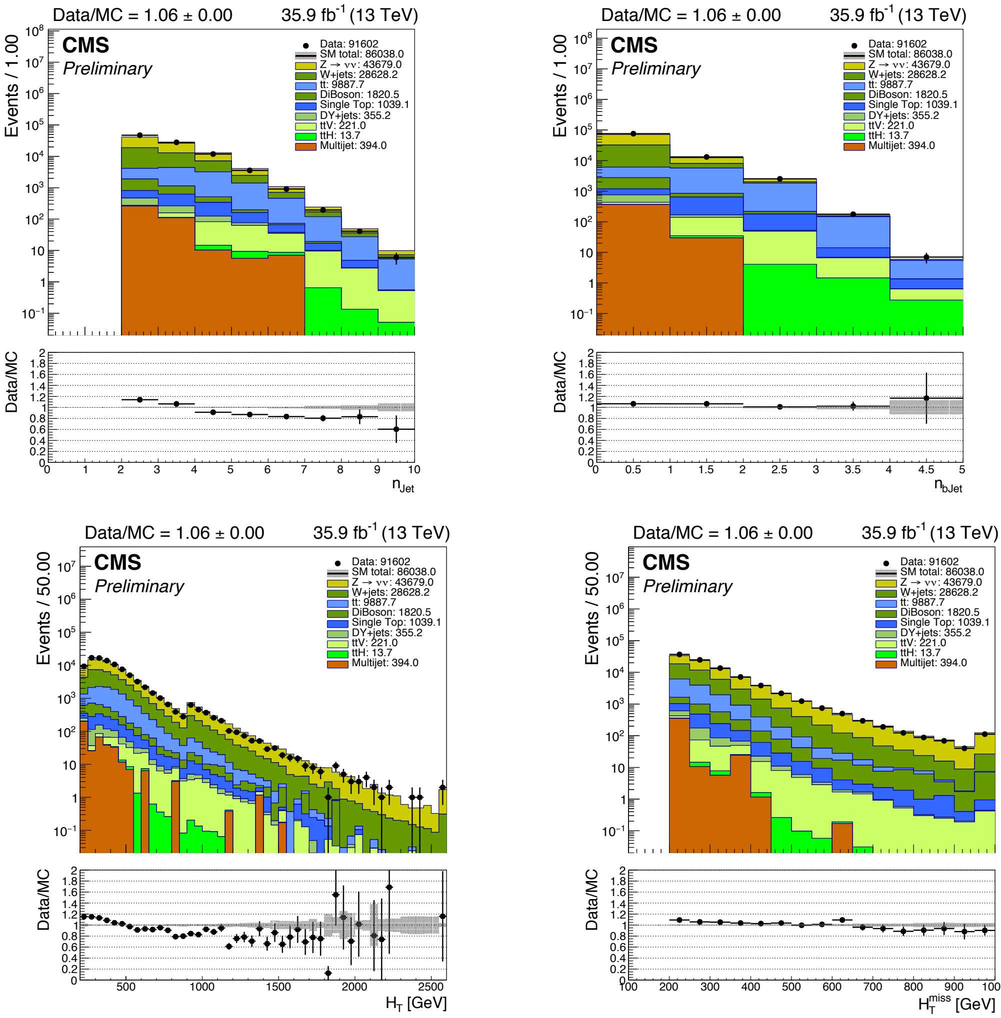

Figure A.1.: Data and MC distribution in four kinematic variables for event categorization in the signal region in the symmetric category.

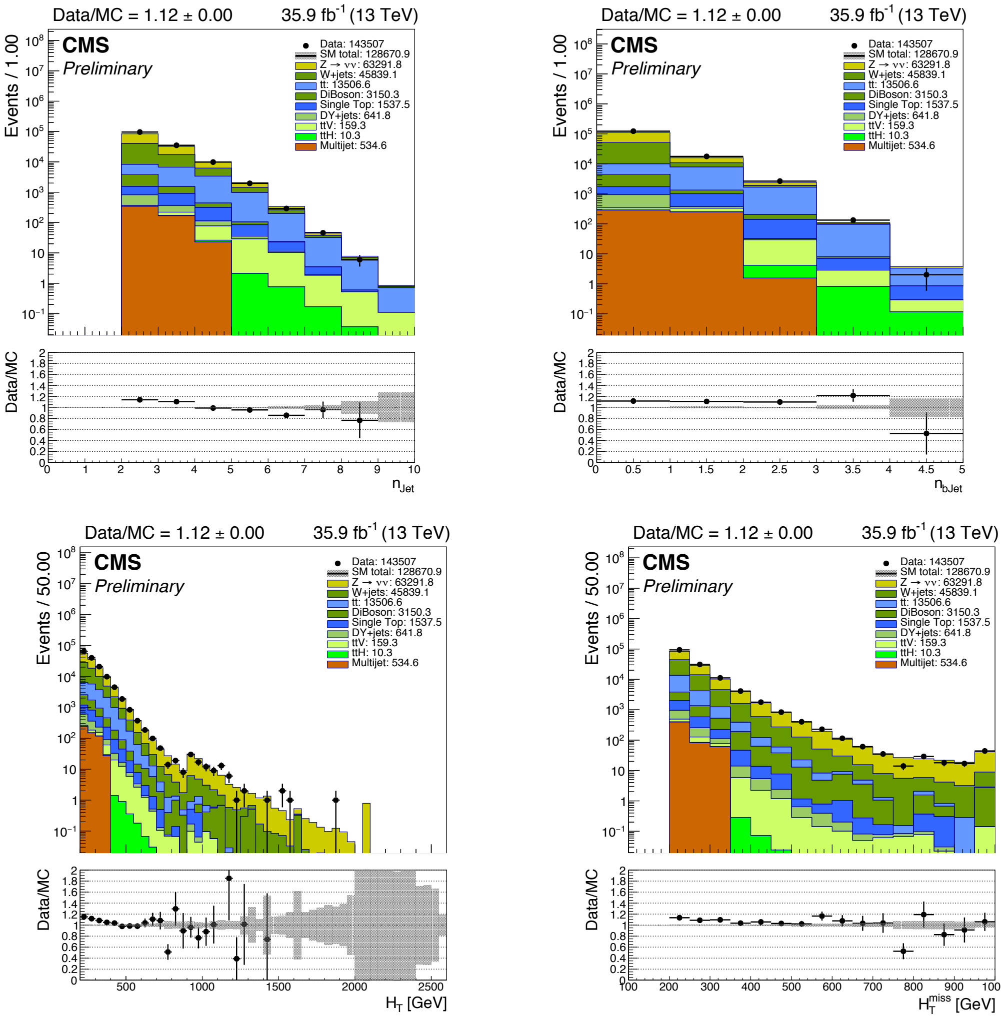

Figure A.2.: Data and MC distribution in four kinematic variables for event categorization in the signal region in the asymmetric category.

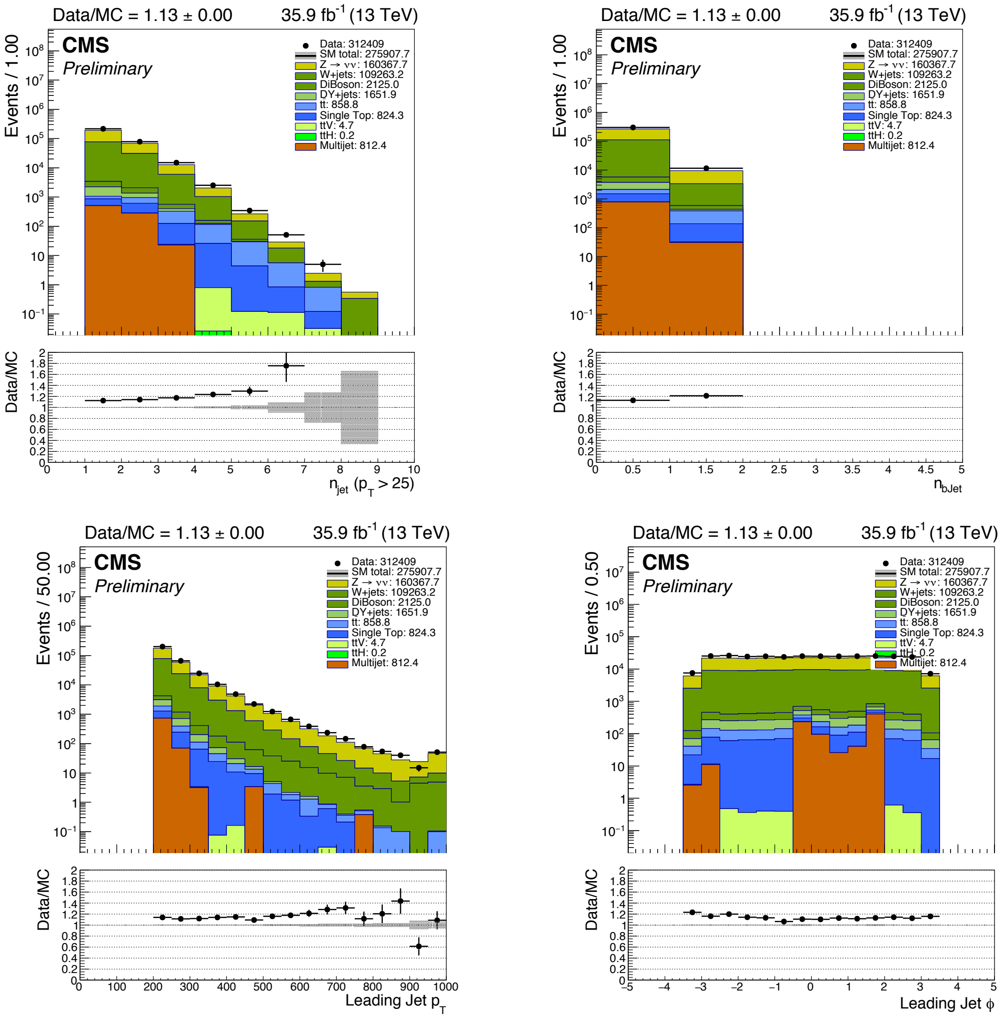

Figure A.3.: Data and MC distribution in four kinematic variables for event categorization in the signal region in the monojet category.

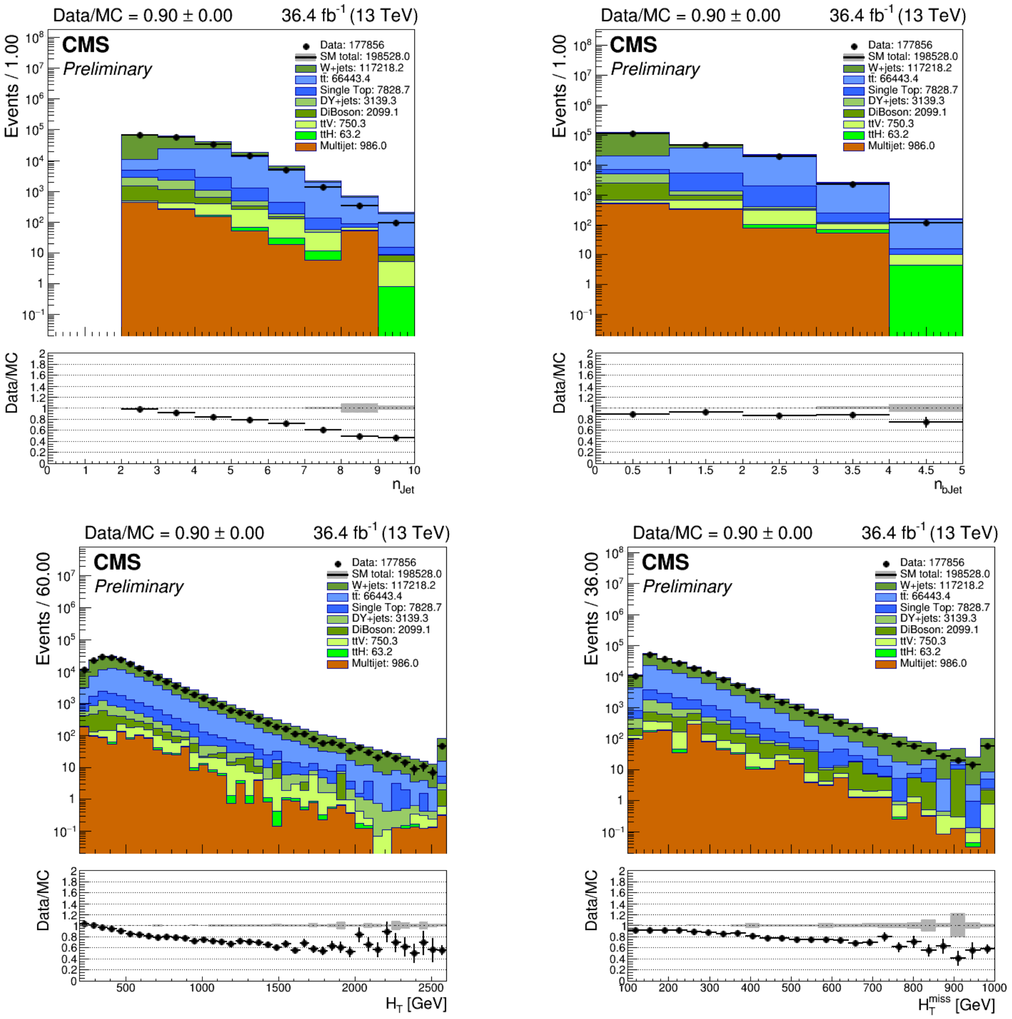

Figure A.4.: Data and MC distribution in four kinematic variables for event categorization in the $\mu +$ jets control region in the symmetric category.

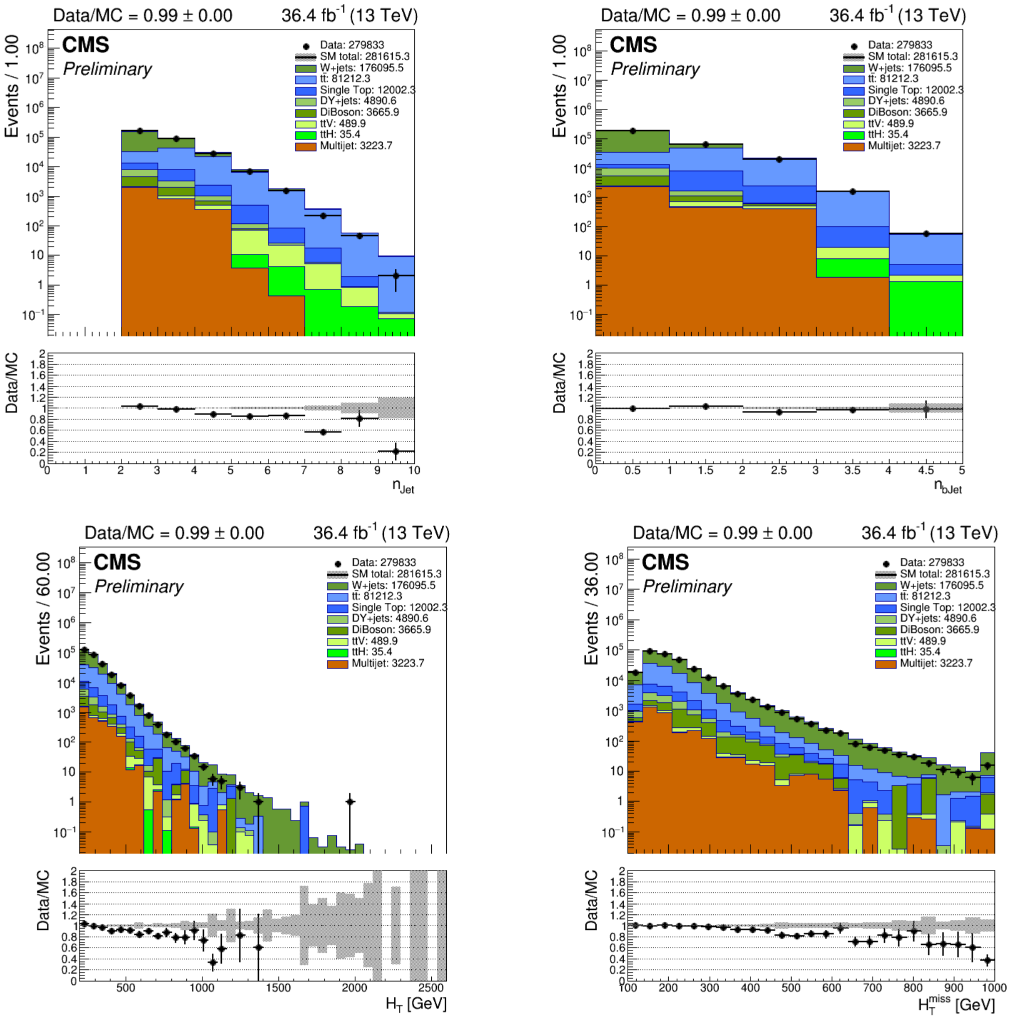

Figure A.5.: Data and MC distribution in four kinematic variables for event categorization in the $\mu +$ jets control region in the asymmetric category.

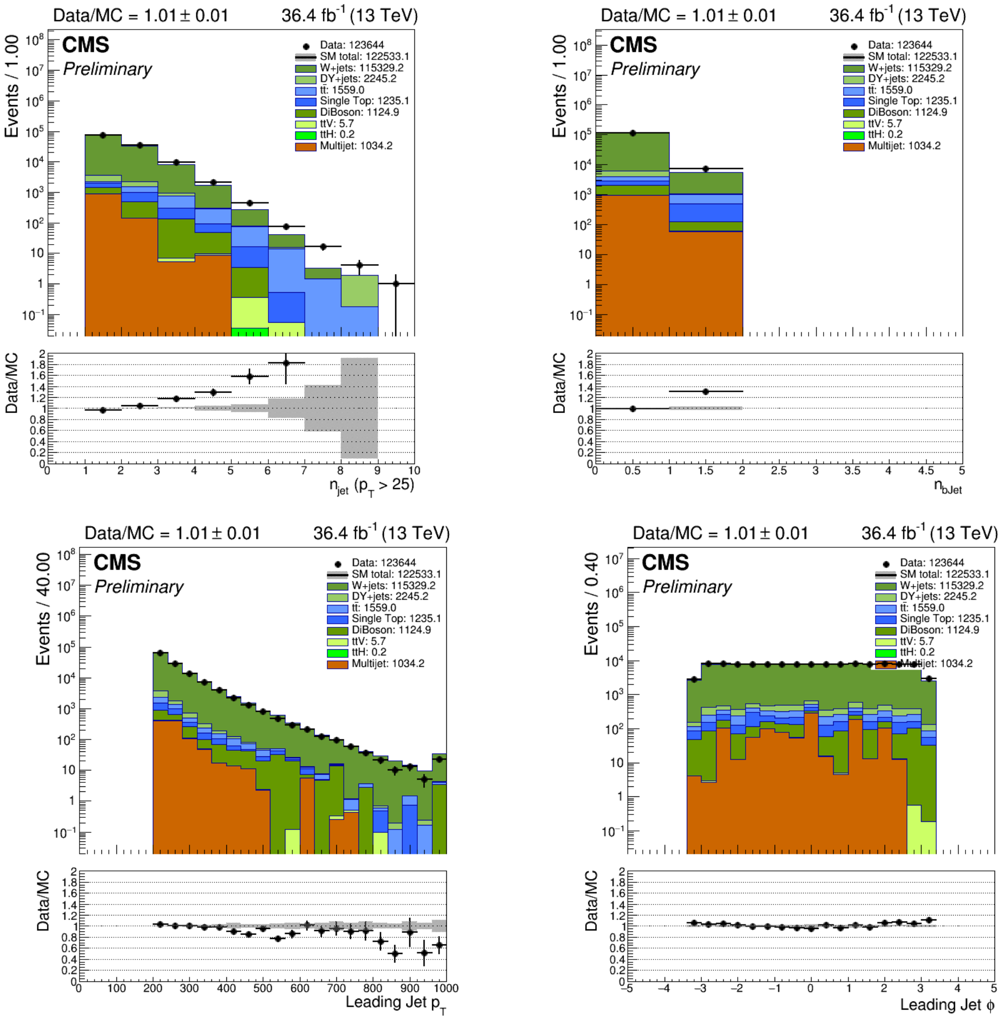

Figure A.6.: Data and MC distribution in four kinematic variables for event categorization in the $\mu +$ jets control region in the monojet category.

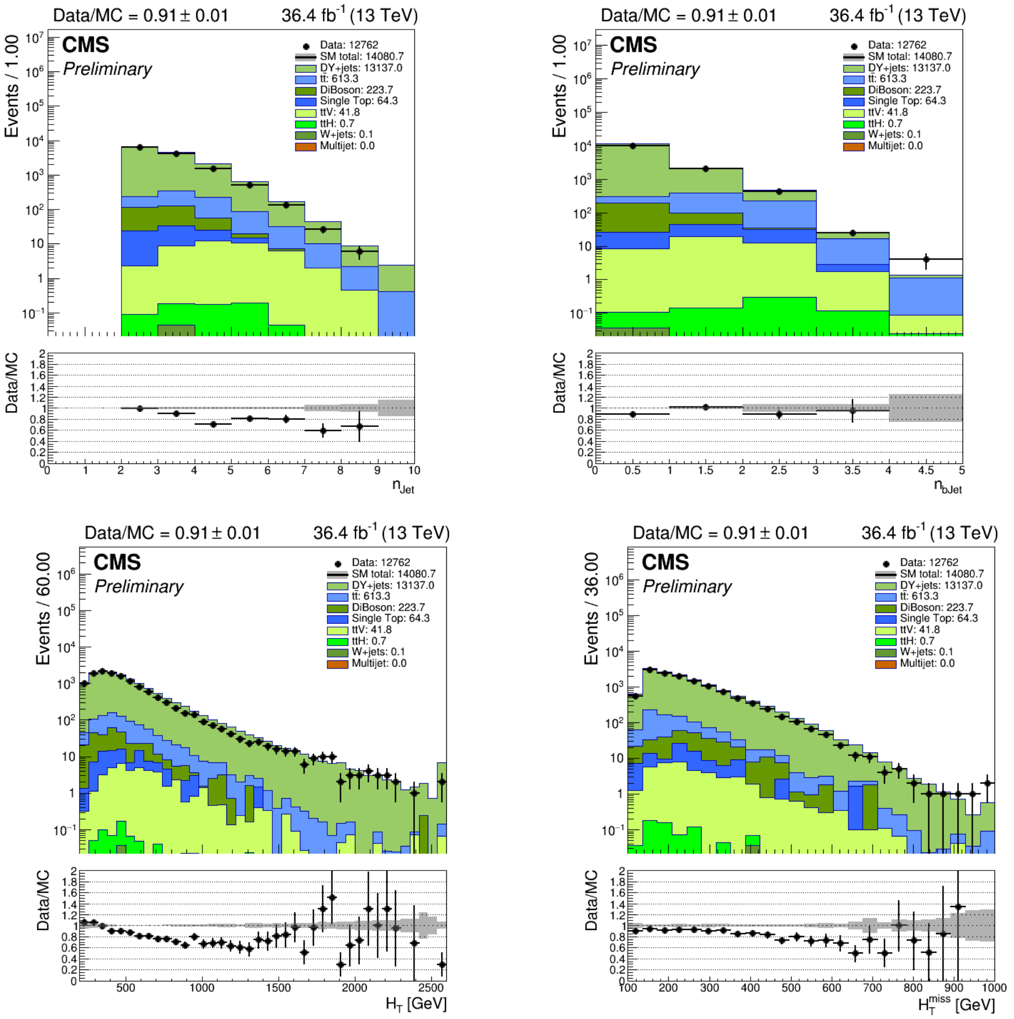

Figure A.7.: Data and MC distribution in four kinematic variables for event categorization in the $\mu\mu$ + jets control region in the symmetric category.

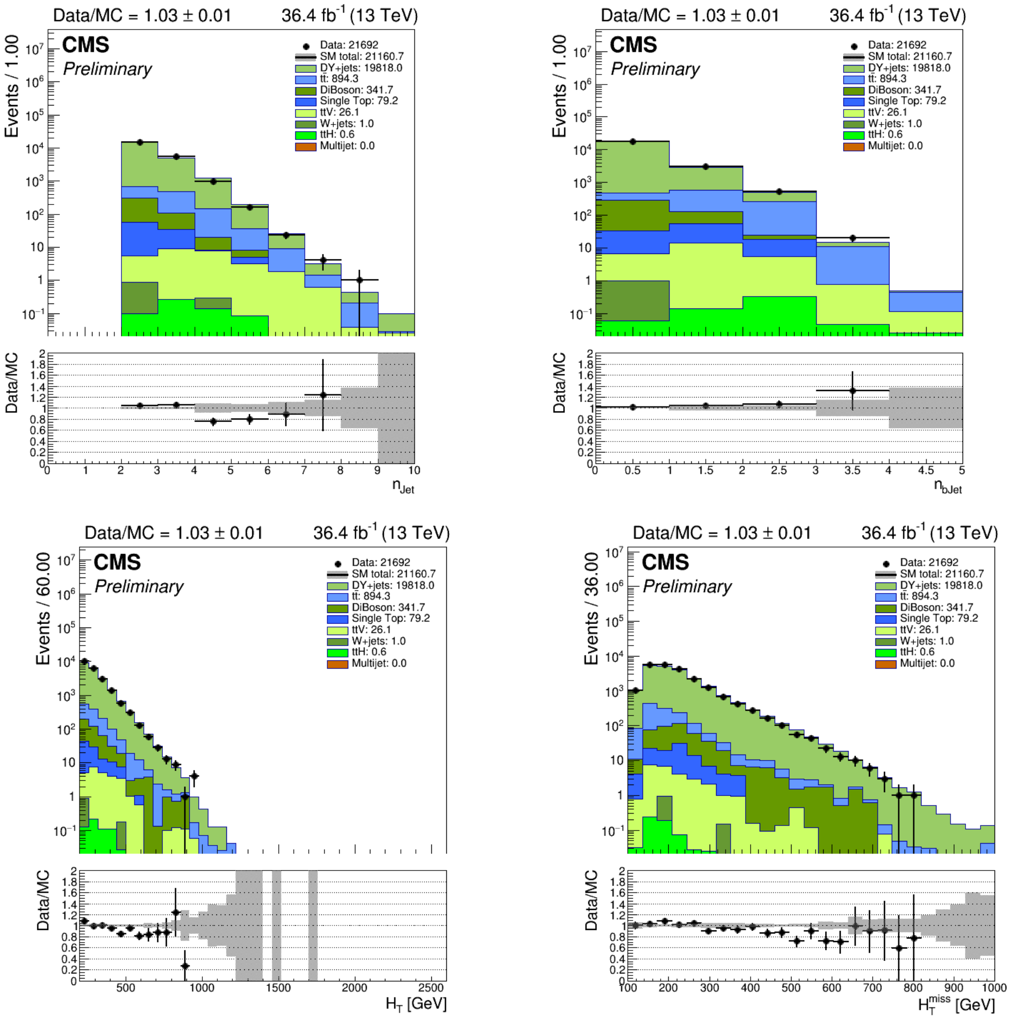

Figure A.8.: Data and MC distribution in four kinematic variables for event categorization in the $\mu\mu +$ jets control region in the asymmetric category.

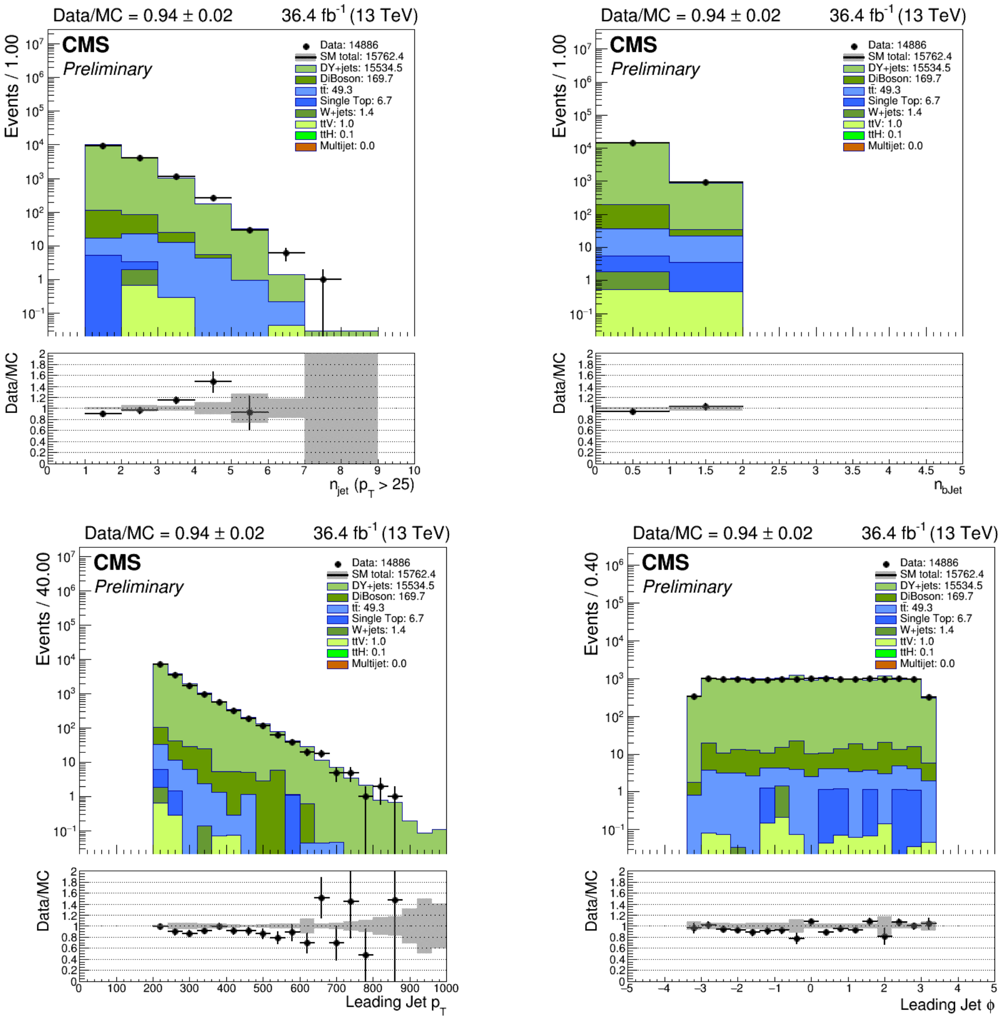

Figure A.9.: Data and MC distribution in four kinematic variables for event categorization in the $\mu\mu$ + jets control region in the monojet category.

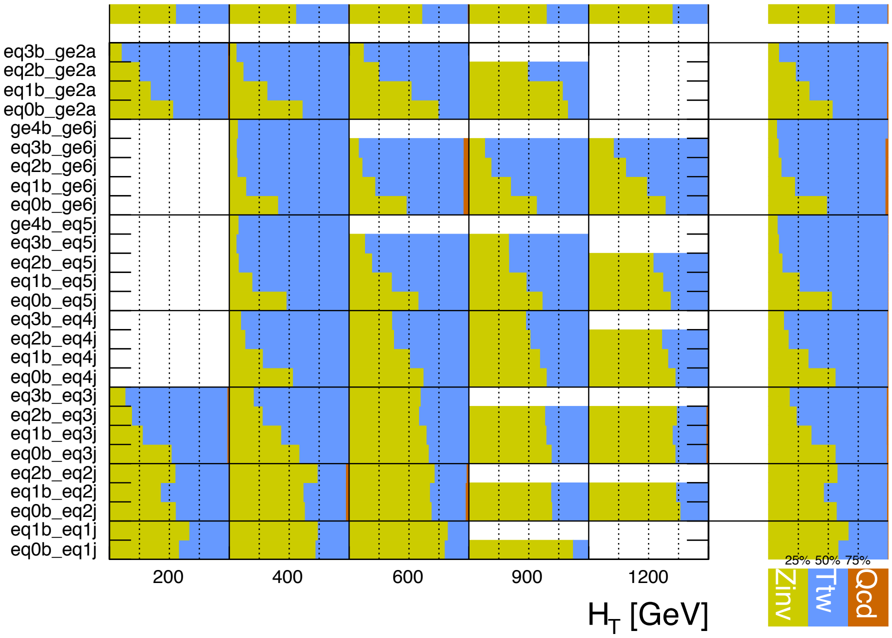

Figure A.10.: SM process breakdown in the $\mu +$ jets control region in (N_{jet}, N_b) versus H_T category.

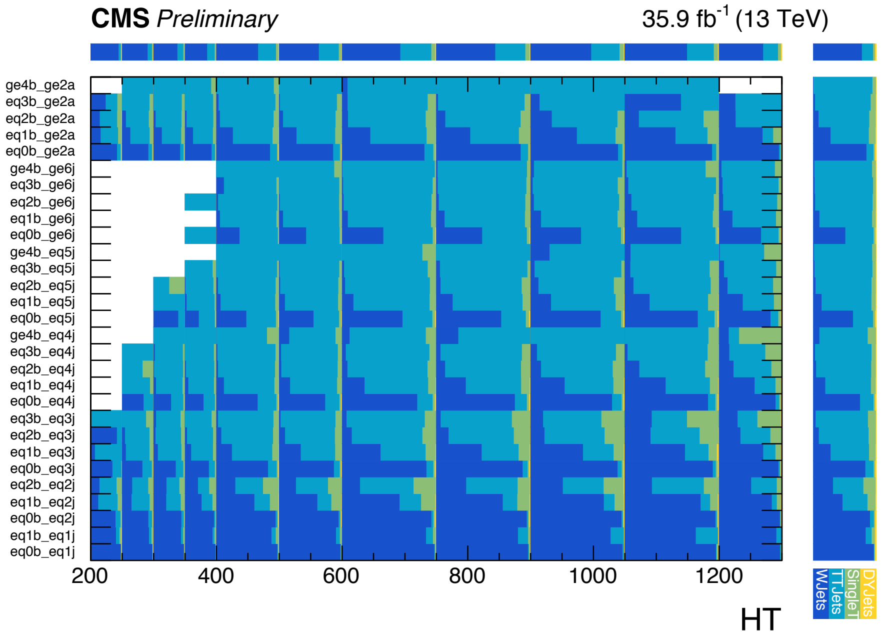

Figure A.11.: SM process breakdown in the $\mu +$ jets control region in (N_{jet}, N_b) versus H_T category.

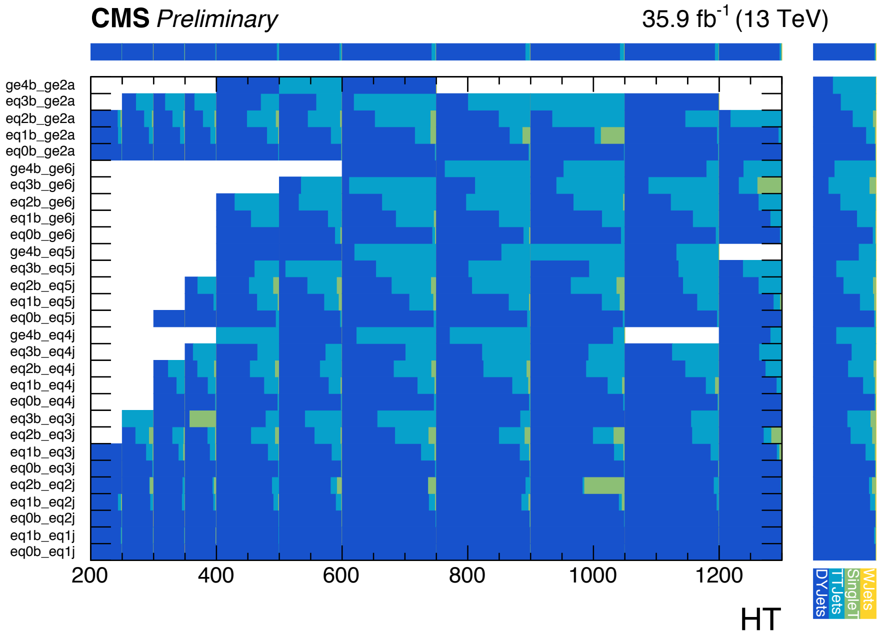

Figure A.12.: SM process breakdown in the $\mu\mu$ + jets control region in (N_{jet}, N_b) versus H_T category.

Appendix B.

Cross section for simulated backgrounds

Data set	Cross section [pb]
ZJetsToNuNu HT100To200	$3.448 \times 10^{+02}$
ZJetsToNuNu HT200To400	$9.553 \times 10^{+01}$
ZJetsToNuNu HT400To600	$1.320 \times 10^{+01}$
ZJetsToNuNu HT600To800	$3.221 \times 10^{+00}$
ZJetsToNuNu HT800To1200	$1.474 \times 10^{+00}$
ZJetsToNuNu HT1200To2500	3.586×10^{01}
ZJetsToNuNu HT2500ToInf	8.203×10^{03}
WJetsToLNu HT100To200	$1.627 \times 10^{+03}$
WJetsToLNu HT200To400	$4.352 \times 10^{+02}$
WJetsToLNu HT400To600	$5.918 \times 10^{+01}$
WJetsToLNu HT600To800	$1.458 \times 10^{+01}$
WJetsToLNu HT800To1200	$6.656 \times 10^{+00}$
WJetsToLNu HT1200To2500	$1.608 \times 10^{+00}$
WJetsToLNu HT2500ToInf	3.891×10^{02}
TTJets DiLept	$8.829 \times 10^{+01}$
TTJets SingleLeptFromTbar	$1.827 \times 10^{+02}$
DYJetsToLL HT100to200	$1.813 \times 10^{+02}$
DYJetsToLL HT200to400	$5.042 \times 10^{+01}$
DYJetsToLL HT400to600	$6.984 \times 10^{+00}$
DYJetsToLL HT600to800 v2	$1.681 \times 10^{+00}$
DYJetsToLL HT800to1200	7.754×10^{01}
DYJetsToLL HT1200to2500	1.862×10^{01}
DYJetsToLL HT2500toInf	4.385×10^{03}
GJets HT40To100	$2.079 \times 10^{+04}$
GJets HT100To200	$9.238 \times 10^{+03}$
GJets HT200To400	$2.305 \times 10^{+03}$
GJets HT400To600	$2.744 \times 10^{+02}$
GJets HT600ToInf	$9.346 \times 10^{+01}$

Table B.1.: Summary of cross section used to reweigh simulated background samples.

Data set	Cross section [pb]
`QCD HT100to200`	$2.799 \times 10^{+07}$
`QCD HT200to300`	$1.712 \times 10^{+06}$
`QCD HT300to500`	$3.477 \times 10^{+05}$
`QCD HT500to700`	$3.210 \times 10^{+04}$
`QCD HT700to1000`	$6.831 \times 10^{+03}$
`QCD HT1000to1500`	$1.207 \times 10^{+03}$
`QCD HT1500to2000`	$1.199 \times 10^{+02}$
`QCD HT2000toInf`	$2.524 \times 10^{+01}$
`ST s-channel-4f-leptonDecays`	$3.344 \times 10^{+00}$
`ST t-channel-antitop-4f-inclusiveDecays`	$8.095 \times 10^{+01}$
`ST t-channel-top-4f-inclusiveDecays`	$1.360 \times 10^{+02}$
`TTWJetsToQQ`	4.062×10^{-01}
`TTZToQQ`	5.297×10^{-01}
`TTGJets`	$3.697 \times 10^{+00}$
`ttHToNonbb`	2.151×10^{-01}
`ttHTobb`	2.934×10^{-01}
`WW`	$1.139 \times 10^{+02}$
`WZ`	$4.713 \times 10^{+01}$
`ZZ`	$1.652 \times 10^{+01}$
`EWKWMinus2Jets WToLNu`	$2.036 \times 10^{+01}$
`EWKWPlus2Jets WToLNu`	$2.582 \times 10^{+01}$
`EWKZ2Jets ZToLL`	$3.998 \times 10^{+00}$
`EWKZ2Jets ZToNuNu`	$1.014 \times 10^{+01}$

Table B.2.: Summary of cross section used to reweigh simulated rare background samples.

Appendix C.

List of abbreviations

ALICE	A Large Ion Collider Experiment
ATLAS	A Toroidal LHC ApparatuS
BSM	Beyond Standard Model
CDF	Collision Detector Fermilab
CERN	Organisation European pour la Recherche Nucleaire
CL	Confidence Level
CMS	Compact Muon Solenoid
CR	Control Region
CSC	Cathode Strip Chamber
DAQ	Data AcQuisition
ECAL	Electromagnetic CALorimeter
FSR	Final State Radiation

HCAL	Hadron CALorimeter
HERA	Hadron Elektron Ring Anlage
HI	Heavy Ion
HLT	High Level Trigger
IP	Interaction Point
L1	Level-1
LHC	Large Hadron Collider
LO	Leading Order
MC	Monte Carlo
ML	Maximum Likelihood
NLO	Next Leading Order
NNLO	Next Next Leading Order
PDF	Parton Density Function
POI	Parameter of Interest
pp	proton-proton
PU	Pile-Up
QCD	Quantum Chromodynamics
QED	Quantum Electrodynamics
QGP	Quark Gluon Plasma
RPC	Resistive Plate Chamber
SB	Side Band
SM	Standard Model
SR	Signal Region
SV	Secondary Vertex